DISSERTATION

INFLUENCE OF ANATOMIC VALVE CONDITIONS AND CORONARY FLOW ON AORTIC SINUS HEMODYNAMICS

Submitted by

Brandon L Moore

Department of Mechanical Engineering

In partial fulfillment of the requirements

For the Degree of Doctor of Philosophy

Colorado State University

Fort Collins, Colorado

Fall 2015

Doctoral Committee:

Advisor: Lakshmi Prasad Dasi
Co-Advisor: Xinfeng Gao

Allan Kirkpatrick
Christopher Orton

ABSTRACT

INFLUENCE OF ANATOMIC VALVE CONDITIONS AND CORONARY FLOW ON AORTIC SINUS HEMODYNAMICS

Heart disease is the leading cause of death in the US, and aortic valve stenosis represents a significant portion of this disease. While the specific causes of stenosis are not entirely clear, its development has been strongly linked to mechanical factors such as localized solid and fluid stresses and strains, especially on the aortic side of the valve leaflets. These mechanical cues can be tied to valvular hemodynamics, however the factors regulating these hemodynamics are relatively unknown. Therefore, the overarching hypothesis of this research is that aortic valve sinus hemodynamics are regulated by anatomic valve conditions and presence of coronary flow. This hypothesis is explored through three specific aims: 1) to develop methodologies for quantifying hemodynamics within the aortic sinuses, 2) to characterize the differences in native valve flow patterns that occur due to patient and sinus variability, and 3) to evaluate the hemodynamic impacts of different prosthetic aortic valve implantations.

In this work, experimental methods have been developed to study a broad range of aortic valve conditions, and computational models were also employed to validate and enhance experimental findings. An in vitro setup is presented using a surgical bioprosthesis as a native aortic valve model, while additional valve implantations were also tested. Physiological pressures and flow rates were imposed across these valves via an in-house pumping loop, which included a novel coronary flow branch. Two-dimensional time-resolved particle image velocimetry (PIV) protocols were developed and employed to analyze sinus vorticity dynamics. Computationally, both 2D and 3D simulations were run in ANSYS Fluent to enhance experimental findings.

Results from this research demonstrate that aortic sinus hemodynamics are indeed regulated by anatomic valve conditions and coronary flow. From a clinical perspective, average valve geometric parameters tend to produce hemodynamics that are least likely to initiate disease than those near the upper or lower anatomical limits. Coronary flow was likewise found to increase sinus velocities and shear stresses near the leaflets, which is also beneficial for valve health. The prosthetic valves tested – transcatheter and sutureless – both severely limited sinus perfusion, which could help explain an increased risk of thrombus formation in the transcatheter case and suggests similar risk for sutureless valves. These findings could help educate clinicians on proper courses of treatment based on patient-specific valve parameters, and could also provide useful information for engineers when designing new valve prostheses.

ACKNOWLEDGEMENTS

There are a number of people I would like to thank for their support and contributions to this research. First and foremost, thank you, Dr. Prasad Dasi, for being an outstanding advisor and mentor. I greatly appreciate the knowledge and expertise you have shared with me over the past five years. Thank you to my co-advisor, Dr. Xinfeng Gao, for guiding my computational work. Thank you also to my committee members, Dr. Chris Orton and Dr. Allan Kirkpatrick.

Thank you Dr. Pablo Maureira for sharing your clinical expertise and for providing our lab with prosthetic heart valves. It was a pleasure working with you during your time in Fort Collins.

I am grateful to the Mechanical Engineering Department for supporting me through a Graduate Teaching Assistantship. This position provided both financial support as well as invaluable experience.

My fellow graduate students in the Cardiovascular and Biofluid Mechanics Laboratory have all contributed to this work in some way. I appreciate the support and camaraderie from everyone. Thank you all - it has been a pleasure working in this lab group.

Last, but not least, I would like to acknowledge my parents for their continuing support regardless of my endeavors. Thank you Mom and Dad!

TABLE OF CONTENTS

LIST OF TABLES

LIST OF FIGURES

1. INTRODUCTION

Heart disease is the leading cause of death in the United States, and valvular diseases comprise a large subset of this condition. Aortic valve stenosis, in particular, is present in over five percent of the population [1]. Representing one specific cause of aortic stenosis, calcific aortic valve disease (CAVD) affects a wide range of the US population, leading to approximately 50,000 valve replacements each year [2]. In addition to stenosis, thrombosis on or near the valve is also a major cardiovascular issue. Since these diseases are strongly tied to mechanics, namely within the aortic sinuses, understanding valvular hemodynamics is crucial for further understanding of disease progression and development of patient care strategies.

Many different anatomical and physiological aortic valve conditions exist. For example, patient-specific anatomy and physiology yield a range of geometric and flow conditions across the human population. The valve is also radially asymmetric due to slight geometric variations as well as presence of coronary ostia in only two of the three sinuses. Prosthetic aortic valves, used to replace failing native valves, can also drastically alter the geometric and flow characteristics of the aortic root.

Understanding these different valve conditions and their implications for hemodynamics could provide useful information for physicians and surgeons regarding management therapies or surgical interventions. Such knowledge could also aid engineers in designing new valve prostheses. Given these potential impacts, along with basic physical considerations relating valve structure and function, **the overarching hypothesis of this research is that aortic valve sinus hemodynamics are regulated by anatomic valve conditions and presence of coronary flow.** The following are specific aims that test this hypothesis.

- *Specific Aim 1 – Develop methodologies for quantifying hemodynamics within the aortic sinuses*
    - Currently no method exists to quantify hemodynamics in the fine detail that is required for this research
    - In vivo methods (e.g. 4D MRI) are under resolved
    - Will form the basis for future studies

- *Specific Aim 2: Characterize the differences in native valve flow patterns that occur due to patient and sinus variability*
    - Will help explain the mechanistic causes of calcific aortic stenosis
    - No experimental techniques have yet been developed to analyze coronary sinus hemodynamics

- *Specific Aim 3: Evaluate the hemodynamic impacts of different prosthetic aortic valve implantations*
    - Many clinical studies for recently-developed valves lack detailed hemodynamic information
    - Will give novel insight into hemodynamics of state-of-the-art valve prostheses

To achieve the above aims, a two-dimensional, time-resolved particle image velocimetry protocol was developed to examine sinus hemodynamics in vitro under a variety of different anatomical and physiological valve conditions. Computational models were also created to help validate experiments and to provide further insight into hemodynamic parameters within the sinuses. It was found that the aortic sinus vortex is an unsteady turbulent structure with complex spatiotemporal characteristics, and these characteristics depend on anatomical factors such as sinus size and aspect ratio. Additionally, presence of coronary flow can significantly alter sinus flow patterns by energizing the sinus vortex and providing washout flow near the

base of the leaflet. Finally, the study of different types of bioprostheses showed that these valves tend to impede vortex formation and therefore limit blood flow into the sinuses.

This dissertation is organized as follows: A brief background on aortic valve anatomy, physiology, and mechanobiology followed by a literature review of current research is presented in Chapter 2. Specific Aim 1, which involves the development of experimental and computational methodologies, is outlined in Chapter 3 along with results of baseline studies. Chapter 4 covers Specific Aim 2, which details parametric studies of anatomic and hemodynamic valve conditions. Chapter 5 is devoted to Specific Aim 3, which involves experimental testing of prosthetic aortic valve implantations. Chapter 6 provides an overall summary and outlines possible future work, and Chapter 7 is a list of contributions to the field, including journal articles and conference publications. References are given in Chapter 8 and appendices are included in Chapter 9.

2. BACKGROUND

2.1 General Aortic Valve Background

2.1.1 Aortic Valve Anatomy

The heart pumps blood in order to supply the body tissues with oxygen and remove carbon dioxide [3]. There are 4 chambers and 4 valves in the heart (see Figure 2.1). The left and right ventricles are responsible for pumping blood via contraction of cardiac muscle known as myocardium. The period of time that the ventricles are expelling blood is known as systole, while the period of time that the ventricular myocardium is relaxed is known as diastole. The left and right atria receive blood after circulation to the lungs and body, respectively, and then pass this blood to the ventricles. The two atrioventricular valves – tricuspid and mitral – form one-way flow passages between each atrium and ventricle, and the two semilunar valves – pulmonary and aortic – ensure one-way flow from ventricles to blood vessels. The right side of

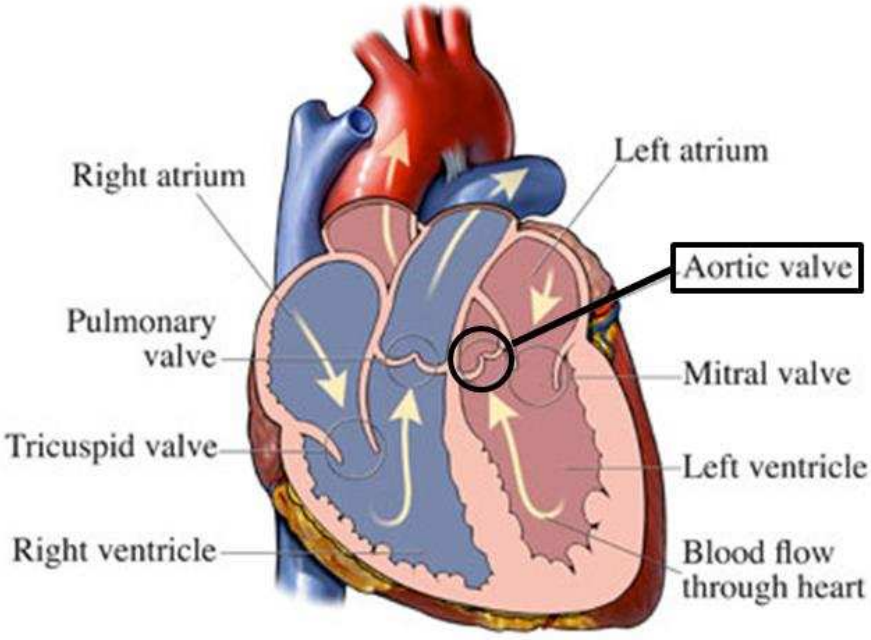

Figure 2.1: Schematic of the human heart
A cutaway diagram of the heart is shown, with the aortic valve highlighted and directions of blood flow indicated (figure adapted from [3])

the heart, which is colored purple in Figure 2.1, pumps blood to the lungs. The left side of the heart, colored in red, pumps blood to the rest of the body.

The aortic valve is comprised of three moving parts called leaflets as well as a surrounding structure known as the aortic root [6]. A diagram of a valve that has been sliced open and peeled apart is shown in Figure 2.2a.

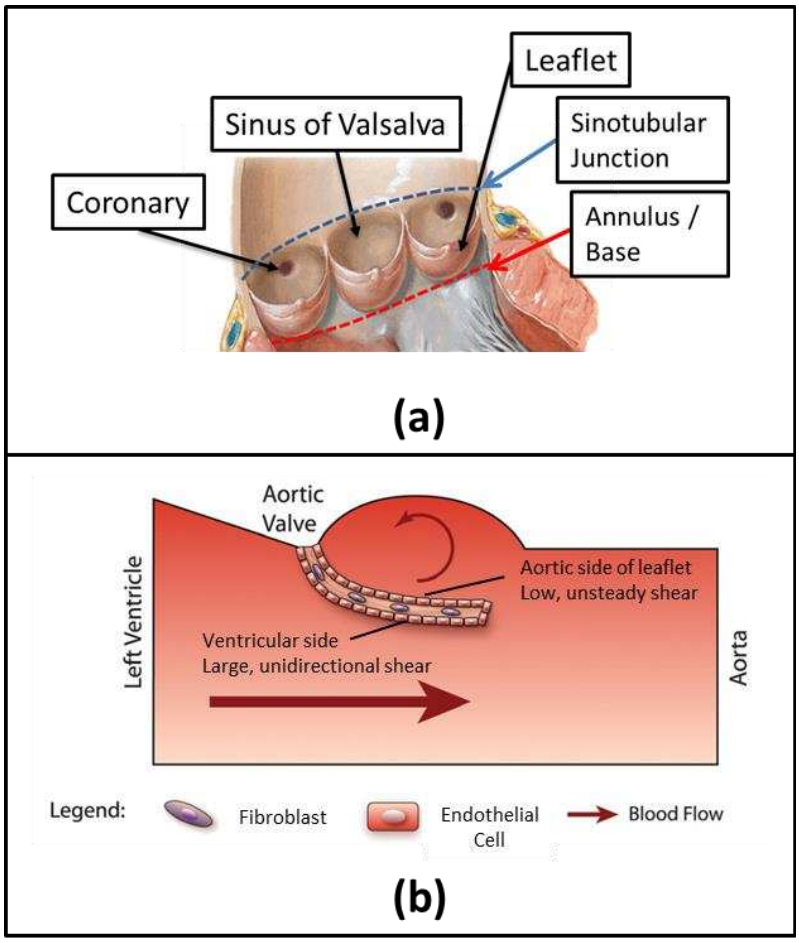

Figure 2.2: Detailed aortic valve anatomy
a) Depiction of an aortic valve that has been sliced and "unrolled" (figure adapted from [4]) . b) The two sides of the aortic valve leaflet are exposed to vastly different types and magnitudes of shear stress (figure adapted from [5])

The junction of the ventricle and aorta, where the leaflets attach, forms a ring-like structure known as the annulus, or base, of the valve. Downstream of the annulus are three "bulges" in

the walls of the aortic root corresponding to each leaflet, which are termed the Sinuses of Valsalva. Of the three total sinuses, two contain coronary arteries, which are the vessels that supply the heart muscle itself with blood. The dividing line between the sinuses and the main cylindrical portion of the aorta is called the sinotubular junction. At a slightly finer scale, each leaflet is divided into three layers: the ventricularis, spongiosa, and fibrosa. The fibrosa lies on the aortic side of the leaflet and therefore is exposed to the same flow environment as its corresponding sinus during systole. The spongiosa forms the middle layer of the leaflet and the ventricularis lies on the ventricular side of the valve. As shown in Figure 2.2b, valvular endothelial cells line the aortic and ventricular sides of the valve, while the spongiosa is comprised of valvular interstitial cells, such as fibroblasts and myofibroblasts, as well as glycosaminoglycans and water ([7, 8])). The fibrosa and ventricularis both contain collagen and elastin, but in different proportions. The fibrosa is composed mainly of circumferentially-oriented collagen fibers while the ventricularis contains mainly elastin fibers that are oriented in a somewhat axial direction. In general, collagen fibers carry most of the tensile loads while elastin fibers appear to provide a “return-spring” effect in order to help return collagen fibers to their rest geometry [7].

There is a wide range of anatomic variability across healthy human aortic valves. Thubrikar has summarized common variations in different geometric parameters from a multitude of studies, as shown in Figure 2.3 [9].

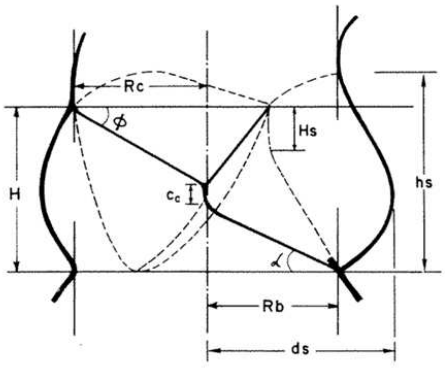

(a)

TABLE 1
Dimensions of the Aortic Valve in Various Species (for Rb = 1)

	Rc	H	Φ°	α°	C_c	Hs	L_f	L_R	ds	hs	Authors
Man	1.0	1.42	32	22	0.34	0.71	2.48	1.4	1.46	1.76	Swanson and Clark[3]
Man		1.34	33				2.42				Sands et al.[6]
Man	0.9								1.12		Lozsadi and Arvay[9]
Man	0.75								1.71	2.02	Reid[10]
Man							2.65	1.2			Silver and Roberts[7]
Pig		1.3	28				2.2				Sands et al.[6]
Pig	1.1	*							1.12		Lozsadi and Arvay[9]
Pig	0.69							1.04	1.71	1.32	Reid[10]
Calf		1.16					2.18				Sands et al.[6]
Sheep		1.08					2.13				Sands et al.[6]
Sheep	0.67							0.93	1.6	1.15	Reid[10]
Dog	0.83	1.17	34	20		0.5					Thubrikar et al.[11]
Dog	0.7							1.0	1.74	1.4	Reid[10]
Ox	0.75							1.01	1.56	1.4	Reid[10]
Rabbit	0.71								1.74	1.42	Reid[10]
Range of values	0.7—1.1	1.1—1.4	28—34	20—22	0.34	0.5—0.7	2.13—2.6	1—1.4	1.1—1.7	1.2—2	

(b)

Figure 2.3: Aortic valve geometric parameters
Many geometric parameters define the anatomy of the aortic valve, such as a) Rc – commissure radius, H – valve height, α – bottom leaflet surface angle, Φ – leaflet free edge angle, c_c – coaptation height, Hs – commissure height, hs – sinus height, Rb – base radius, ds – sinus radius. b) Typical ranges are given for different species (figure taken from [9]).

2.1.2 Aortic Valve Physiology

Bulk Aortic Valve Hemodynamics

Since the left ventricle is responsible for pumping blood to the entire body, rather than just the lungs, the load requirements of the left side of the heart are greater than those of the right side. Subsequently, the aortic valve sees the highest pressures of any heart valve. These pressures reach up to 120mmHg in a healthy human. With a resting heart rate of 60bpm and a stroke volume of 70 mL, average cardiac output is around 4.2 L/min, with peak flow rates reaching near 30 L/min. Figure 2.4 is called the Wigger's diagram and displays useful pressure and volume information regarding the left side of the heart as well as electrical and acoustic signals that occur throughout the cardiac cycle.

In an average human lifetime, the aortic valve will open and close approximately 3 billion times. Therefore, even slight disruptions in the mechanical environment of this valve can have severe repercussions for patient health.

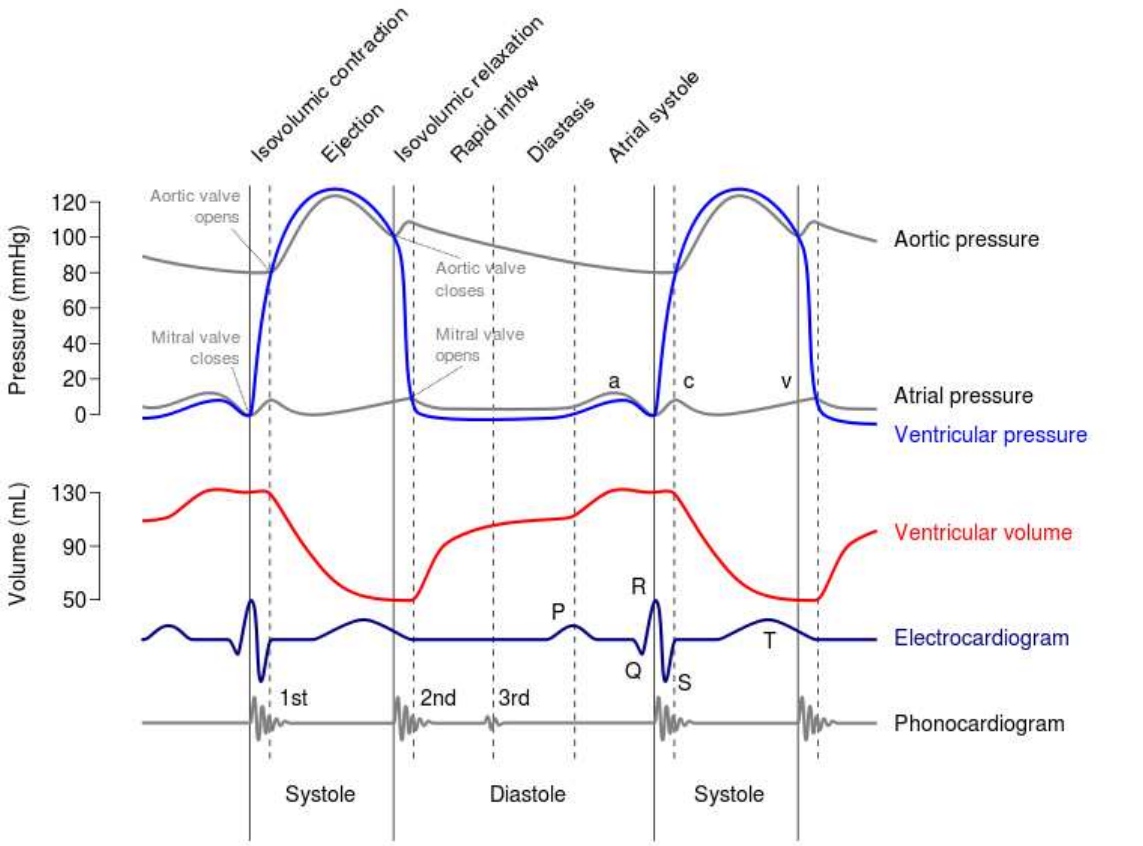

Figure 2.4: Wigger's diagram
Pressures and volume change across the aortic valve are shown as well as electrical signals throughout the cardiac cycle (figure taken from [10])

Detailed Aortic Valve Hemodynamics – The Aortic Sinus Vortex

It is theorized that the purpose of the sinuses is to provide a space between the leaflets and the aortic wall in order to facilitate both coronary flow and smooth closure of the valve [12, 13]. In this space, recirculating flow develops due to interaction with the freestream jet, thus creating a systolic sinus vortex. Leonardo da Vinci is generally regarded as the first person to theorize and depict the sinus vortex (see Figure 2.5) [11]. While this vortex is a well-established flow feature [14], its spatiotemporal complexity has only recently been elucidated and studied [15]. These detailed fluid dynamics are important since fine-scale coherent structures govern the valve's precise mechanical environment and mechanics are strongly tied to valvular health.

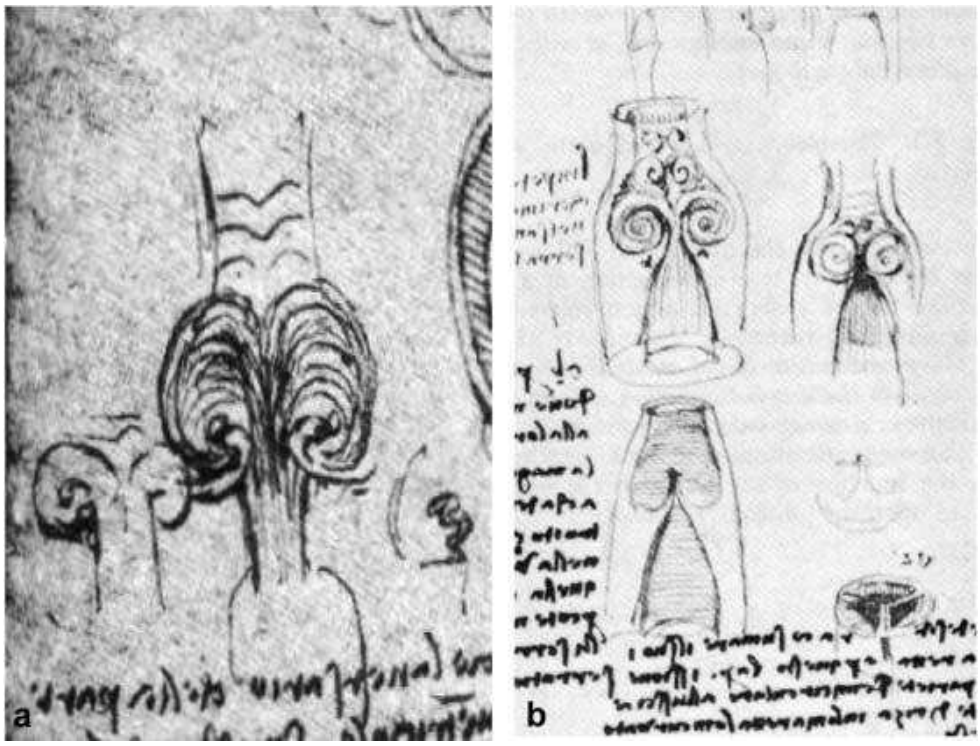

Figure 2.5: Leonardo da Vinci's sketches
Aortic sinus vortices depicted by da Vinci. Whether these sketches illustrate an experimental setup or not is unknown, but many studies have built upon the theory illustrated here (figure taken from [11])

Leaflet Mechanical Stresses

The aortic valve is exposed to a complex mechanical environment, which leads to time-varying fluid and structural stresses on the leaflets. These stresses have been shown to regulate disease, so details of mechanical bending stresses and fluid shear stresses on the leaflets are of interest.

Fluid shear stress is generally much higher along the ventricularis than on the fibrosa. Additionally, direction of shear is somewhat oscillatory on the aortic side of the valve leaflet, while it is unidirectional on the ventricular side. Conversely, mechanical bending stresses are generally highest on the aortic side of the leaflets, near the line of attachment to the aortic root [2].

Coronary Hemodynamics

A typical coronary flow waveform is presented in Figure 2.6 [16]. The initial peak in flow is due to the sharp rise in aortic pressure at the beginning of systole (A-B). Flow is then reduced once the myocardium is fully contracted since this causes constriction of the vessels (B-C). Upon diastole, the myocardium is relaxed, which reduces resistance in the coronary arteries and thus is responsible for the second peak in the waveform despite reduced pressure in the aorta at this time point relative to systole (D). Flow gradually declines with a coinciding decrease in aortic pressure throughout diastole (D-E-A).

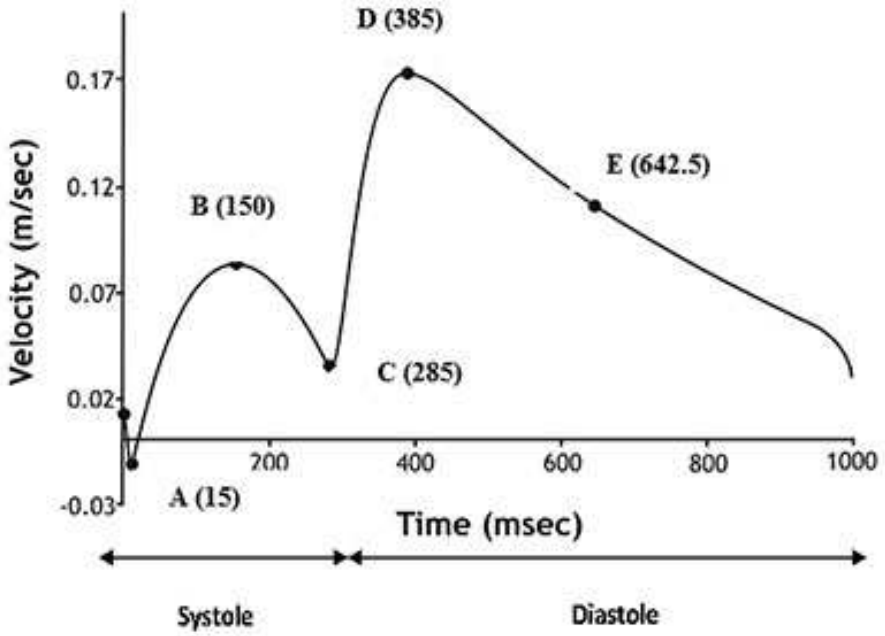

Figure 2.6: Coronary artery flow waveform
An average flow waveform for the left coronary artery is shown with certain time points of interest marked (figure taken from [16])

2.1.3 Aortic Valve Pathology and Congenital Anomalies

Calcific Aortic Stenosis

Aortic stenosis is a condition in which the valve is not able to open fully. This is often caused by calcification and therefore stiffening of the leaflets, as shown in Figure 2.7. While the exact causes of stenosis are unknown, strong correlations exist between calcification and mechanical factors, such as fluid shear and structural stresses. In addition, calcific lesions are similar to those of atherosclerosis, so it has been hypothesized that similar hemodynamic conditions could lead to both vascular and valvular calcification [2, 17].

Regardless of the cause, certain biological patterns are common in almost all calcific lesions. One of the earliest and most telling signs of calcification is inflammation of vavlular endothelial cells (VECs), which is often determined by presence of macrophages, T lymphocytes, and/or adhesion molecules [2, 17, 18]. Endothelial activation can then lead to a cascade of other events that promote development of calcification [19]. Additionally, recent studies have identified the calcification process as active, rather than passive, due to development of an osteogenic phenotype within the leaflet fibrosa similar to that of embryonic bone formation [18]. However, cell apoptosis is also present in diseased valve leaflets, so the process could be both active and passive.

Regardless of the mechanism, early detection of calcific aortic stenosis is difficult and no treatments exist to reverse its course [18]. Since even mild calcification is associated with an increased mortality risk [20], an understanding of the mechanisms that cause this disease is crucial for developing therapies.

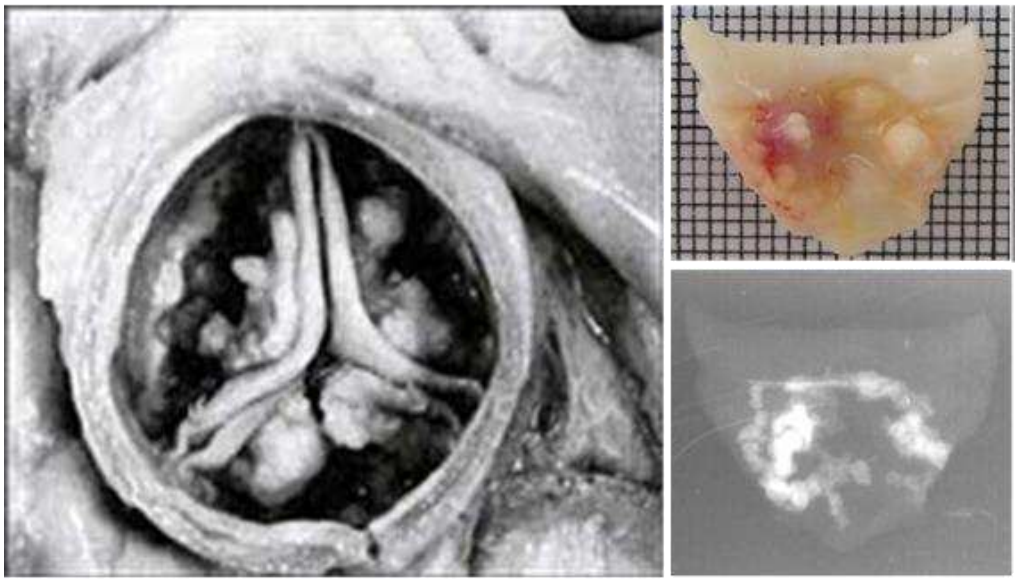

Figure 2.7: Calcific aortic stenosis
Images of diseased aortic valve leaflets with calcific nodules, whose relative stiffness prevent complete opening of the valve, thus causing stenosis (figure taken from [21])

Congenital Anomalies

One example of an aortic valve congenital anomaly is a bicuspid valve . In this case, there are two, rather than three, leaflets. One of the leaflets is larger than the other and generally comprises what would be the right and left coronary leaflets, with a raphe in place of the commissure (see Figure 2.8). This condition is present in approximately 0.9 to 2% of the population [22] and these types of valves are more prone to calcification than their tri-leaflet counterparts, likely due to altered hemodynamics [23, 24].

Anomalous coronary ostia locations have also been discovered. A study by Lee et al found 1.7% of patients undergoing coronary angiography to have some type of coronary artery anomaly [25]. An example of one such anomaly is an ostium location above the sinotubular junction on the wall of the aorta [26]. Other reported cases have found ostia that are still within

a sinus but are displaced horizontally toward the commissure [27]. Furthermore, two coronary arteries have even been noted to originate from the same sinus [25].

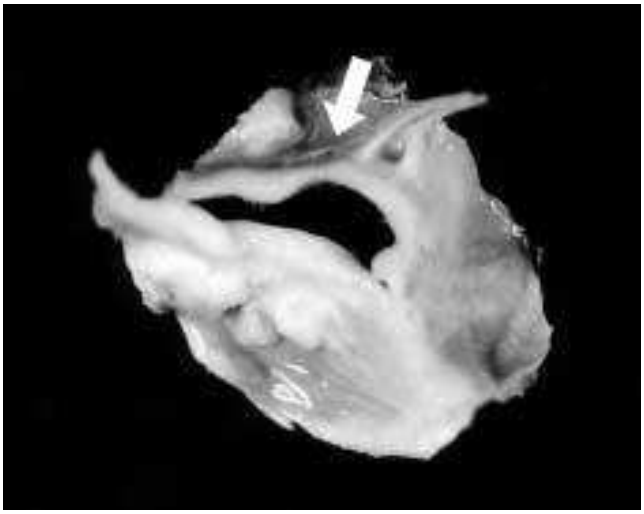

Figure 2.8: Bicuspid aortic valve
Image of an excised bicuspid aortic valve; arrow depicts raphe (figure taken from [23])

Hemodynamic Pathologies

In addition to anatomical anomalies, physiological conditions also exist that yield hemodynamic parameter values outside of normal ranges. For example, hypertension involves significantly elevated blood pressures that are pathological or reflect a diseased state. Additionally, elevated or reduced heart rates – tachycardia and bradycardia, respectively – are often indicative of cardiac dysfunction. Peak aortic flow time can occur at different systolic times and this precise timing could have implications for disease. Specifically, a later peak flow time can be correlated to heart failure, a condition in which cardiac output is too low to meet the oxygen demands of body tissues.

Another hemodynamic factor that has implications for valvular health is that of pressure waves and their reflections within the arterial system. These wave reflections come from various

locations throughout the systemic vasculature. An initial reflection from the aortic pulse wave can cause an inflection point in the systolic pressure waveform [28, 29], which is often the case in older patients, or can lead to an increase in the diastolic pressure curve, which more often occurs in younger patients [30]. A later return of the reflected pressure wave (i.e. during diastole) could help facilitate coronary perfusion, so this timing appears more beneficial. It has also been argued that secondary reflections returning back off of the aortic valve can further contribute to increased aortic pressure during diastole. The influence from these reflected waves can increase greatly with arterial and/or valvular stiffening, so accurately modeling them could become important in studies dealing with these types of diseases.

2.1.4 Prosthetic Aortic Valves

There are numerous types of prosthetic aortic valves available to replace a failing valve. The two main categories of these valves are mechanical and bioprosthetic. Mechanical valves are more durable but also require anticoagulation therapy to prevent thrombosis. On the other hand, bioprosthetic valves offer better hemodynamic performance than mechanical valves but are prone to structural deterioration [31, 32].

Many bioprosthetic valve variations have been developed. Stented valves aim to mimic the anatomy of the native valve. Stentless valves were created to help improve hemodynamics and durability while sutureless valves are meant to decrease implantation time. Recently, percutaneous valves have become an alternative for valve replacement candidates who are at a high surgical risk. Different materials have been used for these different valve designs including porcine valve tissue as well as bovine and equine pericardium. Figure 2.9 shows examples of these different types of valves [33].

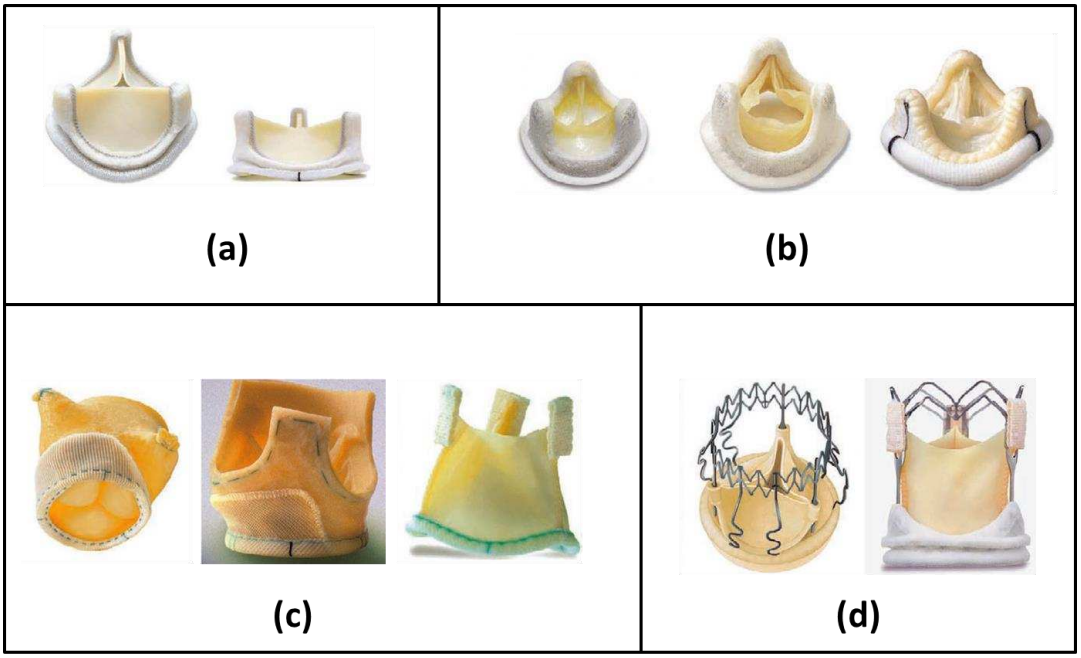

Figure 2.9: Bioprosthetic aortic valves
a) Surgical valves made of pericardium (generally bovine) b) Surgical valves made from porcine leaflets c) Stentless valves and d) Sutureless valves (figure taken from [34])

2.2 Links between Mechanical Environment and Disease

Since valvular disease is generally initiated on a cellular level, it is difficult to determine what clinical parameters may cause it. One step towards linking cellular biology and patient clinical parameters is to elucidate valve tissue responses to their surrounding hemodynamic conditions.

Development of calcification is strongly linked to valvular hemodynamics. Specifically, sinus flow is of interest since calcification preferentially develops on the aortic side of the valve [35]. Additionally, the non-coronary leaflet often calcifies first [36], so detailed information on flow differences between the sinuses is crucial for understanding hemodynamic influences on disease in the aortic valve. For example, many ex vivo studies have been conducted on excised leaflet tissue to examine the individual contribution of either wall shear stress [36-40] or mechanical stretching [41, 42] to calcification-triggering factors (Figure 2.10) [43]. In one study,

Sun et al created a tissue bioreactor involving a spinning disk immersed in a cell culture medium. Different angular velocity profiles were prescribed to impose different shear stress environments on the leaflet samples. Another study by Balachandran et al involved mechanical stretching of excised leaflet tissue. In this case, tissue samples were stretched at different magnitudes.

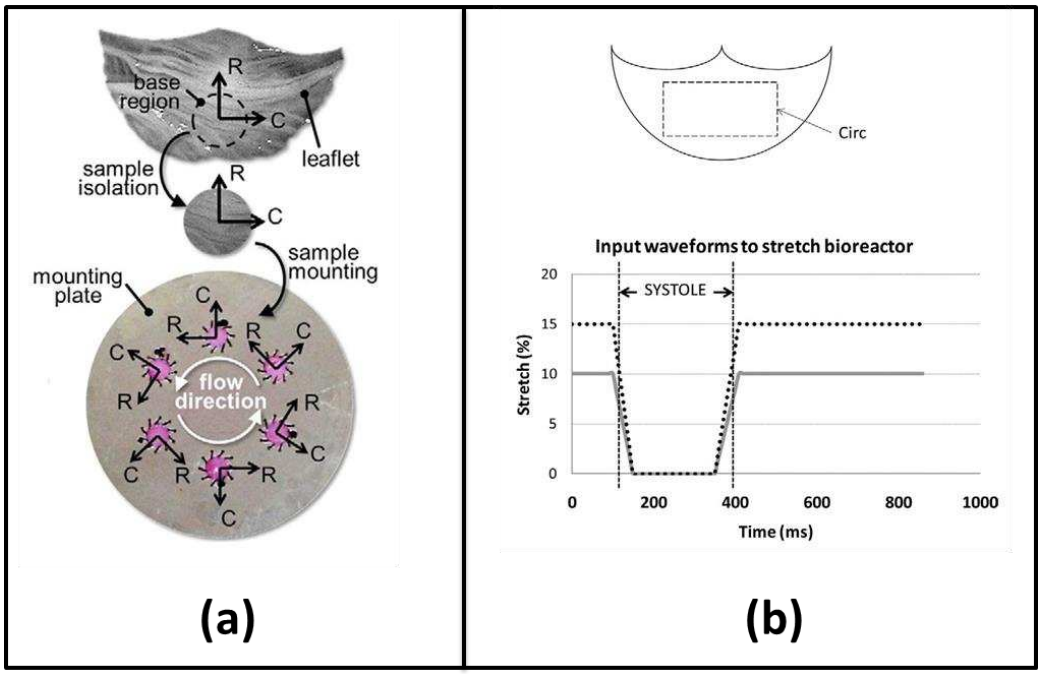

Figure 2.10: Ex vivo aortic valve leaflet studies
a) Effects of shear stress patterns (figure taken from [38]) and b) mechanical stretching patterns (figure taken from [41]) on calcification triggering mechanisms

Investigators identified low or oscillatory shear stress and increased mechanical strain as potential risk factors for CAVD. Furthermore, fluid shear stress patterns similar to those on the fibrosa, rather than the ventricularis, were shown to generate cell responses more strongly linked to stenosis [36, 38]. Additionally, it has been shown that bicuspid valves, which have significantly different sinus hemodynamics, typically calcify earlier and more often than “normal”, tricuspid counterparts [44, 45]. These correlations all support the notion that mechanics do indeed regulate calcification.

Other valve pathologies, besides calcific aortic stenosis, can also be tied to mechanics. For example, thrombus formation can occur in stagnation zones that develop due to altered hemodynamics from prosthetic valve implantation. Thrombosis after TAVI valve implantation, in particular, has sometimes led to stroke [46, 47], while numerous other complications related to prosthetic valve implantation also exist. These complications, which are often due to difficulties with valve placement, include paravalvular regurgitation, breaking off of tissue, and blockage of coronary arteries [46-49] as well as surgical difficulties during the valve replacement procedure.

2.3 Regulation of Mechanical Environment by Hemodynamics

Given that mechanical stresses can regulate disease, it is therefore important to understand the overall hemodynamics that regulate these stresses. This helps form one link in the chain between valvular disease and patient clinical parameters. Many current studies are focused on establishing causal relationships between global hemodynamics and leaflet stresses.

One method commonly used to visualize aortic hemodynamics is in vitro experimentation. Most studies of this nature utilize a pumping loop to simulate physiological flow conditions across a model aortic valve (Figure 2.11). Prosthetic valves are often used as models and are generally contained within a clear chamber so hemodynamics can be visualized. Leonardo da Vinci was perhaps the first person to conduct such experiments using a glass mock aorta (although only sketches of such equipment are available today) [11], however much more sophisticated techniques have been developed recently. One of these techniques is particle image velocimetry (PIV), which provides quantitative information on flow patterns near the aortic valve. Using PIV, many different aspects of aortic valve morphology and hemodynamics have been studied. For example, native valve hemodynamics have been elucidated to determine the fine-

scale flow features within the sinuses and/or to use as a baseline for comparison to hemodynamics under different valve conditions [15].

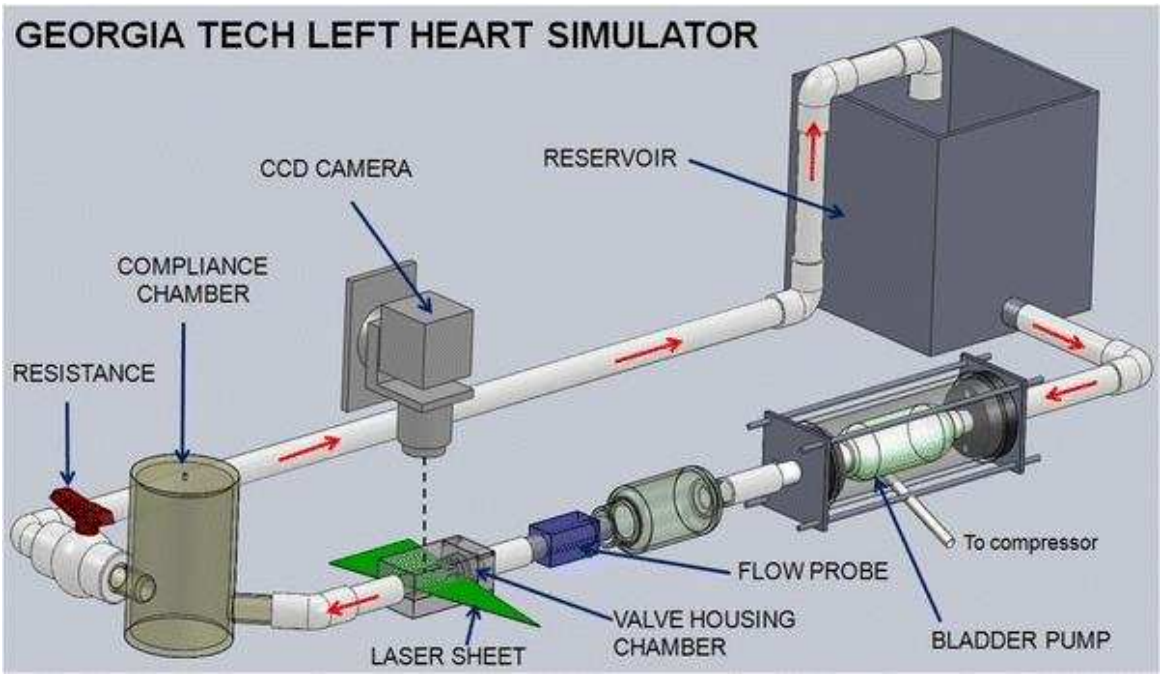

Figure 2.11: Diagram of the Georgia Tech Left Heart Simulator
This schematic displays many standard flow loop components, which are used to collectively impose physiological pressures and flow rates across the aortic valve. Orientation of camera and laser sheet for PIV are also shown (figure taken from [50]).

Some different conditions that have been tested in vitro include bicuspid valves, calcified valves, various types of prosthetic valves, and absence of Valsalva sinuses. Investigators have focused on different aspects and scales of flow through these valve models depending on the particular study, from overall pressure drop and flow rate measurements to detailed sinus hemodynamics. For example, Bottio et al. examined transvalvular pressure gradients for a bioprosthetic valve placed in different Dacron conduits with and without sinuses [51]. At a slightly finer scale, Lim et al. calculated Reynolds stresses, and therefore implications for blood damage, of flow just downstream of a porcine bioprosthesis [52]. And at even finer scales, the effects of a bicuspid versus tricuspid valve on sinus hemodynamics were elucidated by

Saikrishnan et al. [50]. While many of these studies have used surgical bioprostheses as model native valves, much recent focus has been placed on transcatheter aortic valve implantations due to their potential as a minimally invasive alternative to open-heart surgery. Ducci et al. compared native and TAVI valves to understand the hemodynamic effects of this type of prosthesis [53], while further work has been conducted to determine the unique flow characteristics that arise due to eccentric TAVI deployment [54] or axially displaced TAVI positioning [48].

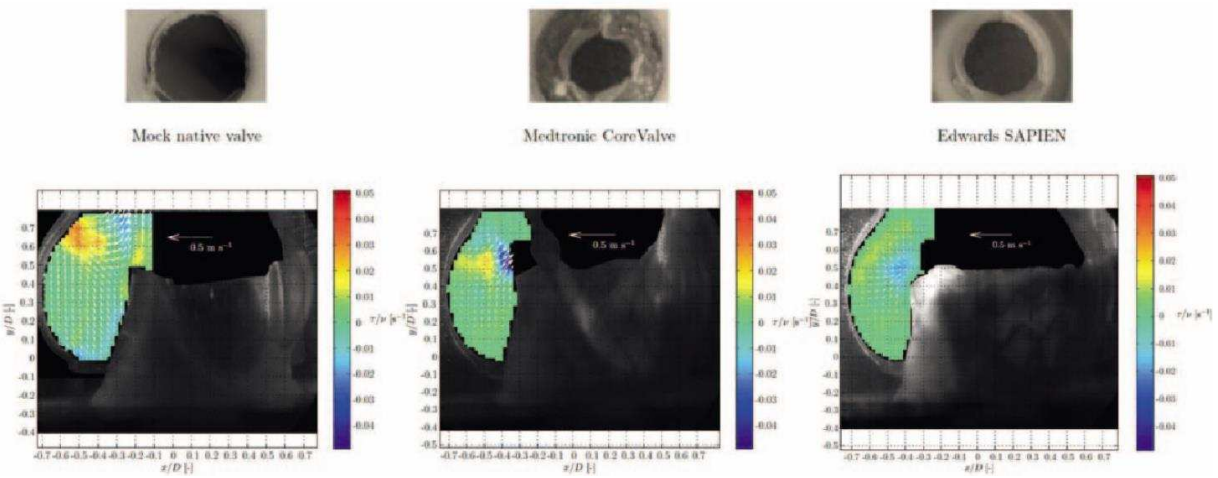

Figure 2.12: Native and TAVI sinus hemodynamics from Ducci et al.
Sinus velocity vectors and vorticity contours are shown for three different valve cases – a mock native valve and two types of TAVI valves (figure taken from [53])

While these types of in vitro experimental techniques are well-suited for elucidating complex hemodynamics, they still contain limitations. For example, most experimental flow loops are unable to accurately replicate the pressure wave reflections that occur in vivo. However, bulk hemodynamics are generally still preserved so average pressure and flow cases can still be simulated. In addition, in vitro visualization techniques often lack the ability to acquire certain information. One example of such information is wall shear stress, which is a useful parameter due to its implications for disease. While experimental techniques have been developed to calculate wall shear stress on the valve leaflets [55, 56], they are still lacking due to spatial

constraints (i.e. only two-dimensional) and also face difficulties during leaflet opening and closing phases.

One method that gives more detailed insight into spatiotemporal shear stress patterns is computational fluid dynamics (CFD). There have been many CFD models developed to explore leaflet shear stresses [57-59]. However, these types of simulations possess their own limitations, namely the inability to accurately model leaflet motion. To address this issue, fluid-structure interaction (FSI) models (see Figure 2.13) have been developed to simulate leaflet motion based on hemodynamics, while still accurately capturing flow patterns through a changing geometry [60-62]. An additional advantage of these FSI models is their ability to calculate leaflet stresses and strains, although the viscoelastic nature of valve tissue creates difficulties in approximating material properties, which is an active area of research in itself [63].

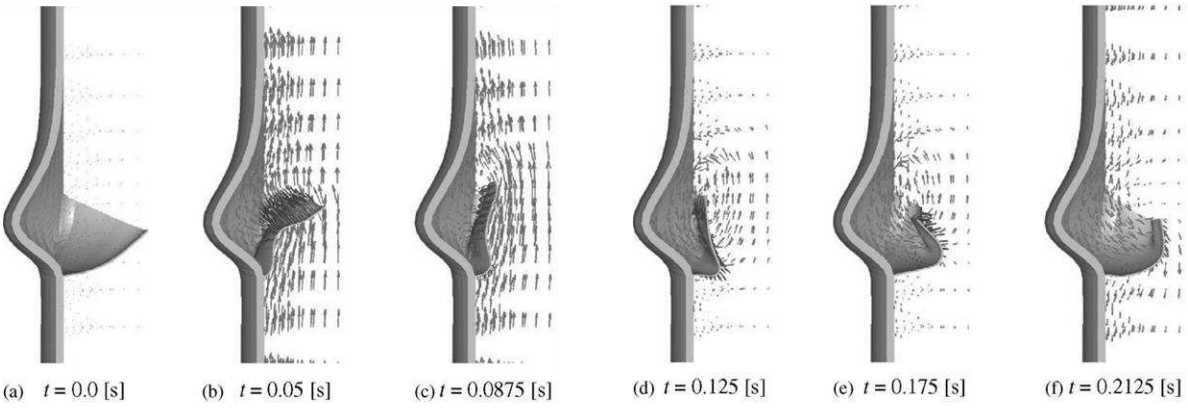

Figure 2.13: Fluid-structure interaction model results from De Hart et al.
Results from a fluid-structure interaction study of the native aortic valve. Images show a cutaway through one sinus (figure taken from [61]).

One additional method for studying aortic valve hemodynamics is medical imaging. Recent advances in 4D MRI have made possible in vivo imaging at multiple time points across the cardiac cycle. These studies shed light on patient-specific aortic valve hemodynamics [64, 65]. A depiction of this method is given in Figure 2.14. The advantage of this method is that actual

aortic geometry is studied and no modeling assumptions are used for hemodynamics or valve kinematics. However, limitations in spatial and temporal resolution prevent detailed viewing of hemodynamics near the valve leaflets, so in vitro experimental and computational methods are still widely used.

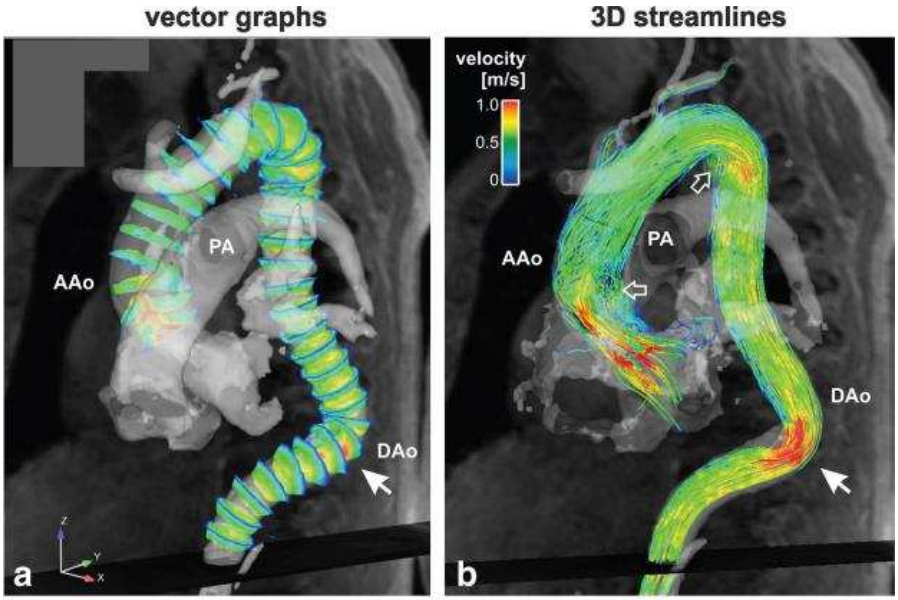

Figure 2.14: Velocity results from 4D MRI study by Markl
Velocity vectors and streamlines were computed from 4D MRI data in vivo (figure taken from [65])

There are a wide variety of aortic valve parameters that have been studied at different spatial and temporal scales. Table 2-1 is a sampling of recent work involving in vivo and in vitro visualization of hemodynamics, giving insight into both the resolution and dynamic similarity capabilities of different studies.

Table 2-1: Spatial and temporal resolution of aortic valve studies
Numerous in vitro and in vivo aortic valve visualization studies are summarized with regard to their spatiotemporal resolution capabilities

Author(s)	Year	Technique	Temporal Resolution	Spatial Resolution
Saikrishnan et al. [50]	2012	PIV	50 µs (systole) 1000 µs (diastole)	16.6 microns/pixel 1600 X 1200 px
		Echo	250 fps	1280 X 1024 px
Leo et al. [66]	2006	PIV	75 µs (systole) 500 µs (diastole)	0.4 mm
Querzoli et al. [67]	2010	PIV	250 Hz	1.34 mm
Falahatpisheh, Kheradvar [68]	2012	Digital PIV	1000 Hz	1280 X 1024 px
Toger, Kanski, Carlsson [69]	2012	4D PC-MRI	50 ms	3 X 3 X 3 mm
Bellofiore, Donohue, Quinlan [70]	2011	PIV (scaled up)	1754 Hz (scaled)	120 µm (scaled)
Kaminsky, Kallweit, Weber [71]	2007	PIV	3000 Hz	1.2 mm 1024 X 1024 px
Strecker, Harloff, Wallis [64]	2012	4D MRI	40.8 ms	1.7 X 2.0 X 2.2 mm
Markl, Frydrychowicz, Kozerke, Hope [65]	2012	4D MRI	40-50 ms	2-2.5 mm
Seaman, Akingba, Sucosky [72]	2014	PIV	22 Hz	1648 X 1214 px
Keshavarz-Motamed et al. [73]	2014	PIV	1000 Hz	1632 X 1200 px

2.4 Regulation of Hemodynamics by Anatomic Valve Conditions and Coronary Flow

The relationship between patient-specific anatomy and physiology forms the final link in the chain between clinical parameters and valvular disease. By linking patient parameters to hemodynamics, and then hemodynamics to calcification-triggering stresses, it may be possible to determine clinical causes of aortic stenosis and also to develop therapies for this disease. Elucidating the relationships between different anatomic and flow conditions that may arise in different patients is the goal of this work. This section gives a brief introduction into different factors that could affect hemodynamics and that have therefore been studied as a part of this research project.

2.4.1 Variation in Anatomy and Physiology

As is the case in nearly any biomedical study, a single geometric model of the aortic valve is not sufficient to represent variations in anatomy across multiple subjects. The aortic root is defined by a number of geometric parameters, all of which can vary from patient to patient. Asymmetries are also present that can lead to variations within an individual. Therefore, it is important to recognize these differences and incorporate them when modeling aortic valve mechanics and hemodynamics [74].

One parameter that is indicative of overall valve size is aortic diameter. Variations in this dimension are often correlated to patient factors such as age and gender [75] and also correspond to variations in other aortic root dimensions. These include, but are not limited to, annulus diameter, sinus radius, and sinus height – three parameters of interest for this particular study focused on sinus hemodynamics. Relative sizes of these different parameters can also vary [9]. One such relative parameter is sinus aspect ratio, which is the ratio of sinus height to width. Sinus width is often referred to as sinus radius and is sometimes defined as the farthest

distance from the aortic axis to the sinus wall [76]. Another definition is the difference in radius between the aorta and the farthest point on the sinus wall. Additionally, ratio of annular radius to aortic radius can vary patient to patient. These differences in anatomy can lead to differences in hemodynamic parameters, such as stroke volume and therefore cardiac output. Locations of coronary ostia as well as strength of coronary flow are other geometric and flow parameters that vary based on the individual [26]. The unique hemodynamics that occur due to these differences in geometry and flow characteristics are one focus of this work.

2.4.2 Coronary Flow

One such factor that could influence sinus vorticity dynamics, and therefore valve health, is the presence of coronary ostia. The non-coronary cusp often calcifies first, and it has been hypothesized that the reason for this is reduced shear stress from a lack of diastolic coronary flow [2]. Some studies have focused on coronary flow in the context of aortic sinuses. For example, an experimental study by de Paulis et al. examined coronary flow as regulated by presence and/or shape of sinuses of Valsalva [77]. Similarly, Nobari et al. aimed to include coronary arteries in computational models of the aortic valve [78]. However, no studies to date have investigated in detail the impacts of coronary arteries on sinus vortex dynamics throughout the cardiac cycle. Likewise, there exist patient-to-patient variations in coronary parameters, such as ostia locations, that could affect hemodynamics (Figure 2.15).

One aim of this study is to elucidate specific sinus hemodynamics that occur in both coronary and non-coronary sinuses. Therefore, new information gained from this work will contribute to a better understanding of aortic hemodynamics and could help educate surgeons and clinicians on a proper course of treatment for patients with, or at risk for, calcific aortic stenosis or other diseases affecting the aortic valve or coronary arteries.

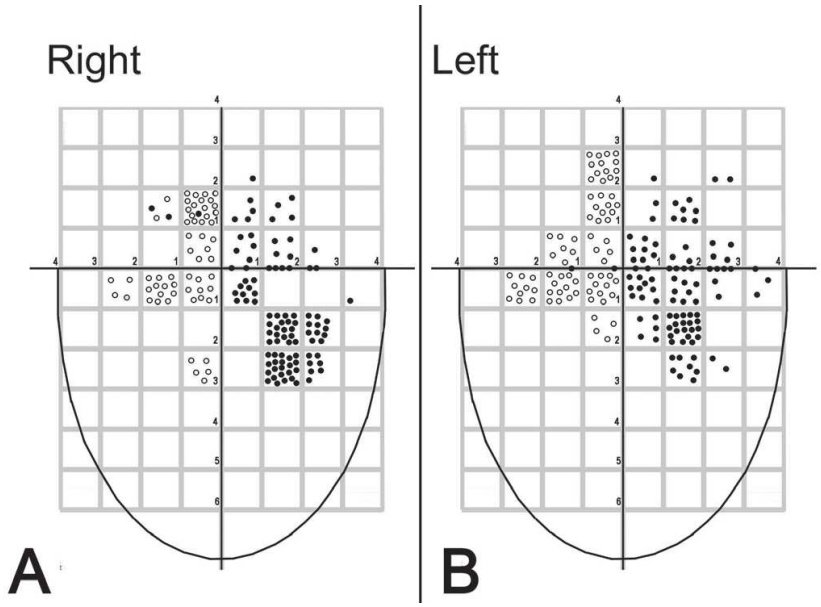

Figure 2.15: Variation in coronary ostia location
Depiction of coronary ostia locations arising from the A) right and B) left cusps. The reference point is at the commissural height along the sinus center plane (figure taken from [26])

2.4.3 Transcatheter Aortic Valve Implantations (TAVI)

Once calcification has progressed to the point of severe aortic stenosis and a patient has become symptomatic, valve replacement is generally recommended [79]. While prosthetic heart valves provide a remedy for stenosis, they still have significant drawbacks. One of these drawbacks is the highly invasive nature of open-heart surgery, which has recently been addressed through transcatheter aortic valve implantation (TAVI) [80]. However, this relatively new technology is currently only approved for patients with a high risk of surgical complications, such as elderly and those with severe comorbidities and/or hostile chest. This is due largely to a current lack of data in younger patients concerning long-term follow-up after TAVI implantation. Therefore, additional studies focusing on TAVI valve sinus hemodynamics are important for further development of this technology and use in younger patients.

Currently there are multiple types of TAVI valves in use across the United States and Europe (see Figure 2.16). Initial results are promising as these valves have shown huge improvements in hemodynamics over stenotic native valves and even slight improvements over stented and stentless surgical bioprostheses [82, 83] Additionally, a study by Smith et al found favorable results concerning intra-procedural deaths for TAVI procedures vs surgical operations on high risk patients [46]. Despite relative successes, however, there are still a number of complications associated with TAVI valves. Chief among these complications is difficulty of placement. This difficulty can lead to breaking off of tissue as well as numerous other detrimental effects [84].

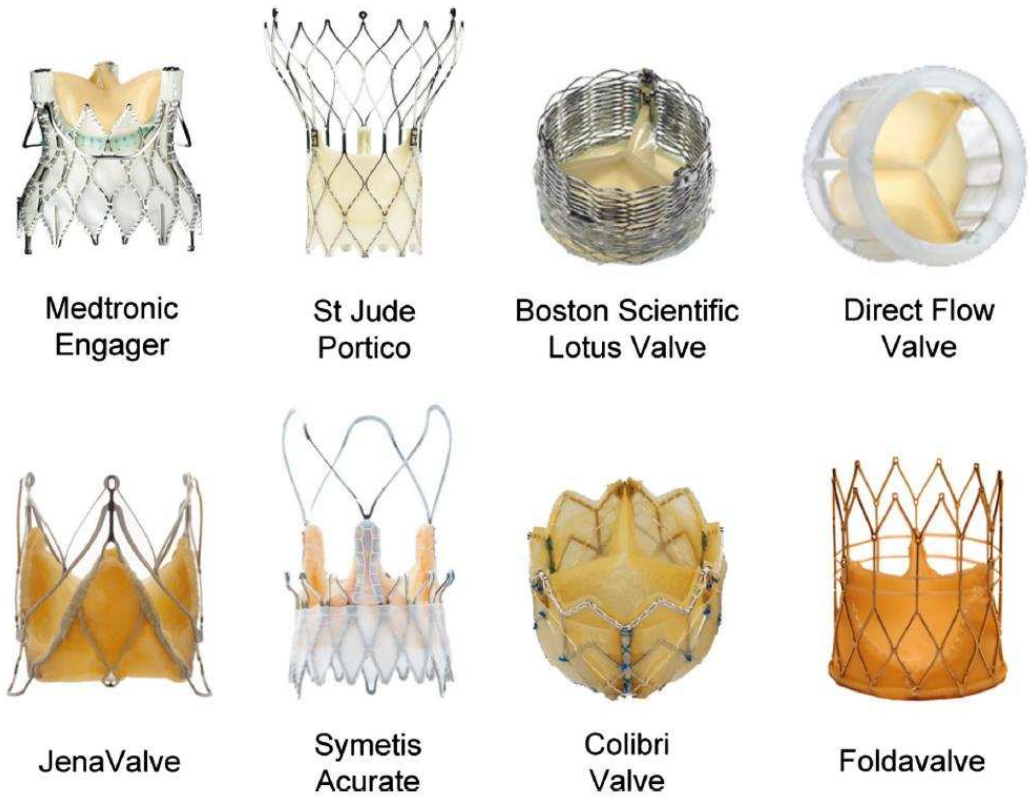

Figure 2.16: Examples of various types of TAVI valves
Many transcatheter valves have been developed or are currently in development thanks to promising results from Medtronic and Edwards versions of this technology (figure taken from [81])

For example, TAVI implantation requires precise pre-operative sizing of the aortic root to avoid blockage of coronary arteries [49]. Similarly, unfavorable valve placement, often due to ovoid shape and/or bulky calcifications, is generally acknowledged as a cause of paravalvular

regurgitation as well as unfavorable hemodynamic environments that leave the patient susceptible to stroke [46, 47] (see Figure 2.17). However, these studies mainly focus on short term outcomes, so it is feasible that similar problems may occur over time even with proper placement. Additionally, there is a current lack of knowledge regarding hemodynamic impacts due to TAVI-specific factors, such as stent presence and persistence of native leaflets in the coronary and non-coronary sinuses.

This study aims to evaluate the long term effects of TAVI valves, particularly from the standpoint of sinus hemodynamics since poor hemodynamics may result in a significant risk of stroke [86]. Such knowledge could influence clinical decisions regarding anticoagulation or anti-platelet post-operative treatments. Bioprosthetic valves, as opposed to mechanical valves, are being used in younger patients as technology progresses [87], so an understanding of long-term TAVI implications is vital.

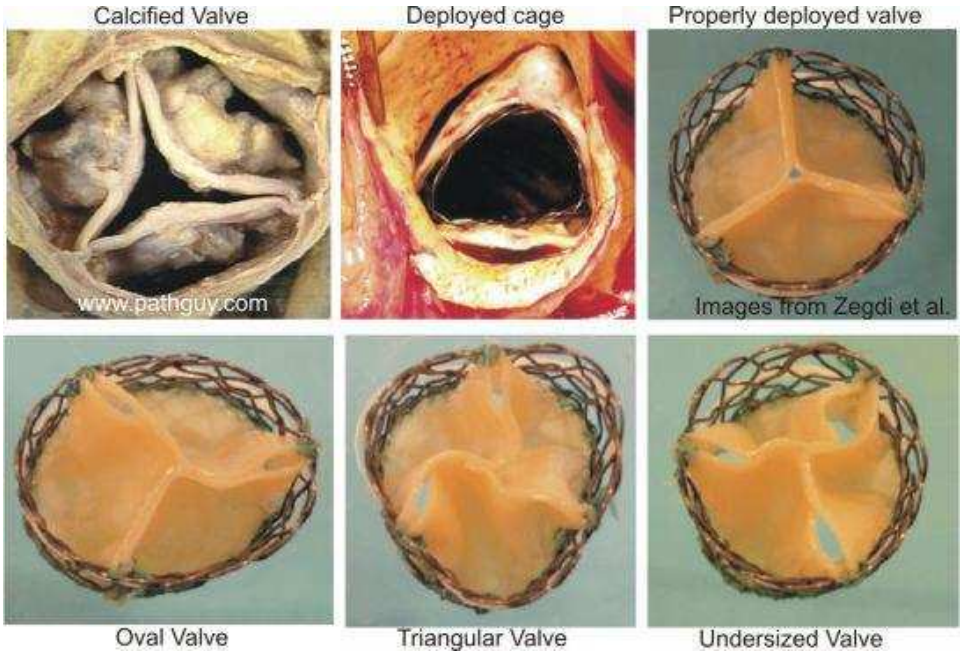

Figure 2.17: Difficulties in transcatheter valve deployment
Abnormalities in calcified valve geometry can lead to difficulties in transcatheter valve deployment, which often cause regurgitation (figure taken from [85])

2.4.4 Sutureless Aortic Valve Replacements

Patients with a high risk of surgical complications generally cannot undergo full open-heart surgery. Instead, these patients are often treated with transcatheter valve implantations. For some patients at slightly lower risk, however, open heart surgery is still feasible but remains challenging, mainly due to cardiopulmonary bypass time. Therefore, a decrease in valve replacement time could reduce complications and decrease morbidity and mortality [88, 89]. Likewise, some less invasive surgical techniques, such as mini-sternotomy (which involves a smaller incision of the breastbone than in a standard sternotomy), have been recommended for these moderately high risk patients [90]. However, some clinicians argue that this type of surgery is more challenging for surgeons and therefore requires longer cardiopulmonary bypass time [91-93], so this is another case where reduced procedural time would be beneficial [94]. To address this issue, sutureless valves have been developed to cut down on the time that a patient has to undergo surgery, and early findings have shown effectiveness of sutureless valves in this regard [95]. Figure 2.18 shows two examples of sutureless valves.

Figure 2.18: Sutureless valves
Two examples of sutureless valves are the) ATS 3F Enable and b) Sorin Perceval S. Radial forces from the stent frames, rather than sutures, are used to hold these valves in place (figure adapted from [34])

The ATS 3F Enable is a sutureless valve that is fabricated from a tubular structure – a design based on the theory that this shape is the most natural configuration for formation of an aortic valve. This theory is supported by finite element modeling which shows that a tube naturally forms an aortic valve when subjected to a physiological pressure gradient. Additionally, most of the leaflet stress due to this applied pressure load is distributed through the "belly" of the cusps, rather than at the commissures of the model (Figure 2.19). This stress distribution pattern is one design feature of the ATS 3F Enable and could decrease wear on the valve over time [96].

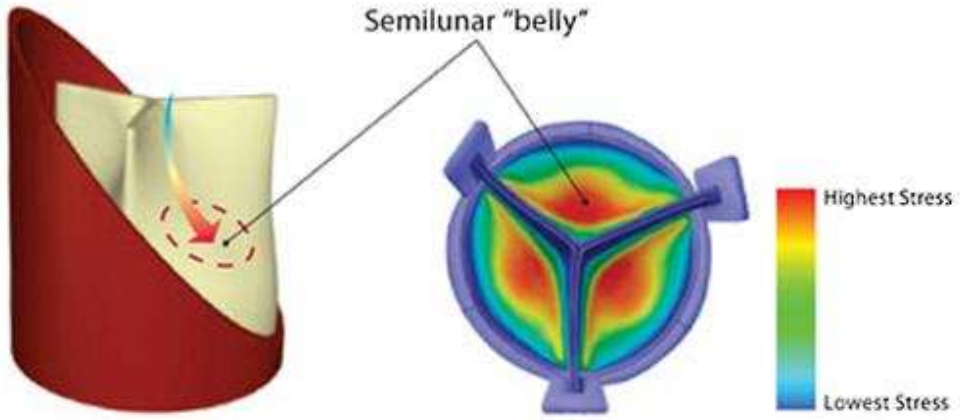

Figure 2.19: Sutureless valve stress distribution
Depiction of stress distribution along the leaflets of an ATS 3F Enable sutureless valve. This valve is designed to carry most stress through the "belly" of the leaflet rather than at the attachment points (figure taken from [96])

From a hemodynamics standpoint, sutureless valves have thus far demonstrated favorable performance relative to existing bioprosthetic valves. For example, the Perceval S valve showed good pressure gradient performance characteristics post-implantation [95]. Likewise, an in vitro study of the earlier generation, stentless ATS 3F Enable valve showed favorable velocity and shear characteristics compared to surgical and TAVI valves [97]. These results are expected to be similar to the newer sutureless valve since general morphology is the same between these two valve generations. Low prevalence of paravalvular leakage has also been noted [98]. Mortality rates are generally low considering the high-risk patients that undergo this

type of valve replacement. Different trials using the ATS 3F Enable valve showed mortality rates of 12.5% after 90 days [98] and 13.7% after one year [99]. A clinical trial involving the Perceval S yielded a valve-related mortality after one year of 6.7% [100].

3. SPECIFIC AIM 1

Develop methodologies for quantifying hemodynamics within the aortic sinuses

3.1 Chapter Introduction

The overall goal of Specific Aim 1 was to build a framework for modeling different valve anatomies under varying flow conditions. This was accomplished through development of both experimental and computational methods. Experimentally, this involved creating in vitro flow setups to replicate physiological valve environments, and also to use particle image velocimetry (PIV) to capture sinus flow features within these setups. Computationally, both 2D and 3D models were created and flow was simulated using the computational fluid dynamics (CFD) solver ANSYS Fluent. Simulations are used to test for agreement with experiments and also to provide some 3D perspective for experiments that can only capture a 2D slice. The following sections describe general methodologies that form the basis of this work. Detailed parameters and/or novel concepts developed for other specific aims are explained in the corresponding chapter. This work has led to 1 conference publication [101] and 1 journal publication [15].

3.2 Experimental Methods

3.2.1 Flow Loops

In order to study the aortic valve in vitro, some type of flow replicating setup is needed to simulate blood flow. These devices are widely used and have been referred to as pulse duplicators and left heart simulators, for example. In this work the setup will be called a flow loop. Regardless of nomenclature, these devices all serve the same purpose: to impose certain blood pressures and flow rates across the aortic valve that are within physiological ranges but are also modifiable.

Different types of custom flow loops were used in this work. Figure 3.1 is a schematic of a flow loop driven by a bladder pump. This pump functions due to pressurization and depressurization of air. Specifically, a flexible tube-like bladder forms part of the flow path, and this bladder is contained within a rigid, airtight chamber. This rigid chamber has two ports – one to a

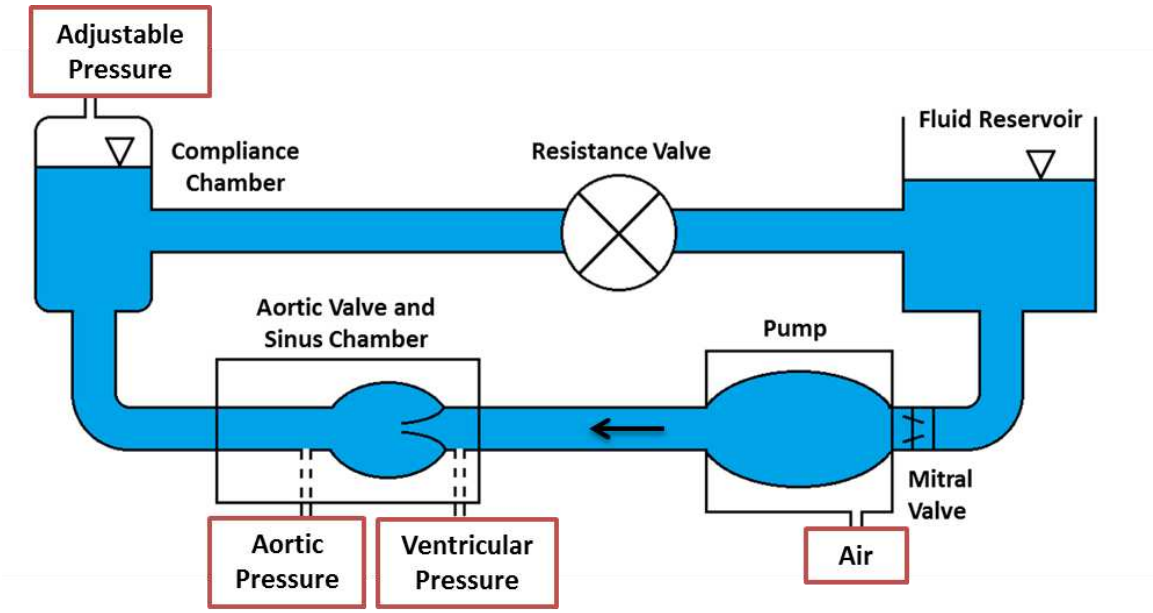

Figure 3.1: Bladder pump flow loop schematic
Multiple components were used to simulate physiological flow conditions across the aortic valve. Key components depicted in the figure include a pump, compliance chamber, and resistance valve.

pressurized air line and one to a vacuum line. The flow of air and vacuum to the chamber is metered by solenoid valves which are controlled by a relay switch connected to an in-house LabVIEW program. By alternately opening and closing the air and vacuum valves, the chamber can be pressurized and depressurized at user-specified intervals of time. The pressurization causes the bladder to constrict, and expel fluid, while the depressurization allows the bladder to expand. A one-way valve is included between the bladder and fluid reservoir to keep fluid motion in one direction. This valve is analogous to the mitral valve in the body.

Additional flow loop components are also shown in Figure 3.1. Downstream of the pump is the aortic valve, which in this in vitro setup is contained within a clear, acrylic chamber for viewing purposes. Multiple chambers were fabricated to hold different valves, and these chambers are explained in more detail in the next section. After the aortic valve is a compliance chamber. This added compliance is necessary to smooth out what would otherwise be pronounced spikes and troughs in the aortic pressure waveform. The compliance chamber works by mimicking the elastic nature of the aorta and other blood vessels. Instead of flexible conduits, however, there is a pocket of air within the chamber that absorbs some pressure during systole and then releases this stored energy during diastole. Therefore, the more compliance that is present in the system, the more the pulsatile pump will act like a steady flow pump. The last component in the flow loop is a resistance valve. This valve is necessary to impose load on the pump and therefore generate physiological pressure magnitudes. This is analogous to pressure losses that occur due to frictional resistance throughout the blood vessels of the body.

A second flow loop was also used that was driven by a piston pump, rather than a bladder pump. Two different pump types were employed due to the unique advantages and disadvantages of each one. For example, the bladder pump functions more like an actual ventricle and yields smoother pressure and flow curves, however the piston pump is more finely adjustable. Therefore, the bladder pump was initially used for baseline tests and the piston pump was used when more control was needed over flow profiles. Figure 3.2 shows a schematic of the piston pump flow loop that was used. Aside from the type of pump, all other functional components in this flow loop are the same as in the bladder pump flow loop.

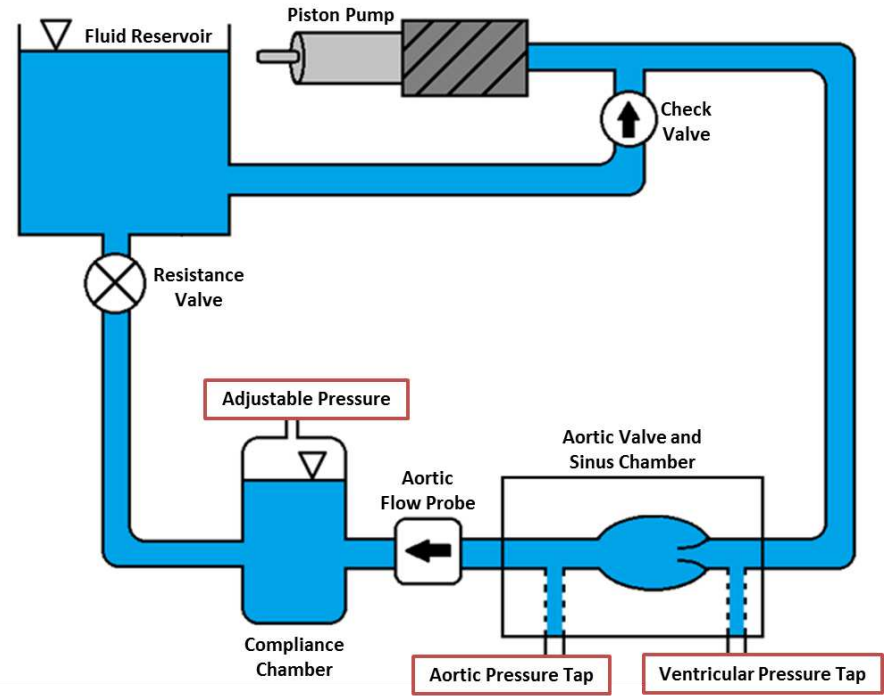

Figure 3.2: Piston pump flow loop schematic
This schematic for the piston pump flow loop shows similar components to the bladder pump loop. The major advantage of this loop is the ability to prescribe the exact motion of the piston.

3.2.2 Flow Parameters

The working fluid used was a 60/40 water/glycerin mixture. This specific ratio of water to glycerin yields a similar density and viscosity to that of blood (water/glycerin mixture: $\rho = 1090$ kg/m^3 and $\nu = 3.88$ cSt).

Pressure data was captured using Validyne pressure transducers (Validyne Engineering Corp., Northridge, CA) while flow waveforms were generated from ultrasonic flow probes (Transonic, Ithaca, NY), both in conjunction with National Instruments data acquisition hardware and software. Experimental pressure and flow data obtained from the bladder pump flow loop are shown in Figure 3.3. As shown in the figure, typical aortic pressure measurements were approximately 110/80 mmHg with a peak flow rate just over 30 L/min.

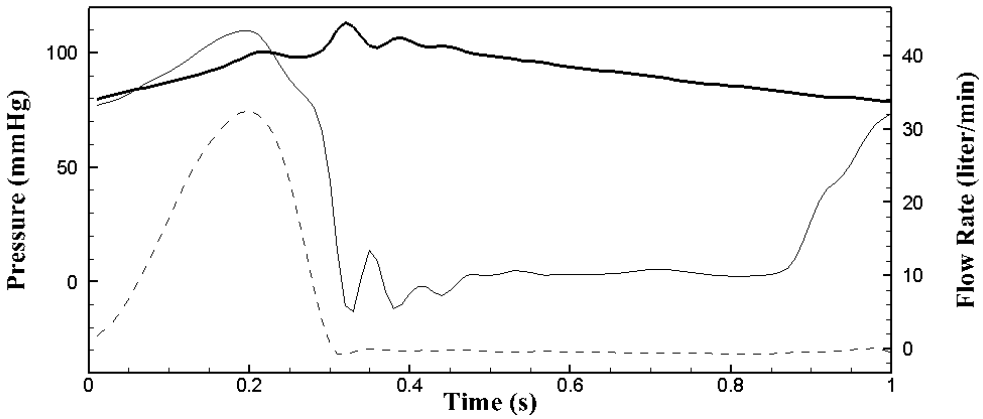

Figure 3.3: Experimental pressure and flow waveforms
Pressure and flow rate curves were generated after tuning the flow loop to replicate physiological conditions

3.2.3 Valve Model and Sinus Chamber

A clear, acrylic valve chamber was used to attach the model valve to the flow loop, which is shown in Figure 3.4a (detailed dimensions are given in Appendix I). This chamber was designed and fabricated based on a previous in vitro aortic valve study by Yap et al [102]. Dimensions of this chamber yielded a sinus radius of 13.5 mm, a sinus height of 16.5 mm, and an aortic radius of 9 mm. The aortic valve used was a 23mm Medtronic Hancock II porcine

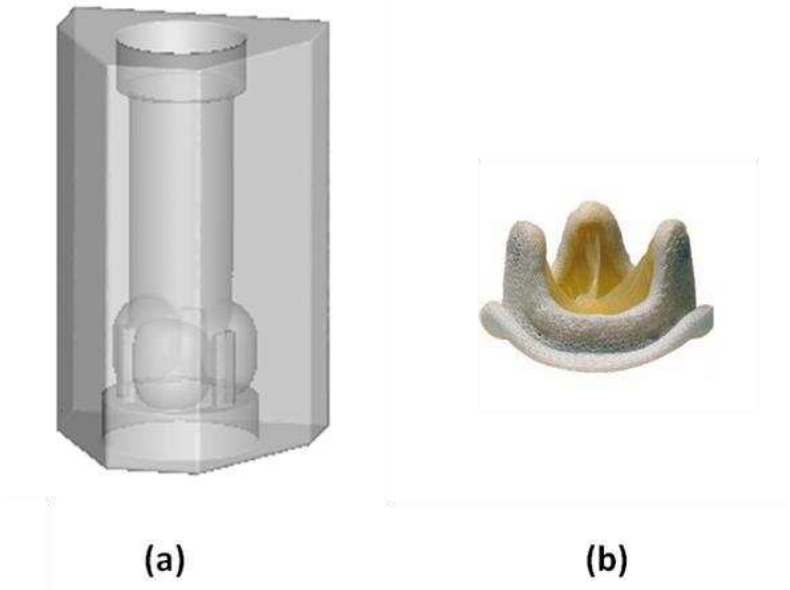

Figure 3.4: Model valve and sinus chamber
a) A 23mm Medtronic Hancock bioprosthesis was used as the model aortic valve, and
b) a custom-fabricated aortic valve chamber was used for PIV studies

bioprosthesis. This surgical valve was used as a model native aortic valve and is shown in Figure 3.4b. Due to the relatively small diameter of this valve, peak flow velocities were near 2 m/s in order to preserve an average cardiac output of 5 L/min.

3.2.4 Particle Image Velocimetry (PIV)

Two-dimensional in vitro particle image velocimetry (PIV) experiments were conducted to visualize fine-scale aortic sinus hemodynamics. For visualization purposes, the flow was seeded with PMMA-Rhodamine B seeding particles (microParticles GmbH, Berlin, Germany) with particle sizes ranging from 1 to 20 µm. These particles were illuminated by a laser sheet. The laser sheet was created with a Nd:YLF single-cavity diode-pumped solid-state, high-repetition-rate laser (Photonic Industries, Bohemia, NY) coupled with external spherical and cylindrical lenses. A high-speed CMOS camera (Photronix, Inc) was positioned for optimal viewing of flow within the sinus and coronary ostium. For the stented surgical valve, this meant a 60 degree angle to the laser sheet for limited obstruction from valve stent posts (see Figure 3.5). For the stentless valve, the camera was positioned at a 90 degree angle to the laser sheet since stent post obstruction of the sinus was not an issue.

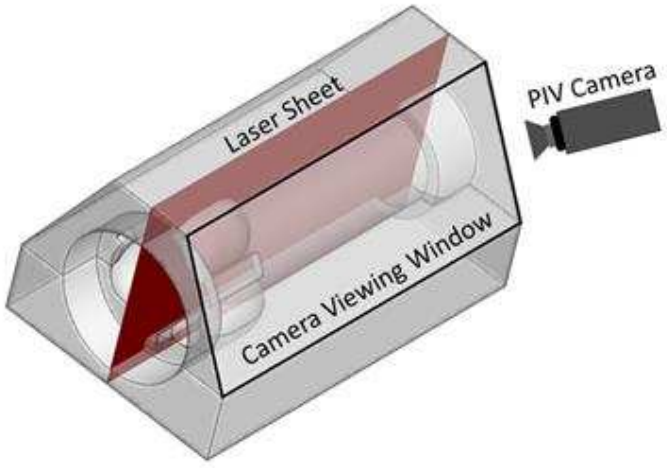

Figure 3.5: Sinus chamber PIV orientation
Orientation of valve chamber, laser sheet, and camera viewing window are depicted. The trapezoidal profile of the chamber allowed for optimal sinus viewing with limited obstruction from the valve stent posts

The commercial PIV software, DaVis (LaVision, Germany) was used for data acquisition and processing. Velocity vectors were calculated using an advanced PIV cross-correlation method. A 50% overlap multi-pass approach was employed in each case, with pixel interrogation window passes ranging from 64X64 to 16X16 pixels. No pre-processing was done, but post-processing was performed using adaptive median filtering. Effective spatial resolutions ranged from approximately 16 microns per pixel to around 80 microns per pixel and temporal resolutions ranged from 1000 Hz to 4000 Hz. Average particle seeding density was approximately 0.02 to 0.08 particles per pixel and the average particle displacement was around 4-12 pixels per frame, which maximized the accuracy of instantaneous velocity measurements to within 2% error.

Qualitative streak plots and quantitative vector plots were created for all cases. Vectors and vorticity contours were ensemble averaged across 5 repeat trials for each case. Additionally, the temporal complexity of turbulent coherent structures was examined by binning images across multiple frames. A bin size of 2.5 milliseconds was used to compare time-averaged flow patterns to instantaneous features within the sinus. Binned techniques are well known to provide coherent structure information at different time-scales [103].

3.2.5 Viewing Calibration

Due to differences in refractive index between air, acrylic, and the blood analog fluid, an image calibration method was developed to “undeform” raw images. In order to accomplish this, a 1mm-resolution grid was inserted into the valve chamber along the centerline of the viewing sinus. A picture was taken from outside the sinus chamber and grid intersection points were picked manually. This array of points was then modified by translating individual points to form a regularly-spaced matrix, consistent with the actual 1mm-resolution grid, and vectors were

computed from the deformed points to the "corrected" points. Bilinear interpolation was employed to compute the adjustment of any point within the sinus. Calibration was then applied to PIV velocity vectors in order to shift them back to real "world coordinates" from their deformed "camera coordinates". Figure 3.6 shows these image calibration steps.

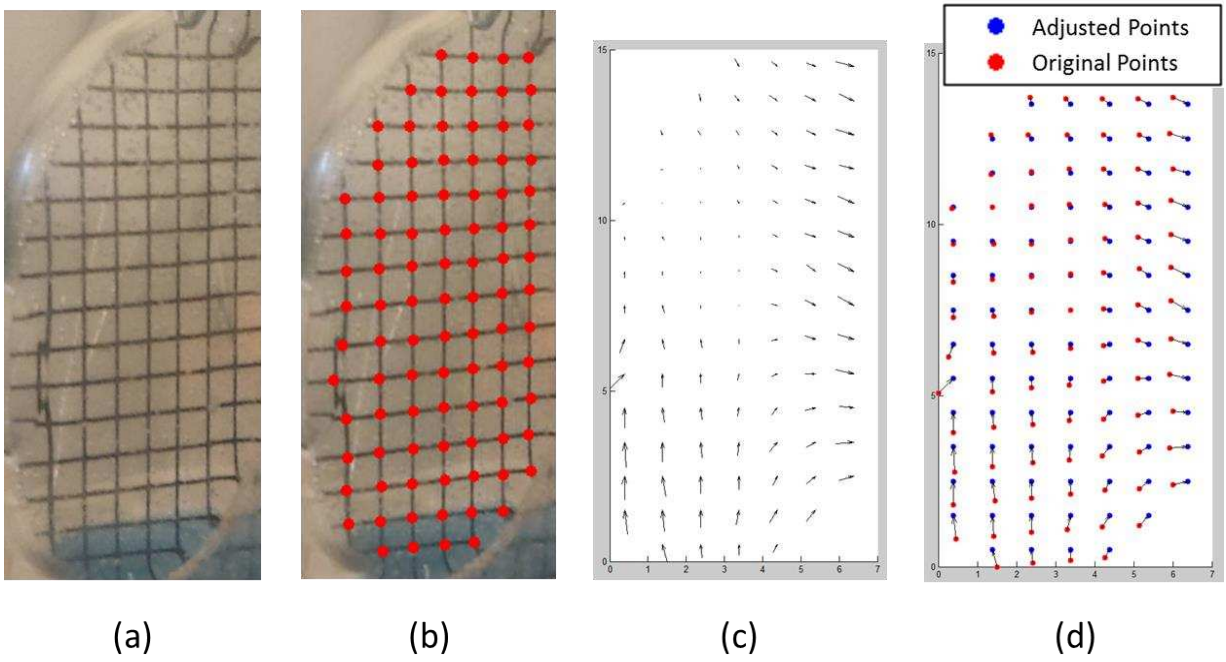

Figure 3.6: Depiction of image calibration steps
a) A 1mm resolution grid was inserted into the viewing sinus of the valve chamber, b) grid intersection points were manually picked, c) "adjustment" vectors were computed to correct for image distortion and d) original and "adjusted" points are superimposed to show effects of image distortion

3.2.6 Leaflet Kinematics Tracking

Leaflet tip motion was tracked manually throughout systole across multiple trials (repeats). Radial distance from the aorta centerline was recorded from raw PIV images and averaged across the repeated trials. Since the aortic axis was not visible in most PIV images, the sinus wall was used as a reference and radial distance was calculated based on known chamber dimensions.

3.3 Computational Methods

Computational models were developed to help validate experimental models as well as to give insight into additional flow information not provided by experiments. Both 2D and 3D computational models were created using ANSYS or SOLIDWORKS and meshed using ANSYS meshing software. Simulations were run in ANSYS Fluent. Geometric properties and flow boundary conditions were chosen based on typical physiological ranges for humans.

3.3.1 Two-Dimensional Setup

A baseline 2D aortic valve model was created using the commercial software ANSYS. Geometric parameters were chosen to represent average aortic valve anatomy. Valve motion was not modeled, therefore leaflet geometry was created in the open position and only systole was simulated. Automated, unstructured meshing in ANSYS was employed, which yielded a total grid size of approximately 190,000 cells. A time-varying inlet velocity boundary condition was imposed on the ventricular side of the valve and a constant pressure outlet boundary condition was prescribed approximately two diameters downstream of the valve. The inlet velocity was modeled by a half-sine wave yielding a 0.4s systolic duration. Peak aortic velocity was prescribed at approximately 1.3 m/s in order to yield a peak Reynolds number of around 7000. No turbulence modeling was used; instead detailed sinus flow features were fully resolved at length scales around 0.05 mm. Time step size was 0.001s and a 2^{nd} order upwind momentum solution scheme was used for the flow solver. The fluid properties were specified to match average values for those of blood (ρ = 1060 kg/m^3; μ = 0.0035 Pa-s). An image of the computational geometry is shown in Figure 3.7a.

3.3.2 Three-Dimensional Setup

A baseline three dimensional model was also created based on an average valve anatomy. The commercial software SOLIDWORKS was used to model the geometry (detailed geometry creation steps are detailed in Appendix II).

The same boundary conditions, fluid properties, and solution schemes were used as in the 2D models. Average grid size for the 3D cases was around 2.5 million cells per model, with grid resolution in the sinuses around 0.35 mm per cell. Overall geometry for the 3D case is shown in Figure 3.7b and detailed aspects of leaflet and sinus geometry are shown in Figure 3.7c and d.

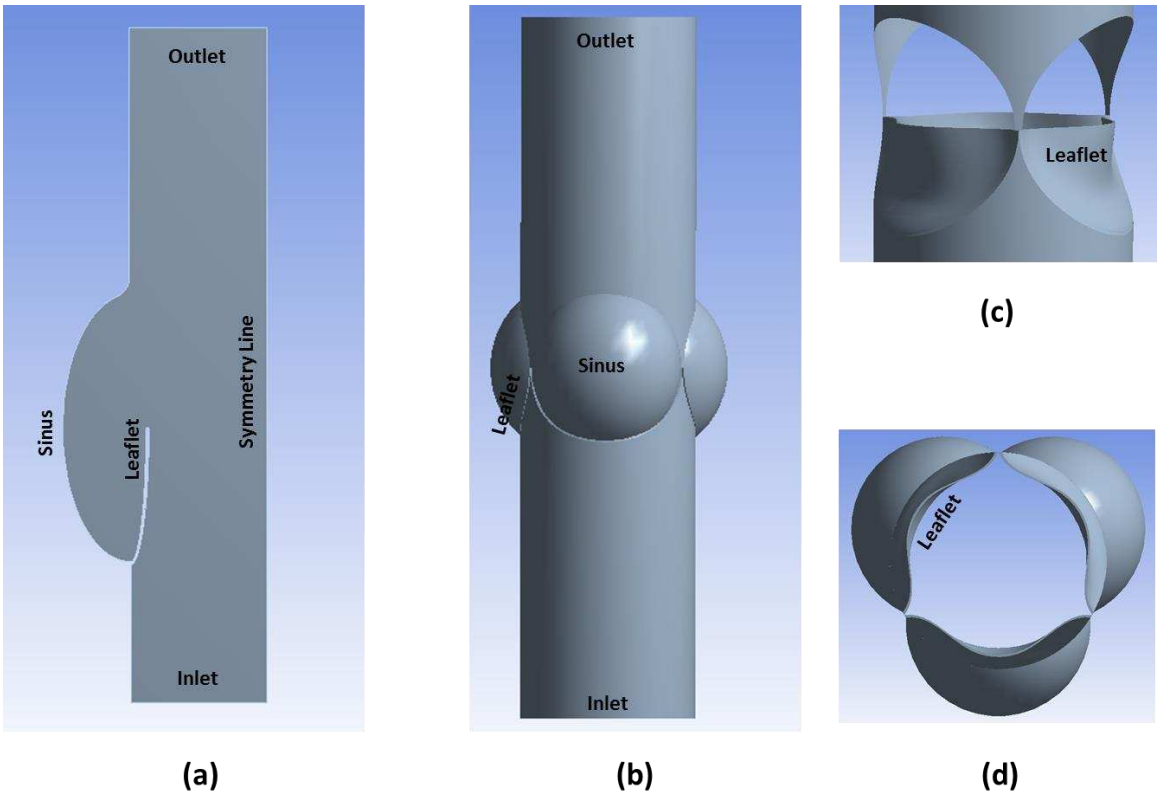

Figure 3.7: 2D and 3D computational models
Models were created using ANSYS and SOLIDWORKS software for 2D and 3D cases, respectively. Figure show a) overall 2D model, b) overall 3D model, c) leaflet view of 3D model (with sinuses hidden), and d) top view of 3D model showing leaflet configuration.

3.4 Baseline Study – Experimental

An initial test was conducted in order to visualize coherent vortex structures within one aortic sinus at fully resolved spatial and temporal scales. Results from this test were used to evaluate the feasibility of methodologies as well as to provide a baseline for comparison to future studies. Since the sinus region is of high spatio-temporal complexity, hemodynamics are best presented in both a qualitative and quantitative manner. Therefore, qualitative particle streak plots and quantitative vector plots were both created. A streak plot video is included in Figure 3.8 for one cardiac cycle. Qualitative descriptions are given first, based on these videos, followed by quantitative explanations of coherent structures based on time bin averaged velocity vectors and streamlines. Snapshots from qualitative videos are included to help clarify explanations of flow patterns that occur in the videos. Annotations included in these snapshots were manually superimposed (not PIV-calculated vectors) to point out flow structures that are generally more noticeable in the videos.

Figure 3.8: Baseline study streak plot video
A qualitative streak video was created by averaging raw PIV images across multiple frames at a time

In addition, five key time points during the cardiac cycle have been identified, based on observation of unique flow patterns, to help simplify the explanation of complex sinus hemodynamics. These time points are as follows (times in reference to start of leaflet opening): early systole (75-100 ms), mid systole (150-175 ms), late systole (275-300 ms), early diastole (400-425 ms), and mid/late diastole (600-700 ms). Total systolic duration was approximately 330 ms.

3.4.1 Qualitative Results

As seen in the qualitative streak plot videos, during early systole, after the valve has fully opened, a "starting" vortex sheds off the leaflet tip, and it migrates with the flow toward the downstream wall of the sinus. Interaction of this vortex with the sinus wall helps drive a recirculating flow in the downstream region of the sinus.

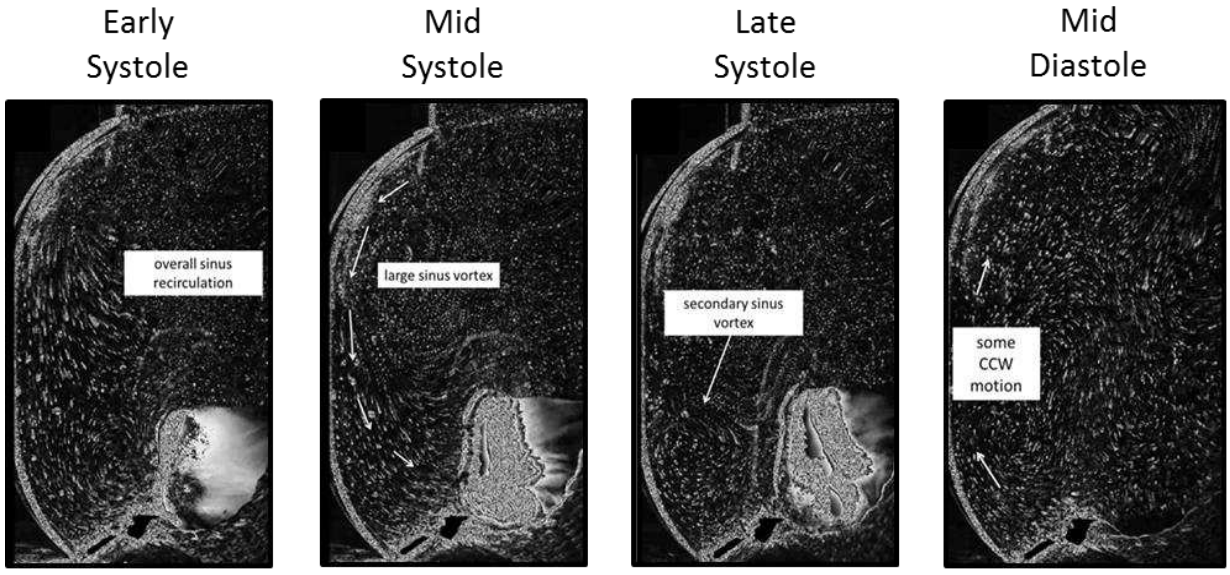

Figure 3.9: Baseline study streak plot snapshots
A) Overall recirculation begins early in the systolic phase, leading to B) a classical sinus vortex during mid systole. C) A secondary vortex can be seen in the base of the sinus by late systole, then D) some clockwise motion develops during diastole.

Toward mid systole, a more noticeable overall sinus vortex develops which appears to be driven by the high-velocity free stream flow. Some secondary flow becomes visible as the primary vortex causes some entrainment of quiescent fluid from the upstream end of the sinus. During late systole, the primary vortex reaches deeper into the upstream end of the sinus. As the leaflets begin to close, a secondary vortex of opposite rotation direction from the primary vortex forms due to accumulated momentum from previously mentioned entrainment.

As diastole begins, just after leaflet closure, a clockwise-rotating vortex continues to build near the base of the leaflet. This rotation eventually grows to fill the entire sinus during mid/late diastole. Near the end of diastole there is little fluid motion within the sinus.

3.4.2 Quantitative Results

Quantitative velocity vector plots were created by averaging 5 frames at a time (2.5 ms) across one cardiac cycle. This time-binning technique was employed to smooth out random turbulent fluctuations. Streamlines were also created for this bin size and are presented at the five key time steps mentioned above.

As seen in Figure 3.10, a sinus vortex with a peak velocity magnitude of about 0.2 m/s develops in the downstream end of the sinus during early systole, and this vortex migrates toward the center of the sinus during mid systole. One notable flow feature is the entrainment of quiescent fluid from the upstream portion of the sinus past the leaflet and into the freestream flow, a trend which is especially noticeable during mid and late systole. During diastole, a vortex develops near the leaflet with an opposite rotation direction to that of the main systolic sinus vortex, and this diastolic vortex expands to fill the sinus. This initial vortex quickly dissipates. Vectors at mid/late diastole depict a general clockwise rotation within the entire sinus, which dissipates as diastole progresses.

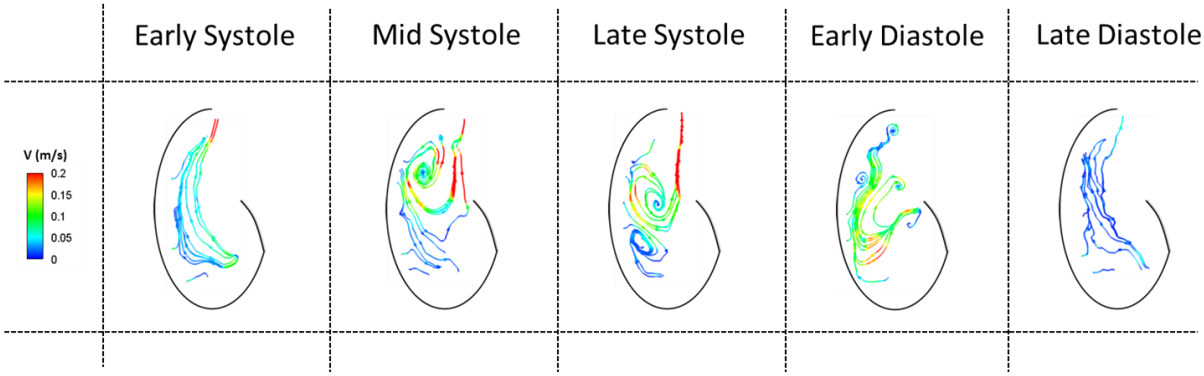

Figure 3.10: Baseline study streamlines
Streamlines, colored by velocity magnitude, are displayed within an outline of the sinus. Velocity fields used for streamline calculations were time bin averaged to smooth out instantaneous turbulent fluctuations.

3.4.3 Leaflet Kinematics

Leaflet kinematics were also monitored and Figure 3.11 shows a plot of radial leaflet position over time throughout systole. The leaflet opens rapidly to a maximum of approximately 10.5 mm from the aortic axis during early systole (~0.25s). This is followed by some slight migration of the valve back towards the aortic axis before rapid closure at the end of systole (~0.9 to 1s).

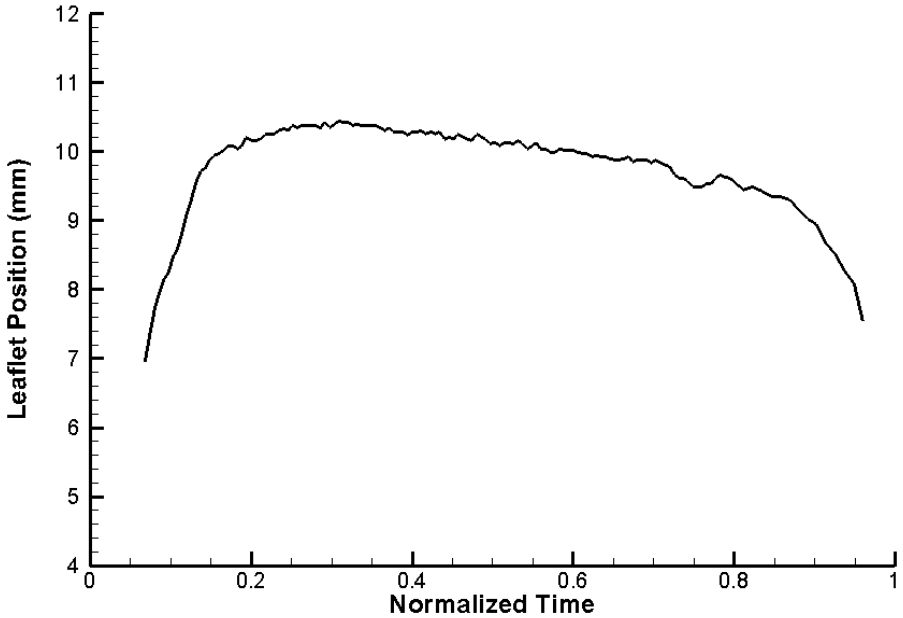

Figure 3.11: Baseline study leaflet kinematics
Leaflet tip position relative to the aortic axis was tracked manually and is plotted over systole

3.4.4 Discussion

Due to the relatively high spatio-temporal resolution of this baseline study, we were able to elucidate novel fine-scale hemodynamics within the aortic sinus. For example, flow is generally turbulent throughout systole so there are unsteady and aperiodic fluctuations within the sinus and also variability in the shape of the main sinus vortex. However, by binning across multiple frames we were able to replicate the smooth sinus vortex demonstrated in a number of previous studies (including 4D MRI) that lacked spatio-temporal resolution. Likewise, some patterns, such as the growth of the sinus vortex until late systole, are present in this study as well as earlier studies [104]. Still, there exist differences between our results and these previous studies, most notably the size of the main sinus vortex. In this study, the vortex does migrate to the center of the sinus, but it still does not encompass the entire sinus. In fact, a secondary vortex of opposite rotation direction forms in the upstream end of the sinus. One likely reason for this discrepancy is the difference in resolution between the present study and many others. For example, Kilner et al. [105] were only able to capture 16 frames across the entire cardiac cycle (40-60 ms intervals).

3.4.5 Limitations

There are a number of limitations associated with this modeling framework, as is expected with most experimental studies. One of these limitations is the inability of the flow loop to perfectly replicate pressure and flow conditions across the valve. For example, the role played by pressure wave reflections is very difficult to model in vitro. However, most pressure and flow trends are adequately reproduced with this setup. Another limitation is the use of a prosthetic valve within a rigid chamber. Because of this, neither material properties nor continuity between the valve leaflets and sinuses is preserved. Furthermore, while a compliance chamber was included downstream of the valve, aortic root compliance cannot be modeled with this setup due

to the rigid material used. These approximations are acceptable, though, since a bioprosthesis made from actual leaflet tissue was used and aortic root motion in vivo is quite small compared to leaflet motion. One other limitation is due to the PIV setup. Using this methodology, only a two-dimensional slice can be visualized rather than the entire flow field. While three-dimensional PIV techniques are in development, they are currently unable to fully resolve the spatial and temporal characteristics of sinus flow, so a two-dimensional method was deemed more appropriate.

3.5 Baseline Study – Computational

3.5.1 Results

Two-dimensional and three-dimensional simulations were run for idealized valve geometries. A planar slice was taken through the center of one sinus of the 3D model in order to compare results between the two cases. Out-of-plane vorticity contours were calculated and are presented in Figure 3.12 alongside 2D results at the same time points.

At early systole, vorticity contours for the two models are comparable. There is a sinus vortex, shed off of the leaflet tip, that is present in the downstream end of each respective sinus. However, by mid systole, flow patterns are drastically different between the 2D and 3D models. In the 2D model, the vorticity landscape remains relatively unchanged throughout systole, with a vortex present near the downstream end of the sinus. This vortex is no longer noticeable in the 3D case and vorticity contours show an unsteady sinus flow environment. There is still some positive vorticity in the sinus at mid systole, with a higher magnitude negative vorticity region present near the base of the sinus wall. By late systole, both positive and negative vorticity regions that were present in mid systole have moved farther toward the annulus, and there is little to no vorticity throughout the center of the sinus.

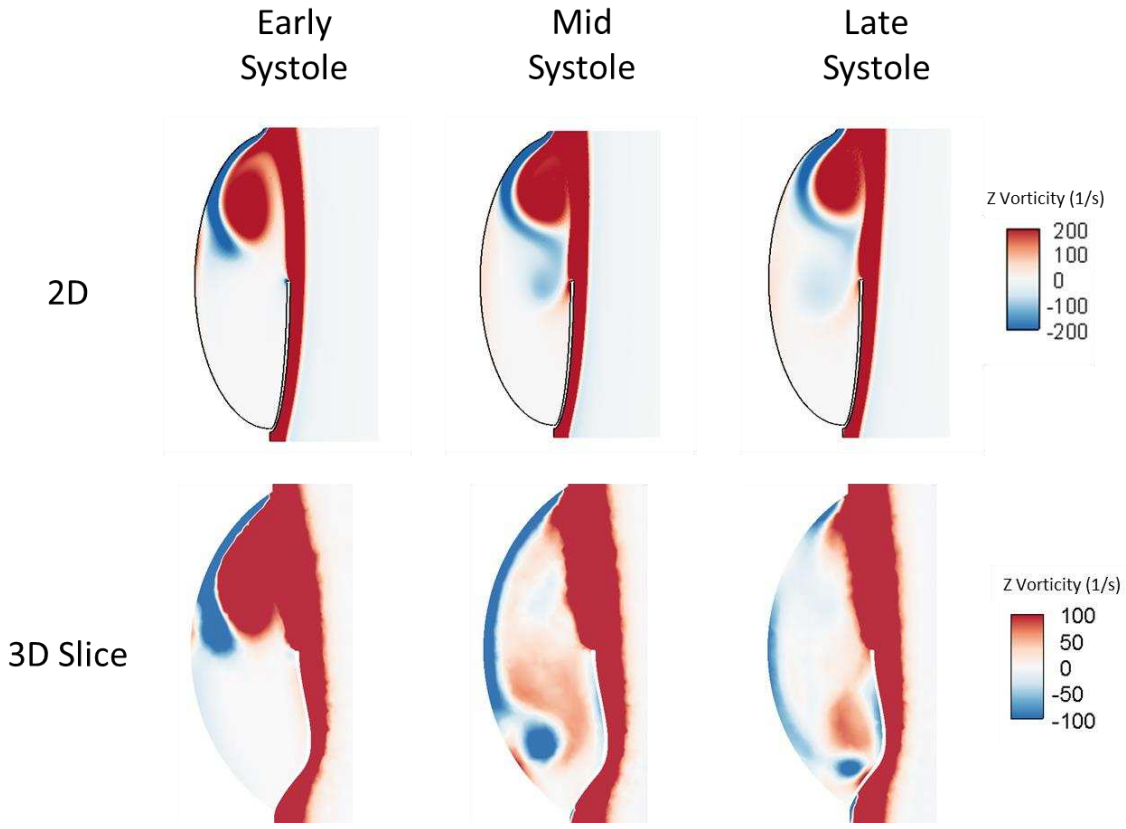

Figure 3.12: Baseline computational vorticity results
Sinus vorticity contours are presented for the a) two-dimensional model and b) at a slice through the sinus center plane of the three-dimensional model

Since there is significant out-of-plane fluid motion that is not captured by a slice of the 3D model, additional analysis was conducted to visualize these flow patterns. Figure 3.13 shows streamlines within one sinus at different time points as well as at different viewing angles throughout systole. These streamlines were calculated from a rake of points along the aortic side of the leaflet free edge.

During early systole, streamlines depict a laminar flow environment, with a smooth recirculation region in the sinus. This region spans an area from the sinotubular junction to the leaflet free edge. Fluid velocities range from over 0.5 m/s as flow enters the sinus to almost zero near the aortic side of the leaflet. There is some 3D motion closer to the commissures than the center of

the sinus. Streamlines here follow a circumferential, as well as radial, path. By mid systole, flow appears much more turbulent as streamlines are more random and unpredictable.

One apparent flow pattern that can be seen from the normal sinus view is the presence of two vortices in the sinus. The oblique view shows that these vortices form at a slight angle compared to the normal viewing orientation. Examination of these streamlines from a side view demonstrates that this angle is less than ninety degrees, since no discernible flow patterns can be seen from this view. Overall, a pattern of fluid movement seems to start at the sinus midplane near the sinotubular junction, where streamlines then stretch downward along the sinus wall to the annulus. At this point, streamlines diverge and run parallel to the line of leaflet

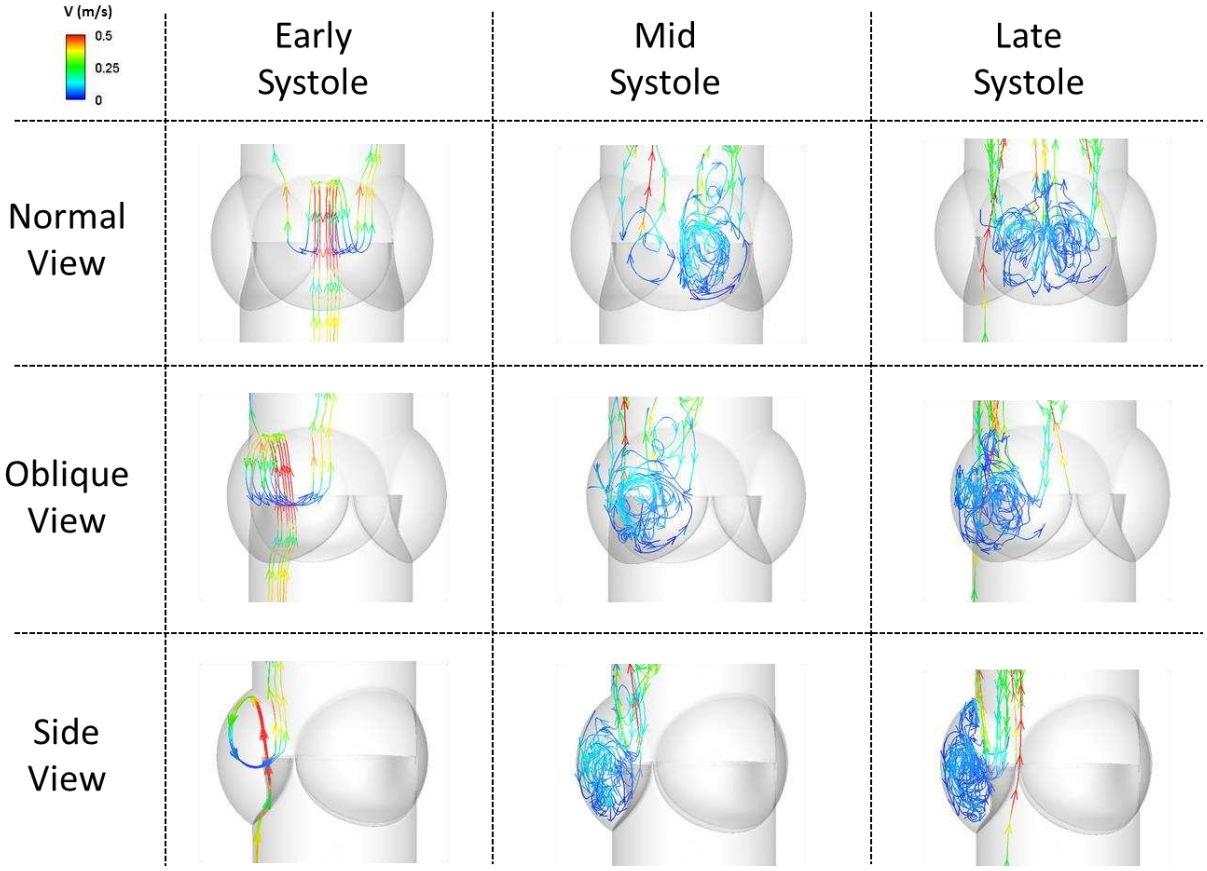

Figure 3.13: Baseline computational streamline results
Streamlines, colored by velocity magnitude, are presented at different systolic time points and at different viewing angles within one sinus.

attachment toward one of the two commissures. From here, fluid velocity vectors then point back toward the starting point on the sinus wall near the sinotubular junction. By late systole, flow is still turbulent and flow patterns are hard to recognize. However, there is still noticeable separation of flow where the sinus midplane intersects the annulus, and some symmetry exists across this plane.

3.5.2 Discussion

Two dimensional results show a sinus vortex localized near the sinotubular junction and a weaker, secondary vortex closer to the base of the valve. The location and strength of the main vortex appears to be governed by the interaction between the shear layer from the leaflet free edge and the curvature of the sinus wall near the sinotubular junction. Therefore, this sinus wall curvature could have an impact on vortex dynamics. The secondary vortex is likely formed due to viscous interaction between the main vortex and quiescent fluid in the base of the sinus, which is a common flow pattern seen in the experimental study.

Significant differences exist between the 2D and 3D cases, which is expected due to the geometric nature of the valve. This geometry is not well-represented in a 2D manner. Initially, vorticity dynamics are similar between the two cases, with a sinus vortex present near the sinotubular junction. However, it is likely the interaction between the fluid and sinus wall near this junction that causes a deviation in flow patterns between the 2D and 3D cases. In the 2D model, flow can only be redirected in essentially one direction once it hits the sinus wall – downward into the sinus. This direction is approximately parallel to the axis of the aorta. In the 3D case, flow is still redirected down into the sinus due to curvature of the sinus wall. However, the fluid can move circumferentially as well due to the 3D shape of the sinus. This freedom of movement in the circumferential direction appears to distribute vorticity throughout the sinus,

thus detracting from the sinus mid-plane vorticity (as shown in Figure 3.12). One flow pattern that is common to both simulation cases as well as to the experimental study is the presence of a secondary vortex near the base of the sinus. This appears to be caused by viscous interaction with the main vorticity in each dimensional case. Furthermore, its location in the 3D case, which is much closer to the base of the sinus, matches experimental results better than the 2D case.

While lower vorticity magnitudes were calculated from the 3D slice than in the 2D case, it appears that the sinus shape provides a means for distributing flow throughout this region, and therefore prevents stagnation zones from forming. This is beneficial from a clinical standpoint since stagnation can often lead to thrombosis and low leaflet wall shear stress (due to reduced velocity) is strongly tied to calcification.

Three-dimensional streamlines support the assertion of circumferential fluid movement in the sinus during mid and late systole. This motion seems to be determined by the shape of the sinus wall, thus providing further support for the notion that aortic root geometry is a key regulator of sinus hemodynamics and therefore valve health.

3.5.3 Grid and Time Step Sensitivity

In order to verify the suitability of the mesh and time step sizes, spatial and temporal scales were refined and then simulations were run for comparison. Four additional simulations were run in total: spatially refined 2D, temporally refined 2D, spatially refined 3D, and temporally refined 3D models.

For the 2D case, the original mesh of approximately 190,000 cells was refined to approximately 760,000 cells. This changed the resolution in the sinus from 0.05 mm/cell to 0.025 mm/cell.

Additionally, the original time step size of 0.001 s was adjusted to 0.0001 s and a simulation was run on the baseline mesh. Vorticity results for spatially and temporally refined 2D models are shown alongside the baseline 2D model in Figure 3.14. Although vorticity magnitudes are slightly different between cases, flow patterns are not significantly different so the baseline mesh and time step size were deemed adequate for the purposes of this study.

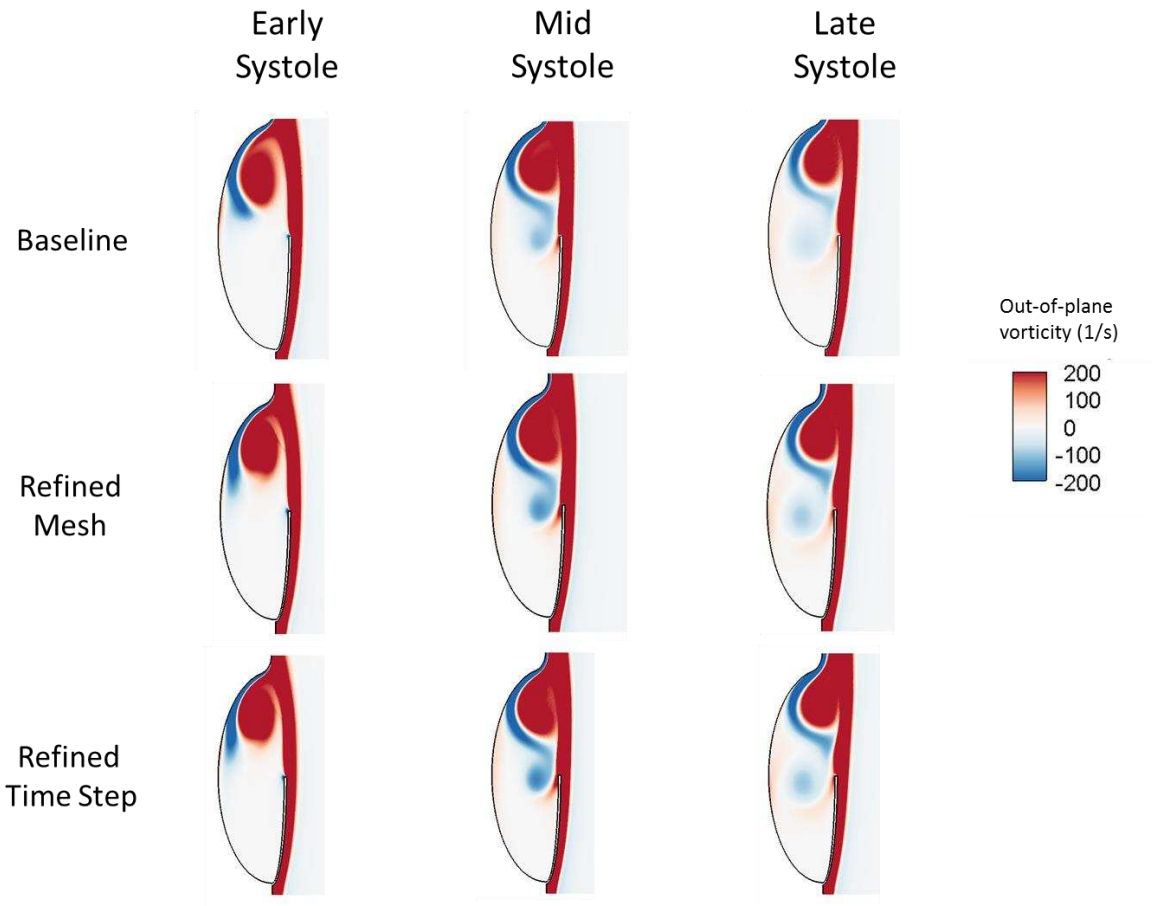

Figure 3.14: 2D grid and time step sensitivity
The baseline model of ~190,000 cells that was run with a time step size of 0.001s was compared to a spatially refined model of ~760,000 cells and also to the same mesh with a refined time step of 0.0001s.

For the 3D case, the original mesh of approximately 2.5 million cells was refined to approximately 4.6 million cells. This changed the resolution in the sinus from 0.35 mm/cell to 0.25 mm/cell. Additionally, the original time step size of 0.001 s was adjusted to 0.0001 s and a

simulation was run on the baseline mesh. Vorticity results along the center plane of one sinus are shown for spatially and temporally refined 3D models alongside the baseline 3D model in Figure 3.15. Similar to the 3D case, vorticity magnitude does change as the grid and time step are refined. However, the purpose of these simulations is to qualitatively compare to and enhance experimental findings. Therefore, since flow patterns are common between baseline and refined models, the baseline case was used.

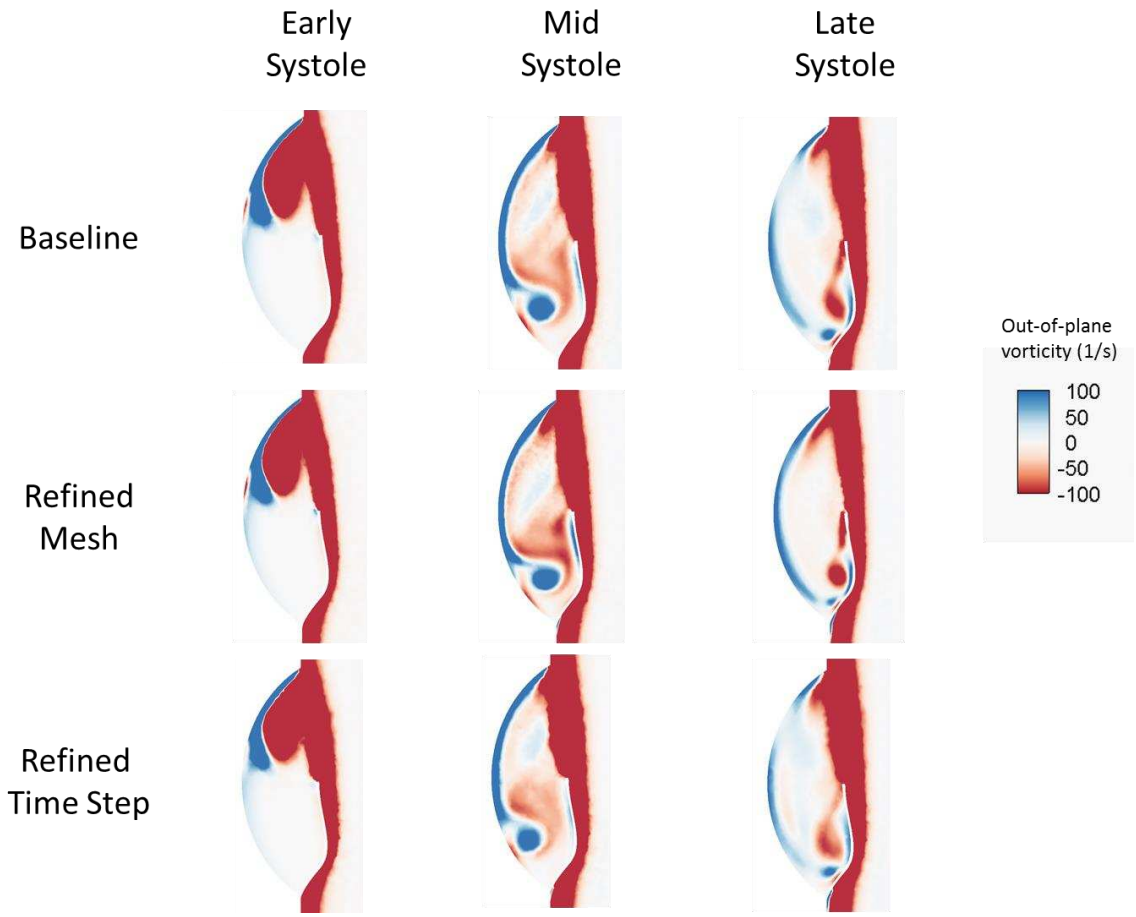

Figure 3.15: 3D grid and time step sensitivity
The baseline model of ~2.4 million cells that was run with a time step size of 0.001s was compared to a spatially refined model of ~4.6 million cells and also to the same mesh with a refined time step of 0.0001s.

3.5.4 Limitations

Two dimensional simulations are inherently limited by spatial dimension. Additionally, both 2D and 3D cases utilized rigid leaflets. Therefore, the flow physics during and resulting from leaflet opening and closing are not simulated, nor is the diastolic phase of the cardiac cycle.

3.6 Chapter Summary

Detailed methodologies have been developed to study aortic sinus hemodynamics in vitro. A tunable flow loop is capable of replicating realistic pressure and flow conditions across a model valve. Hemodynamics visualization is accomplished through the use of a clear sinus chamber and a PIV protocol. Additionally, viewing calibration has been conducted to ensure minimal distortion of PIV images due to refraction from the valve chamber, and this calibration also provides a means to correct raw images that may be distorted due to such refraction effects. A baseline study has been conducted and shows the feasibility of these methods. Results from this study confirm the existence of a sinus vortex while also capturing more detailed flow patterns. In particular, an unsteady vortex is seen, which can be time-averaged to yield a more steady flow feature. There is also some secondary recirculation near the base of the sinus that is of opposite rotation direction to the main vortex.

In addition to experimental methods, computational methods have also been developed to simulate aortic valve hemodynamics in both a two- and three-dimensional manner. Valve models were created based on average geometric parameters and simulations were run using the commercial software ANSYS Fluent. Two dimensional simulations show a sinus vortex that is localized in the downstream portion of the sinus as well as a weaker secondary vortex closer to the valve annulus. The strength and location of these structures appear to be strongly tied to valve geometry. Results from 3D simulations show much more complex sinus hemodynamics.

There are two main vortices in this case that are symmetric about the sinus midplane, and these vortices also drive some secondary recirculation in the base of the sinus.

Both the experimental and computational methods developed possess their own limitations. However, this tandem experimental-computational approach helps overcome many of these limitations. This is because some of the key experimental limitations are not present in the computational studies, and vice versa, so much more information is gained from this combination approach than from either method on its own.

4. SPECIFIC AIM 2

Characterize the differences in native valve flow patterns that occur due to patient and sinus variability

4.1 Chapter Introduction

The goal of Specific Aim 2 was to determine the effects of different valve conditions on sinus hemodynamics. These conditions are determined by different anatomical and physiological parameters – such as sinus dimensions, heart rate, and aortic flow waveform shape as well as coronary flow aspects such as coronary vs non-coronary sinuses, coronary ostia locations, and coronary flow strengths. Both experimental and computational methods, developed in Specific Aim 1, were employed to test these various valve conditions. Qualitative and quantitative analyses of sinus hemodynamics are presented here. This work has led to two conference publications [101, 106] and one journal publication [107].

4.2 Experimental Methods

4.2.1 Valve Chamber

Another valve chamber was created to fit the prosthetic model valve and also to provide for modeling coronary flow (see Figure 4.1). The design of the second chamber was refined to fit the particular valve – a 23 mm Medtronic Hancock II porcine bioprosthesis – that was used as a model native valve. Specifically, grooves were machined into the walls of this chamber so that the stent frame was flush mounted and did not protrude into the flow domain. Sinus dimensions for this chamber included an aortic diameter of 19 mm, a sinus height of 17.6 mm, and a sinus radius of 13.5 mm. Additionally, a 4 mm diameter hole was drilled through the chamber wall and into one sinus in order to model coronary flow. This hole intersected the sinus (i.e. the ostium) at the midpoint between the annulus and sinotubular junction, a location that was chosen based on a previous clinical study [108].

Figure 4.1: Flush-mounted sinus chamber
An additional custom-fabricated valve chamber was used for PIV studies. This chamber was fabricated for flush-mounting of the model native valve and also includes a mock coronary artery

4.2.2 Coronary Flow Loop Branch

In order to model coronary flow, an additional branch was added to the piston pump flow loop (see Figure 4.2). As shown in the schematic diagram, this branch attaches to one aortic sinus and leads back to the fluid reservoir. It contains a compliance chamber and resistance valve, which serve the same purpose as the aortic compliance and resistance on the main branch of the loop. The other component of this coronary branch is a "constriction chamber" (see Figure 4.3) used to add time-varying resistance to the flow. This chamber operates on the same principle as the bladder pump used to drive the flow loop described in Specific Aim 1 – a flexible conduit is passed through a rigid chamber that can be pressurized and depressurized at controlled time intervals. In this way, a physiological coronary waveform can be replicated by adding resistance to the flow during systole, which happens in vivo due to constriction of the vessels by myocardial contraction.

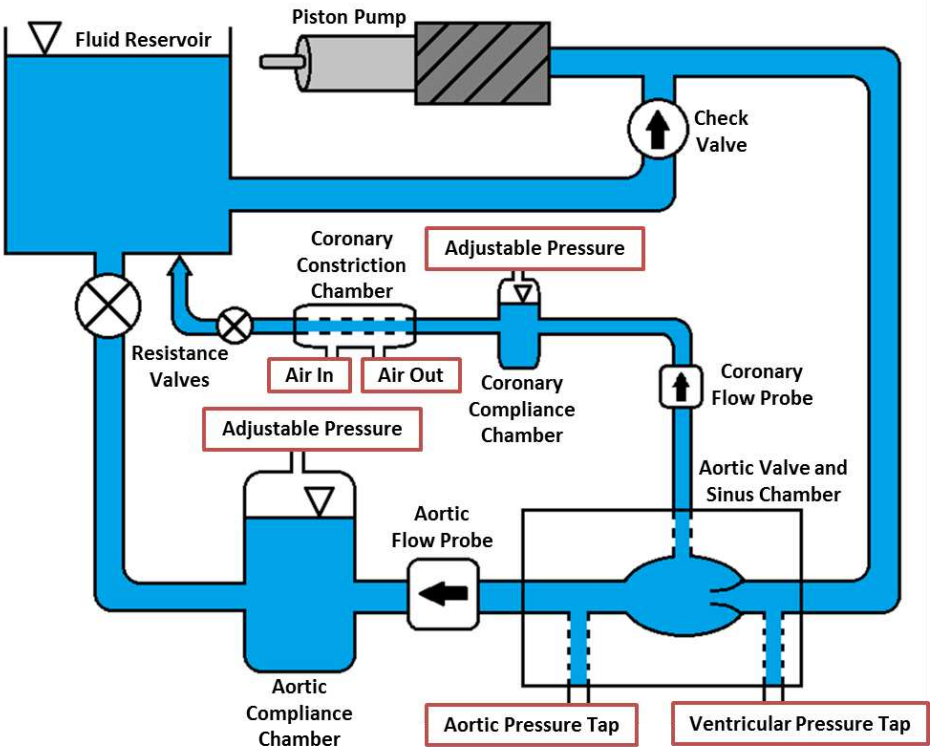

Figure 4.2: Flow loop schematic with coronary branch
An additional branch was added to the piston pump flow loop to model coronary flow. This branch included compliance and resistance as well as a constriction chamber to add time-varying resistance to the flow.

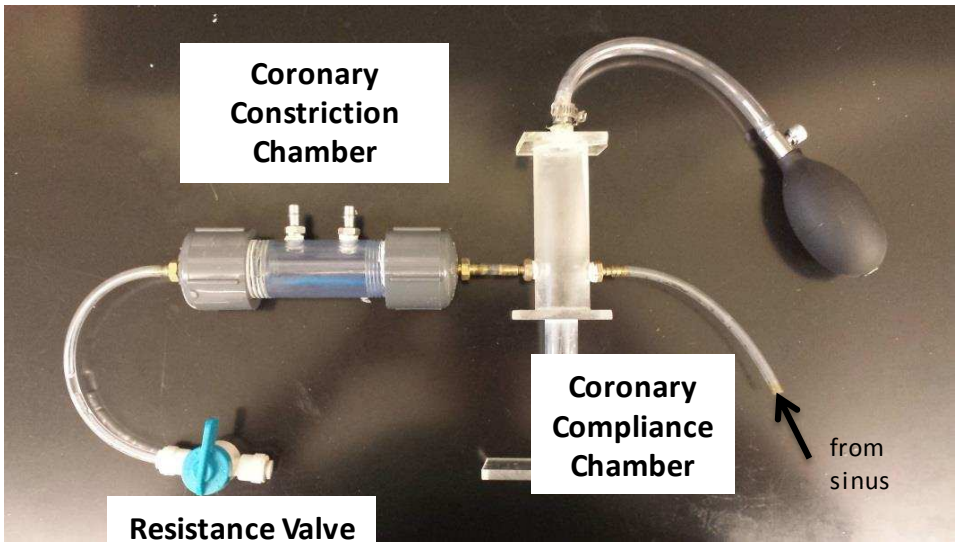

Figure 4.3: Image of experimental coronary flow branch
This chamber was used to impose time-varying resistance on the coronary flow branch. In this way, flow resistance due to myocardial contraction was simulated.

4.2.3 Flow Parameters

Both normal and elevated heart rates were tested under physiological blood pressure (HR ~60/120 bpm; BP ~120/80 mmHg). Systolic time fraction was set to the nominal physiological values of 1/3 and 1/2 for the 60 bpm and 120bpm cases, respectively. Due to differences in heart rates, there was a discrepancy in Reynolds and Womersley numbers for these two trials. Table 4-1 shows these parameters for each case of fluid type and heart rate condition.

Table 4-1: Heart rate study Reynolds and Womersley numbers
Peak Reynolds number (based on bulk velocity and aorta diameter) and Womersley number for each heart rate case

	Peak Reynolds number	**Womersley number**
60bpm	7,915	~16
120bpm	3,518	~23

Pressure and flow rate data for the two cases described in Table 4-1 are given in Figure 4.4a and b. Aortic and coronary flow rates, using a blood viscosity-matching glycerin solution at normal heart rate, are shown in Figure 4.4c.

In addition to heart rate, another physiological parameter studied was the shape of the aortic flow waveform. Three waveforms were generated, each with a different peak flow time. An early peak flow time case was created by imposing a rapid acceleration of the piston pump coupled with a gradual deceleration. Conversely, a gradual piston acceleration and rapid deceleration created a late peak in the aortic flow waveform. A third case was also studied with equal rates of piston acceleration and deceleration. These three different flow waveforms can be seen in Figure 4.4d.

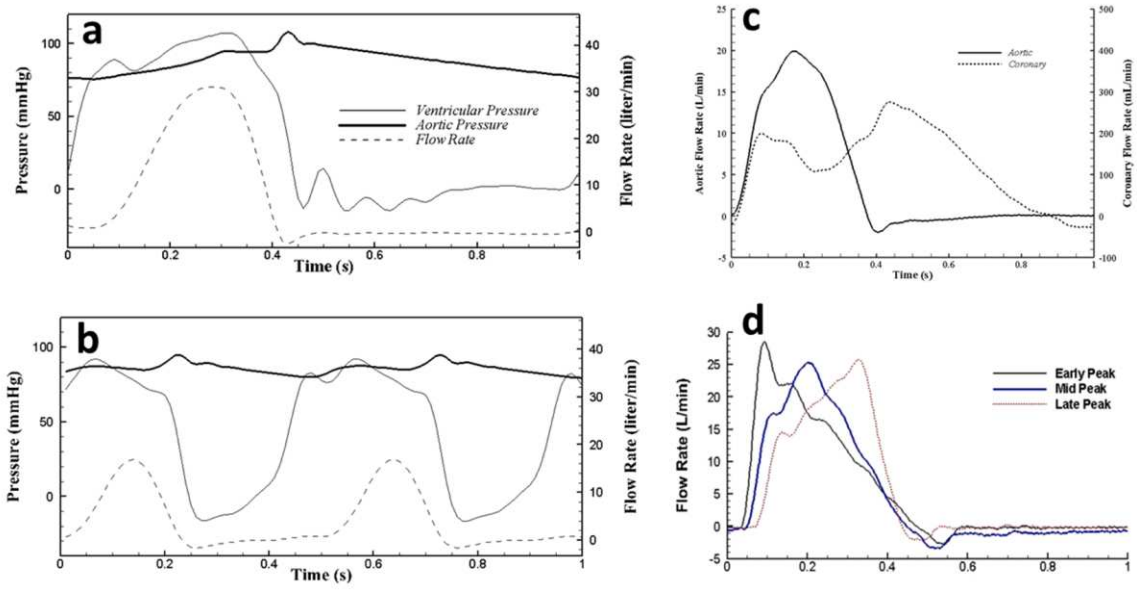

Figure 4.4: Experimental pressure and flow waveforms for parametric studies
Flow loop generated hemodynamic data is given for a) 60 and b) 120 bpm heart rate studies as well as c) coronary flow study and d) aortic flow waveform shape study

4.2.4 PIV Setup

A similar PIV protocol was followed as in Specific Aim 1. When the coronary valve chamber was used, the laser sheet was positioned so that it passed through the center of the ostium (which was also the center of the sinus). Due to the presence of the ostium, however, the laser sheet was not able to illuminate the entire sinus without casting a shadow from the coronary tube fitting. This shadow covers only a small amount of the base of the sinus, so results can still be viewed within the main area of interest.

4.3 Computational Methods

A number of computational simulations were conducted to examine the effects of different anatomic and physiologic parameters on sinus hemodynamics. Some of these parameters were also tested experimentally while others were only studied computationally. The parameters tested include sinus radius, presence of coronary flow, coronary ostia location, and

coronary flow rate. Results for each case are presented at three discrete time points throughout systole – early (100ms), mid (200ms), and late (300ms) systole. Total systolic duration was 400ms.

Two- and three-dimensional baseline models were first developed to match experimental parameters (Specific Aim 1), and then additional models were created to test the effects of different anatomical and physiological valve conditions (Figure 4.5). For the two dimensional models, sinus dimensions were initially created based on the experimental valve chamber and

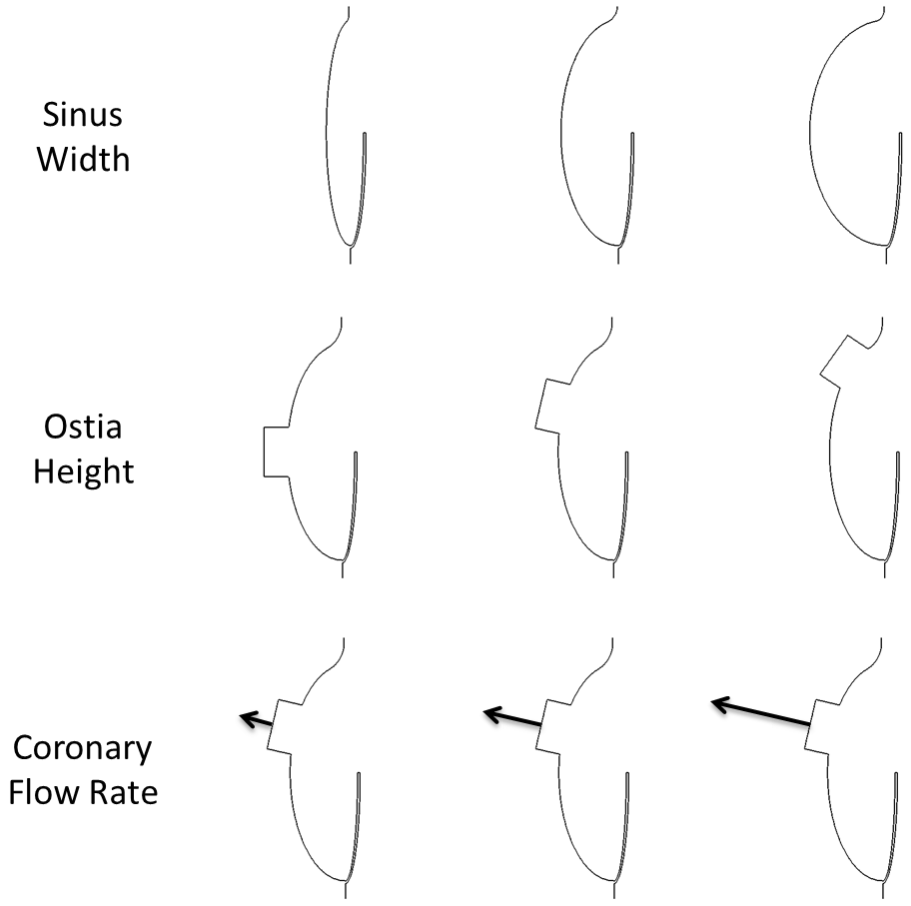

Figure 4.5: 2D computational sinus models
Parameters tested include sinus width (narrow, average, and wide), ostia height (low, average, and high), and coronary flow rate (weak, average, and strong)

then adjusted to study hemodynamics for different sinus sizes. A coronary model was also developed with geometric parameters based on a previous in vivo imaging study [26]. Specifically, a 4mm coronary artery was added to the baseline model approximately 3.5 mm above the center of the sinus. This location was adjusted to create two other models with higher and lower ostia positions representative of upper and lower physiological bounds. Additionally, the magnitude of coronary flow rate was also manipulated to cover a range of realistic scenarios. Initially, a time-varying velocity boundary condition was prescribed at the coronary outlet based on experimental data, which was generated from a flow loop that was tuned to replicate an in vivo coronary flow waveform [109-111]. This was then modified to investigate different coronary flow rates by multiplying by a constant to adjust the magnitude, but not the shape, of the waveform.

One additional 3D model was also created to compare to the baseline study results. This model included a 4 mm diameter coronary artery, which was placed at the midpoint of the sinus in order to match the location of the experimental ostium. The baseline and coronary 3D valve models are shown in Figure 4.6.

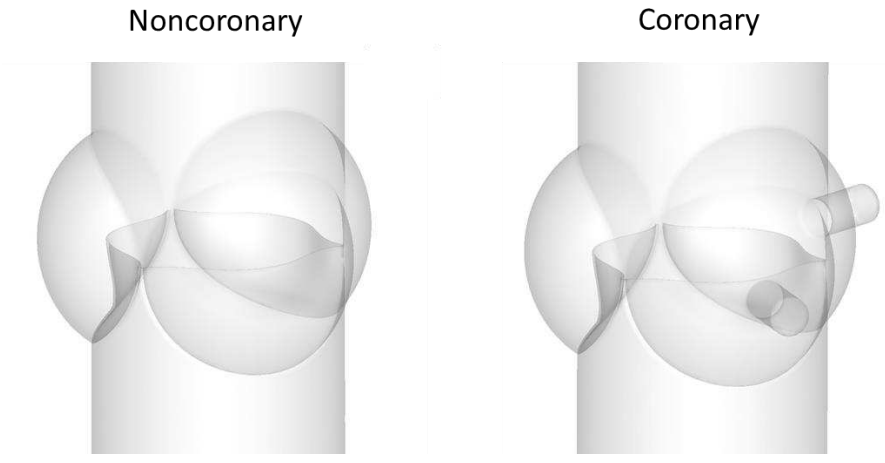

Figure 4.6: 3D non-coronary and coronary computational models
Baseline (noncoronary) and coronary 3D CFD geometric models are shown

4.4 Heart Rate Effects – Experimental

The first parameter investigated for its effects on sinus hemodynamics was heart rate. An elevated heart rate of 120 bpm, which is representative of tachycardia, was imposed on the flow loop and the same methods as in the baseline study were employed to capture sinus flow patterns. Due to the shortened time duration for a cardiac cycle in this case, results are presented at the following time points: early systole (30-50 ms), mid systole (75-95 ms), late systole (120-140 ms), early diastole (190-210 ms), mid/late diastole (300-350 ms).

4.4.1 Qualitative Results

Qualitative streak plot video for 120bpm case, compared against 60bpm case, is shown in Figure 4.7. Note that both cases are normalized based on time so that one cardiac cycle is elapsed in the same amount of time for each heart rate. Additionally, snapshots from these

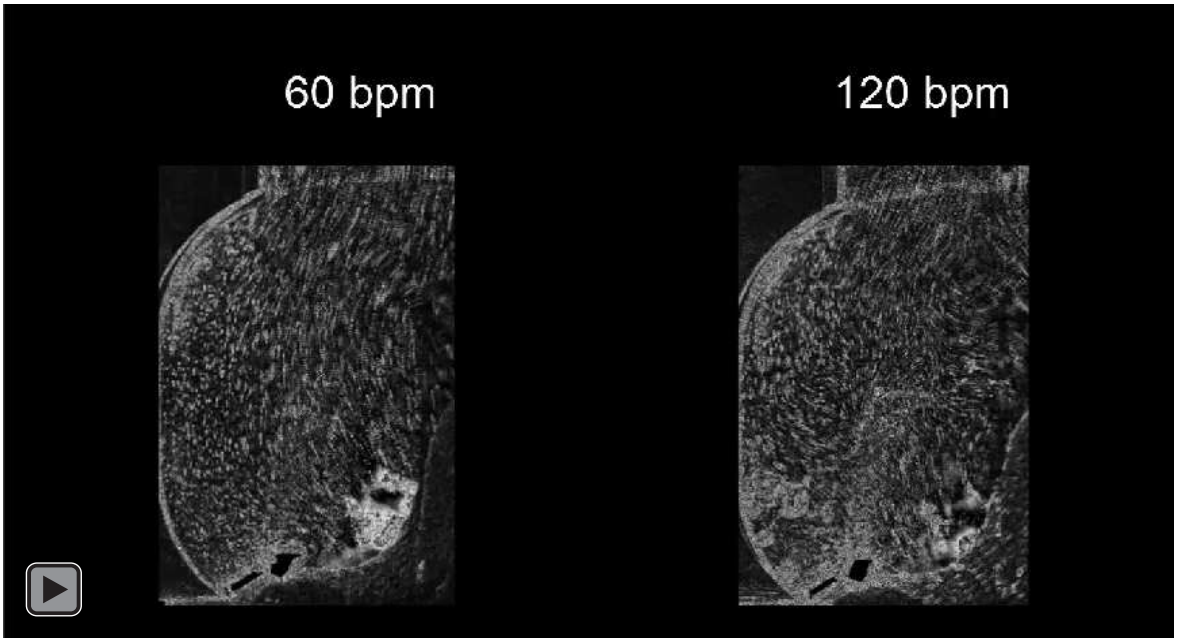

Figure 4.7: Heart rate study streak plot video
Qualitative videos show particle streak paths within the sinus for both normal (60 bpm) and elevated (120 bpm) heart rates. Time is normalized to show one cardiac cycle over the same duration for each case.

videos are shown in Figure 4.8. At early systole, most flow patterns are similar in both the 60 and 120 bpm cases. By mid systole, subtle differences between normal and elevated heart rates start to become evident. The primary vortex, present in both cases, is slightly smaller in

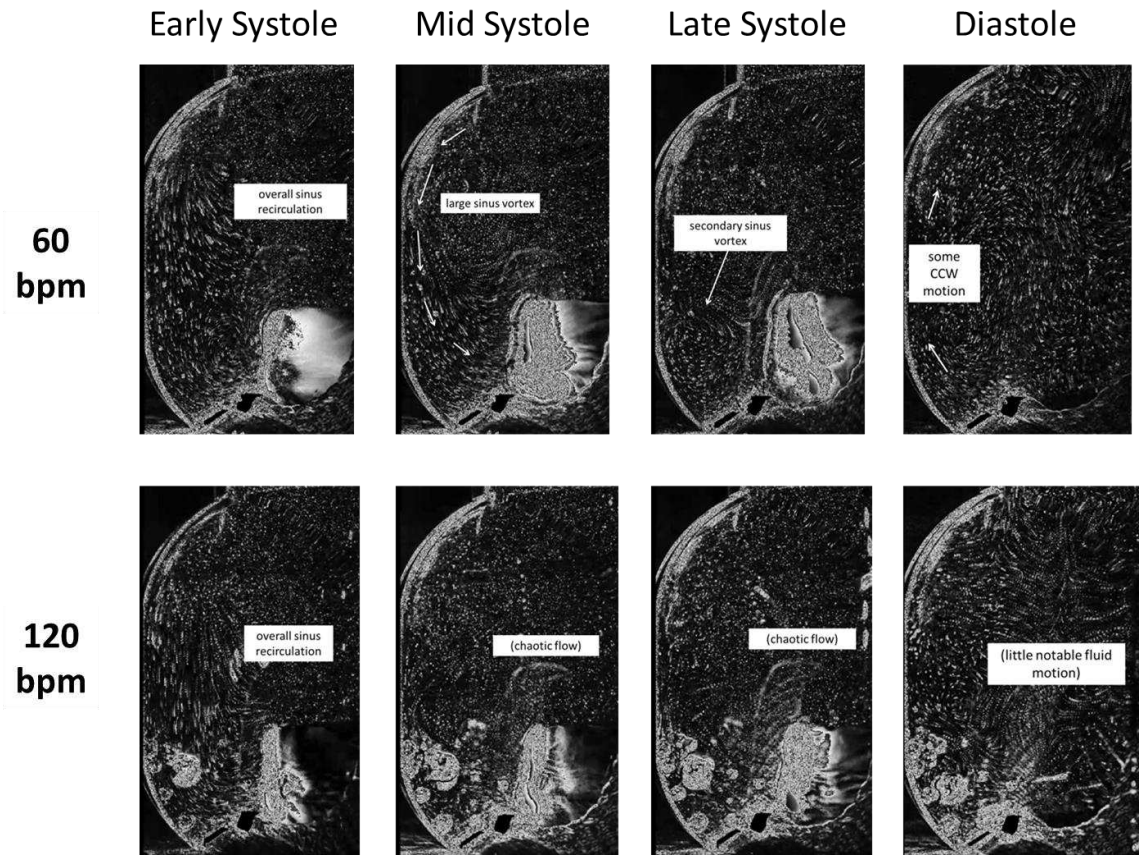

Figure 4.8: Heart rate study particle streak plot snapshots
Instantaneous snapshots were taken from streak plot videos for both the normal (60 bpm) and elevated heart rate (120 bpm) cases. Images contain annotated arrows and text to help describe flow patterns.

the 120 bpm case and also appears to be positioned more near the downstream end of the sinus, although a much more chaotic sinus environment at elevated heart rate makes determination of coherent structures difficult. During late systole, the primary vortex reaches deeper into the upstream end of the sinus, an event much more noticeable in the normal heart rate case. This may be due to the limited time duration that the leaflets are open when the heart rate is elevated. Again, due to the limited time duration and also as a byproduct of lower flow

rate, overall fluid velocities within the sinus appear lower in the 120 bpm case during early diastole and very little flow is present during later diastolic time points.

4.4.2 Quantitative Results

Quantitative results were also generated and analyzed for the elevated heart rate case. Figure 4.9 shows the development of a slightly more turbulent sinus vortex for an elevated heart rate. This vortex, as in the regular heart rate case, forms near the downstream end of the sinus and migrates upstream to the middle of the sinus as systole progresses. Velocity magnitudes within the sinus are similar at a maximum of about 0.2 m/s. One difference from the 60bpm case is that there is no secondary circulation near the base of the leaflet during systole. Diastolic flow patterns initially show some clockwise movement, which is quickly dissipated so that very little fluid motion is present at the end of diastole.

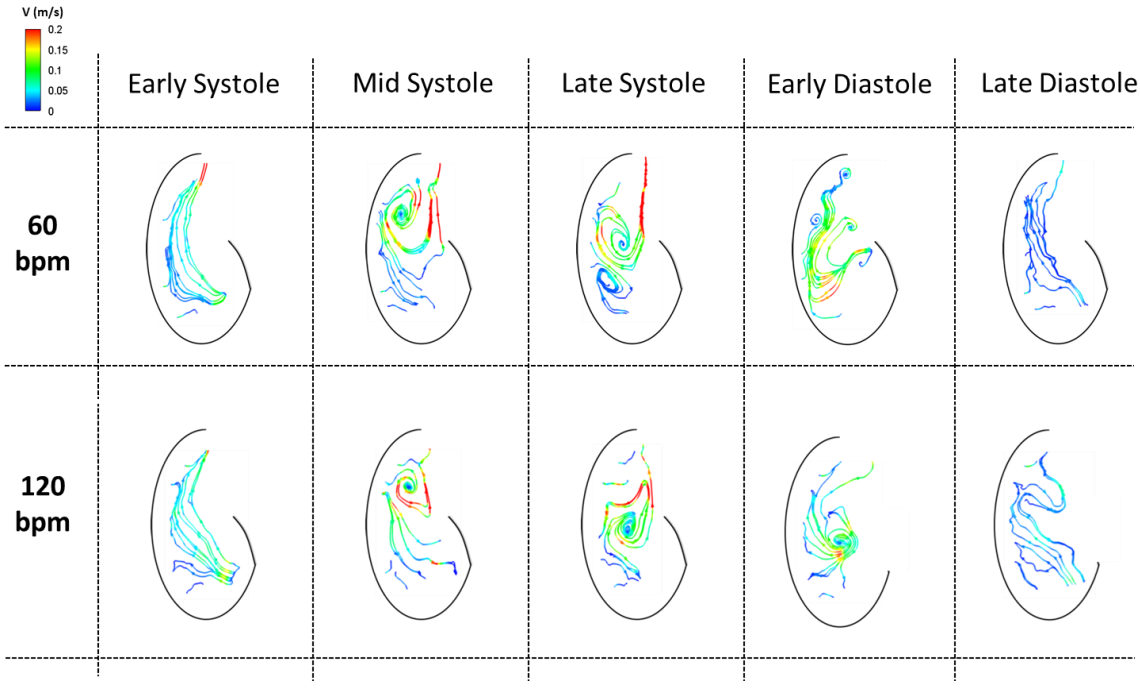

Figure 4.9: Heart rate study streamlines
Streamlines, colored by velocity magnitude, are presented at different time points within one sinus for the normal (60 bpm) and elevated (120 bpm) heart rate cases.

4.4.3 Leaflet Kinematics

Plots of leaflet tip position vs normalized systolic time are shown for both normal and elevated heart rates in Figure 4.10. This figure shows a slightly fuller valve opening for the elevated heart rate case, with the leaflet tip reaching a radial position of nearly 11 mm as opposed to just over 10 mm in the normal heart rate condition. There is also a longer opening time for the 120 bpm heart rate, shown as the time taken to reach maximum radial leaflet position in the figure.

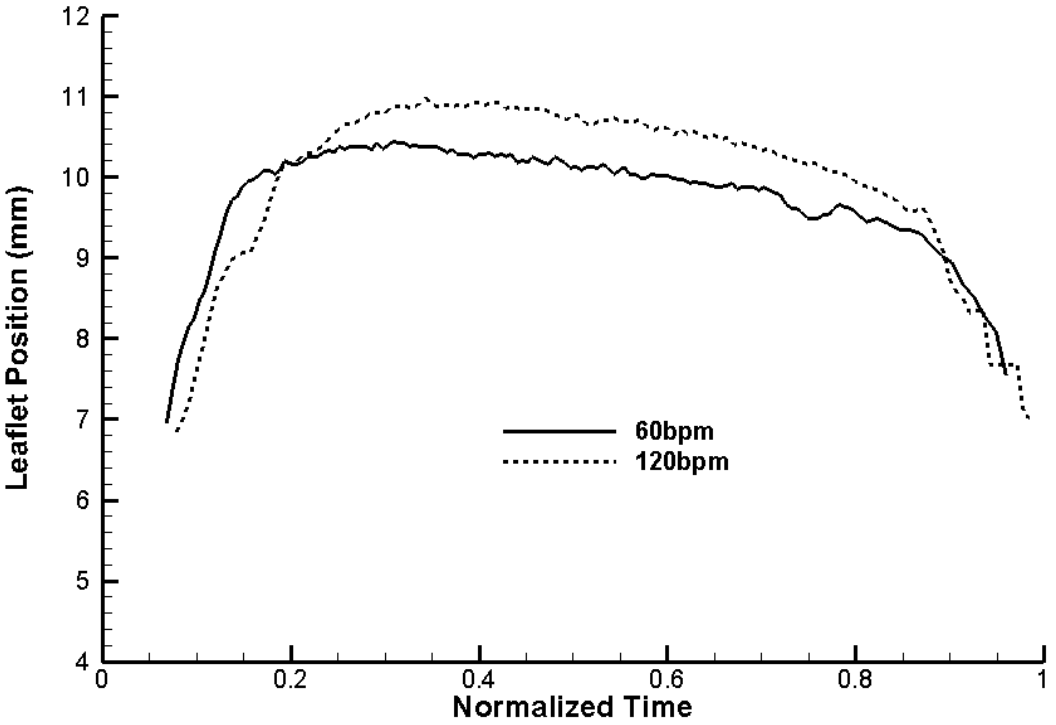

Figure 4.10: Heart rate study leaflet kinematics
Leaflet tip position is plotted against normalized systolic time for both normal (60bpm) and elevated (120bpm) heart rates

4.4.4 Discussion

While similar flow patterns exist, there are key hemodynamic differences between the regular and elevated heart rate conditions. A relatively large scale sinus vortex is present in both cases, but its peak size is smaller for the elevated heart rate condition based on visual

observation. Similarly, velocity magnitude is generally lower at all points within the sinus throughout systole when heart rate is increased. Both of these trends are likely influenced by the decreased systolic time duration in the elevated heart rate condition, which does not allow the main sinus vortex to develop as much as the baseline case (although decreased flow at elevated heart rates also plays a role).

4.5 Sinus Size Effects – Experimental

Aortic valve size is a patient-specific parameter and often varies according to body size. There is a corresponding variation in overall sinus sizes as well as more random variations in sinus aspect ratios (i.e. sinus height/sinus radius). Two different sinus chambers of different dimensions were created and tested with the same model valve. Sinus aspect ratios for the two chambers were approximately 3.4 and 3.9 for the larger and smaller chamber, respectively. Dimensions are given in Figure 4.11.

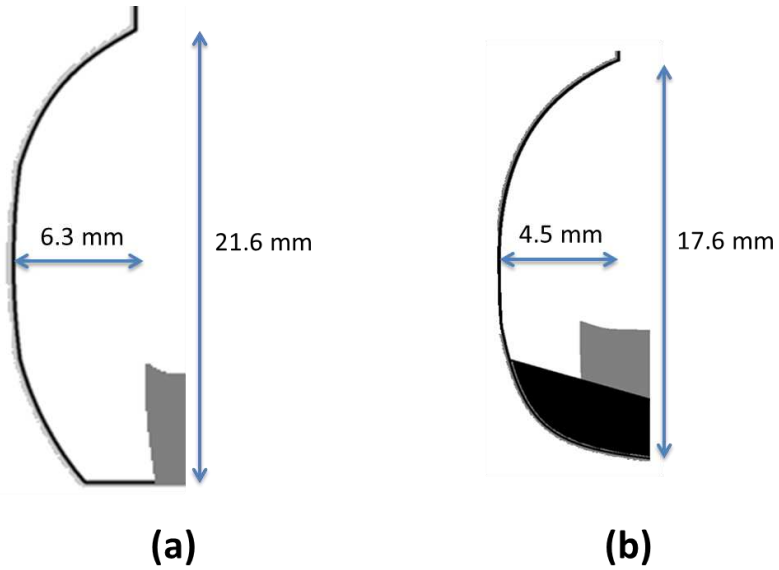

Figure 4.11: Large and small valve chamber sinus dimensions
Sinus height and width (radius) are given for a) small and b) large sinus chamber sizes

4.5.1 Qualitative Results

Qualitative streak videos are shown for two different sinus size cases in Figure 4.12 and snapshots from these videos are included in Figure 4.13. One difference that is apparent during early systole is the radial leaflet opening distance relative to the sinus wall. In the smaller sinus, the leaflet is located much closer to the wall than in the larger sinus. The leaflet free edge is also closer to the sinotubular junction in the smaller sinus case.

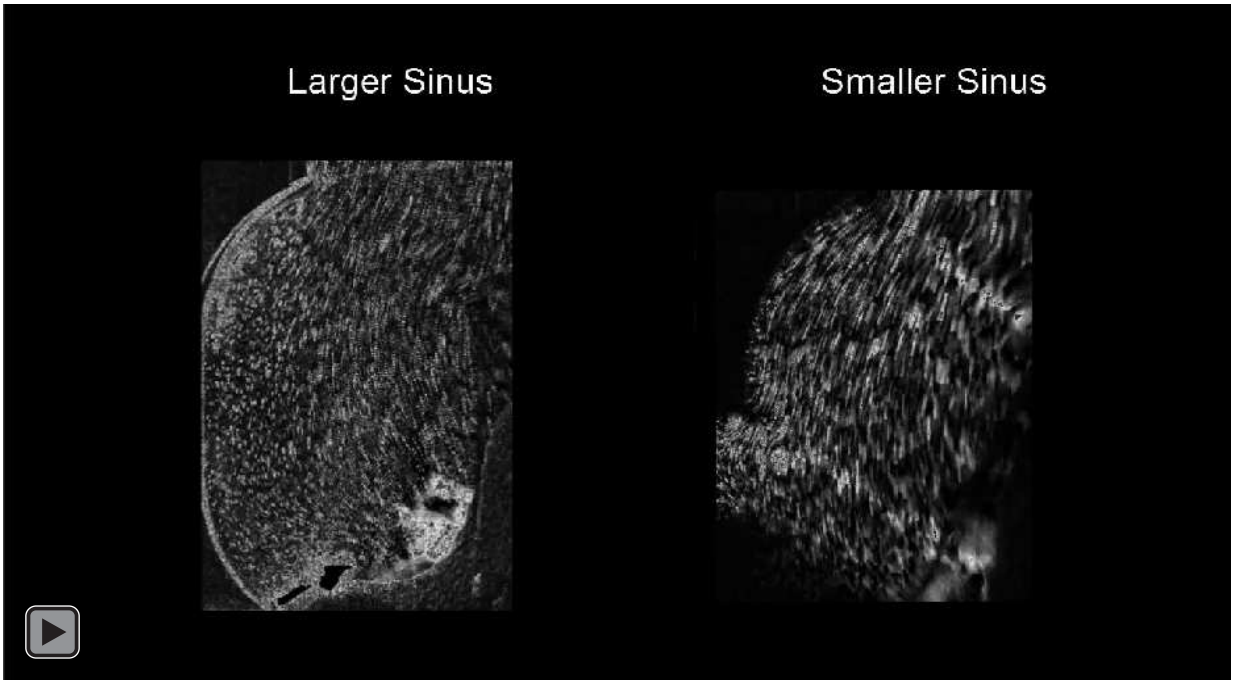

Figure 4.12: Sinus size study streak plot video
Qualitative videos show particle streak paths within the larger and smaller sinus chamber models

From a hemodynamics perspective, overall velocities appear much higher in the smaller sinus as soon as systole begins. There is a sinus vortex that forms in both cases, but it takes longer to develop in the larger sinus and is also located farther downstream in this case. The larger sinus vortex also appears weaker throughout systole. Diastolic flow patterns are generally chaotic and much lower in magnitude for both sinus size cases.

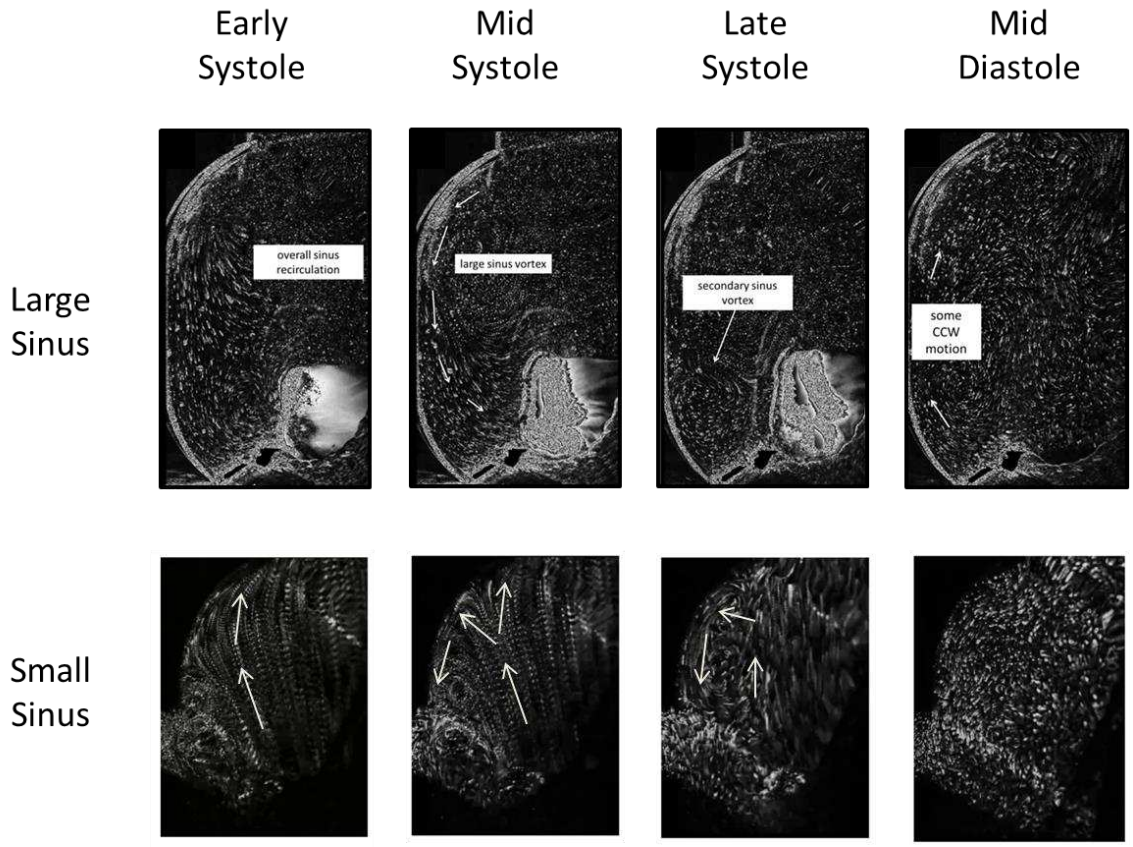

Figure 4.13: Sinus size study particle streak plot snapshots
Snapshots from streak plot videos for larger and smaller sinus cases at four discrete time points throughout the cardiac cycle

4.5.2 Quantitative Results

Figure 4.14 shows velocity and vorticity information within two different in vitro sinus models. As shown in the figure, vorticity magnitude is much higher within the smaller chamber, especially during early and mid systole. Also during early systole, the initial vortex formation occurs near the sinotubular junction in the larger sinus, while this flow structure is initially positioned much closer to the annulus in the smaller sinus. At mid systole, the sinus vortex has migrated upstream in the larger sinus case and downstream in the smaller sinus case, thus residing in a similar location for each model valve chamber. Late systole shows little spatial movement but a significant decrease in strength for each sinus vortex, and there is very little motion during diastole.

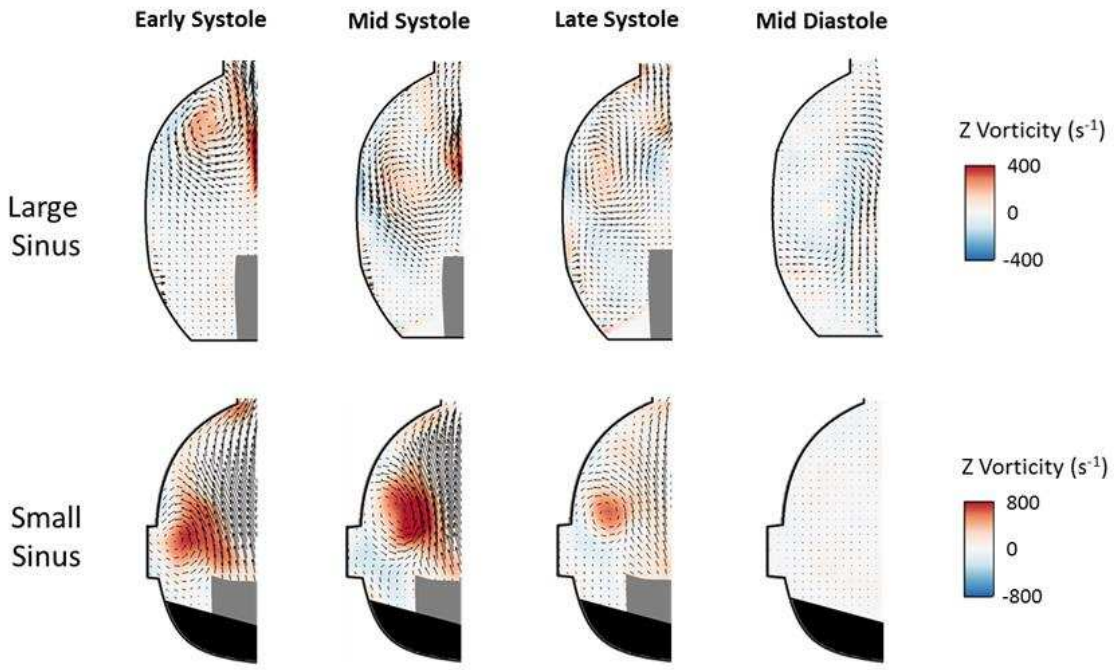

Figure 4.14: Sinus size study velocity vectors and vorticity contours
Effect of sinus size on hemodynamics are shown quantitatively via velocity vectors and vorticity contours. These parameters are shown at four discrete time points throughout the cardiac cycle.

4.5.3 Discussion

The main difference between the two different sinus sizes studied is overall velocity, and therefore vorticity, magnitudes. Peak fluid velocity within the larger sinus reaches about 0.3 m/s while this velocity is nearly 1.6 m/s in the smaller sinus case. There is a similar difference in vorticity magnitudes between the two cases. While this general pattern may be physiological, such large differences are unlikely to occur in vivo. One reason for this discrepancy is the difference between the two experimental setups. The same model aortic valve was used in each valve chamber – one of which was designed specifically to fit the valve while the other was not. This created a flow situation in the smaller sinus chamber where freestream flow was entering the sinus, while it did not in the larger mock aortic root. These two situations were described by Yap et al [102] in relation to leaflet opening angle. While experimental limitations

exist, this study suggests that the fully open location of the leaflet free edge in relation to the sinus could have an effect on sinus velocity magnitudes and therefore vortex strength.

Due to the flush-mounting design of the smaller sinus chamber, it was deemed a more realistic aortic root model. Therefore, this chamber was used for subsequent experimental studies to examine the effects of additional anatomical and physiological parameters on hemodynamics.

4.6 Sinus Size Effects – Computational

Multiple 2D geometric models were created with varying sinus geometries. In these models, the sinus was created using an elliptical shape. The major diameter, or sinus height, was kept constant while the minor diameter, or sinus radius, was varied. Three different sinus radii were chosen to represent patient-to-patient anatomic variability, and the aspect ratio of these three cases was calculated based on the major and minor diameters of the ellipse used to model the sinus. Minor diameters were chosen based on Thubrikar [9], which yielded aspect ratios of 4.6, 2.0, and 1.5 for the narrow, average, and wide sinuses, respectively.

4.6.1 Results

Results from these different sinus aspect ratios are presented in Figure 4.15. This figure shows vorticity contours at three different time points throughout systole for each sinus case. During early systole, a sinus vortex can be seen in the downstream portion of each sinus. The vortex is positioned near the sinus wall in each case, which dictates its spatial relationship to the freestream shear layer that is shed off of the leaflet free edge. In the narrow sinus, the vortex and shear layer appear almost as one structure, while there is a sharp distinction between the two in the average sinus and especially in the wide sinus. At peak systole, the sinus vortex is only slightly noticeable in the far downstream end of the narrow sinus, while it remains apparent

in the other two sinus cases. In the wide sinus, though, vorticity magnitude has decreased relative to early systole while it is similar in the average sinus. There is no evidence of a vortex in the narrow sinus by late systole, while little change has occurred in the average sinus. At this stage in the wide sinus, the vortex is still present but magnitude has further dissipated.

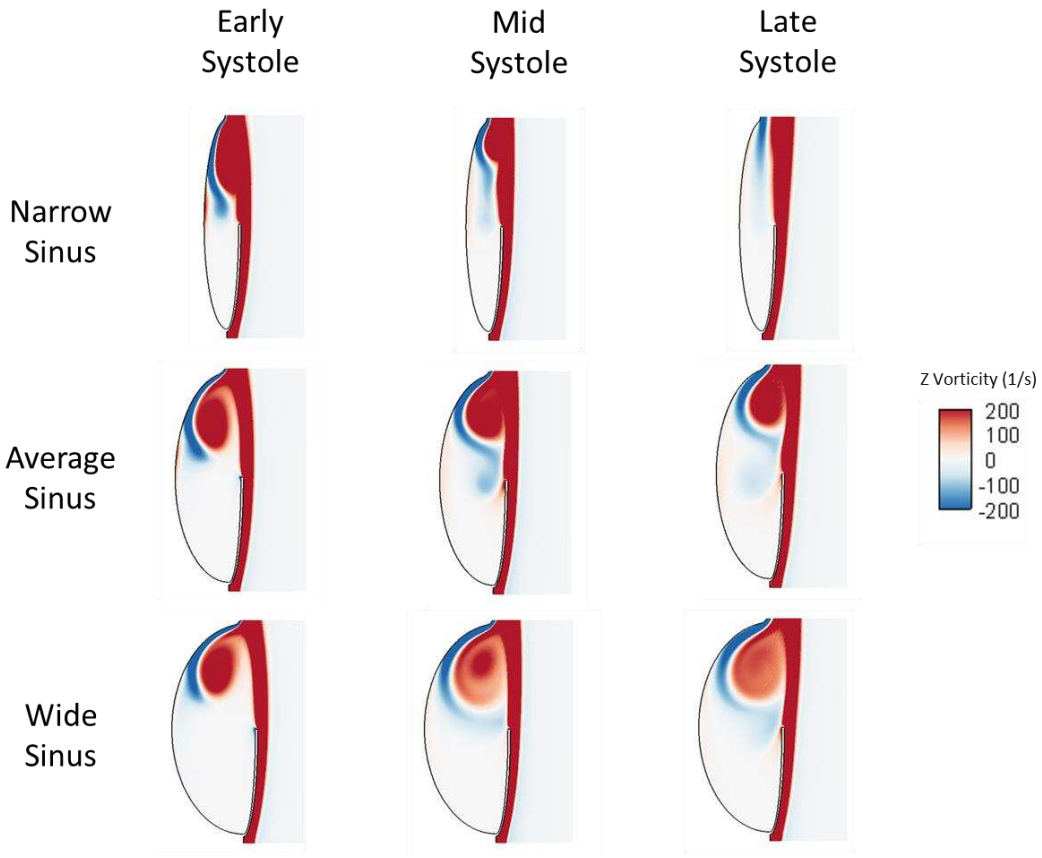

Figure 4.15: Sinus size study vorticity contours – computational
Three different 2D models were created to represent different sinus radii and vorticity contours within each of these sinuses are presented at three systolic time points

4.6.2 Discussion

In all three sinus size cases, the majority of positive vorticity is localized near the downstream end of the sinus. However, this sinus vortex is very small in the narrow sinus and is practically non-existent by late systole for this case. Similarly, in the wide sinus, the vortex is present

throughout systole, but loses strength as vorticity magnitude decreases from earlier to later time points. This trend of diminishing or disappearing vorticity is not present in the average sinus case. Instead, a strong sinus vortex persists throughout systole for this sinus size. This suggests that there could exist an ideal sinus aspect ratio for supporting vortex strength, which is often desirable due to the negative effects from decreased fluid motion in the sinus.

4.7 Aortic Flow Waveform Shape Effects – Experimental

Another hemodynamic parameter of interest studied was the shape of the aortic flow waveform. Three cases were modeled – early, mid, and late peak flow times – and sinus hemodynamics were captured for each case. Since only the systolic portion of the flow curve was altered, there is very little variation in diastolic hemodynamics between each case. Therefore only systolic flow patterns are presented for these different cases.

4.7.1 Qualitative Results

Streak plot videos for each flow waveform are presented side-by-side in Figure 4.16. A notable trend in the video is that the aortic valve opens earliest in the early peak flow case and also closes latest in this case. Some transient leaflet flutter is also apparent for each case, the timing of which corresponds to peak aortic flow. Snapshots from these videos are shown in Figure 4.17. Flow patterns are somewhat difficult to decipher in these still images, so annotations have been manually superimposed to match trends from the video. In general, sinus hemodynamics are similar for each case. During each flow acceleration phase, particle motion within the sinus is mainly streamwise. There is a vortex that develops by peak flow time near the leaflet free edge, and the downstream boundary of this vortex can be seen. At this spatial point, flow is either directed toward the sinotubular junction or back towards the annulus

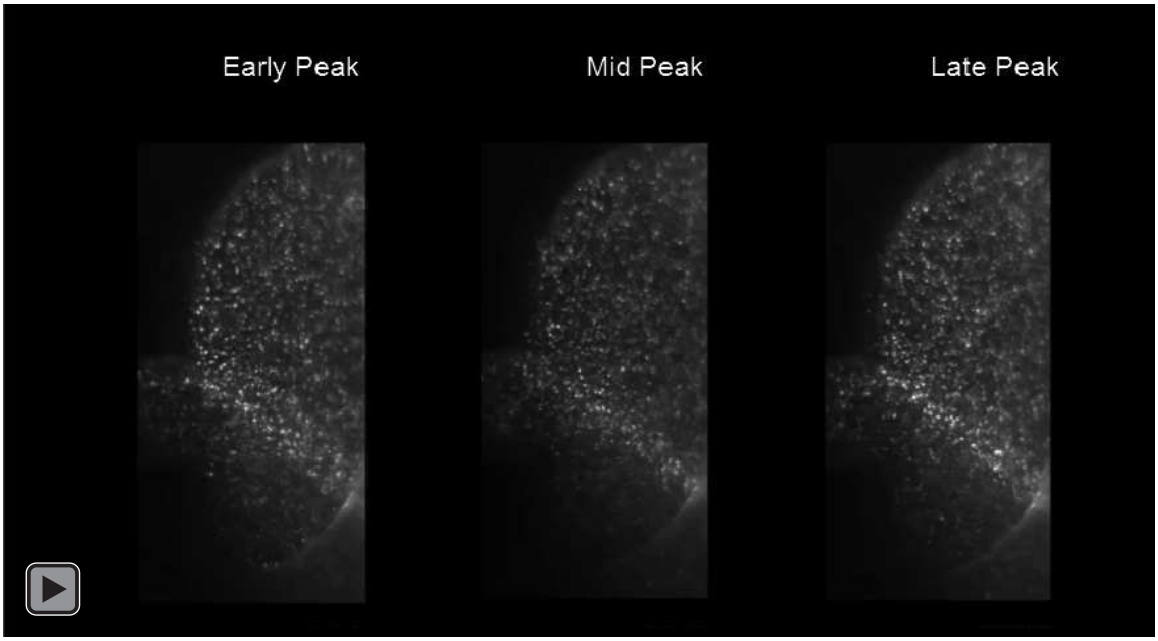

Figure 4.16: Aortic flow waveform study streak plot video
Three different aortic flow waveforms, each with a different temporal location of peak flow, were generated and particle streak paths were computed

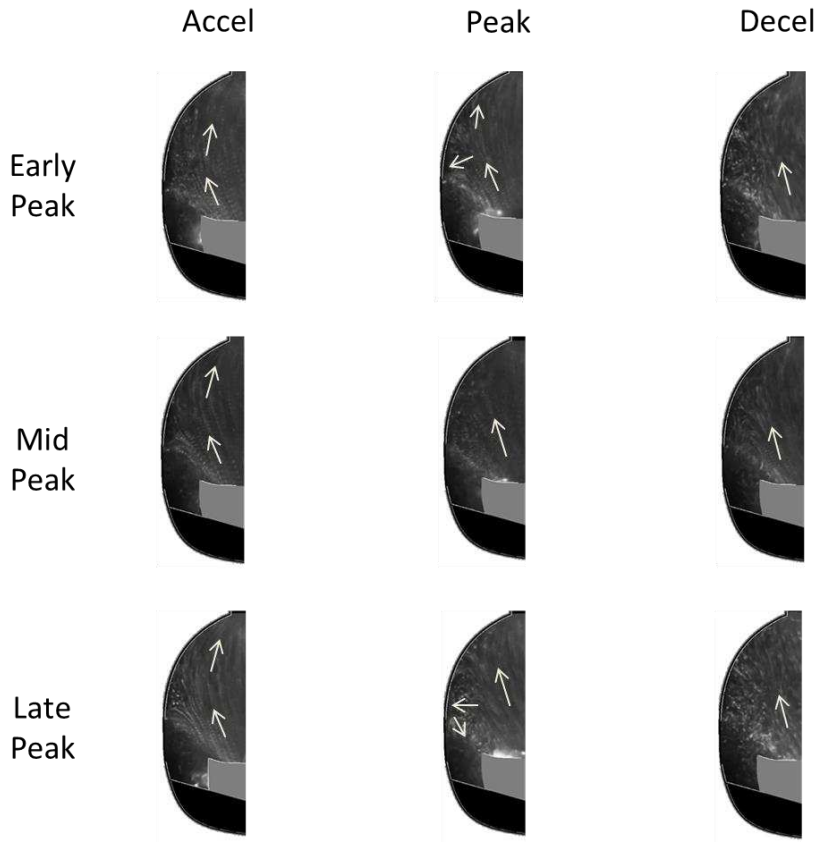

Figure 4.17: Aortic flow waveform study particle streak plot snapshots
Annotated snapshots from streak plot videos are presented for different aortic flow waveform shapes

by curvature of the sinus wall. During flow deceleration, particle velocities are reduced and the sinus vortex has mainly dissipated in all cases.

4.7.2 Quantitative Results

Figure 4.18 shows vector and vorticity plots within the sinus at three systolic stages for the different flow waveforms. These stages of systole (acceleration, peak, and deceleration) are based off of aortic flow magnitude and therefore times do not match up across trials. When the flow is accelerating, there is some slight streamwise motion within the sinus for early and mid peak flow cases. For the late peak flow case, some recirculation has already developed within the sinus by this time point, causing a noticeable vorticity region near the leaflet. By peak

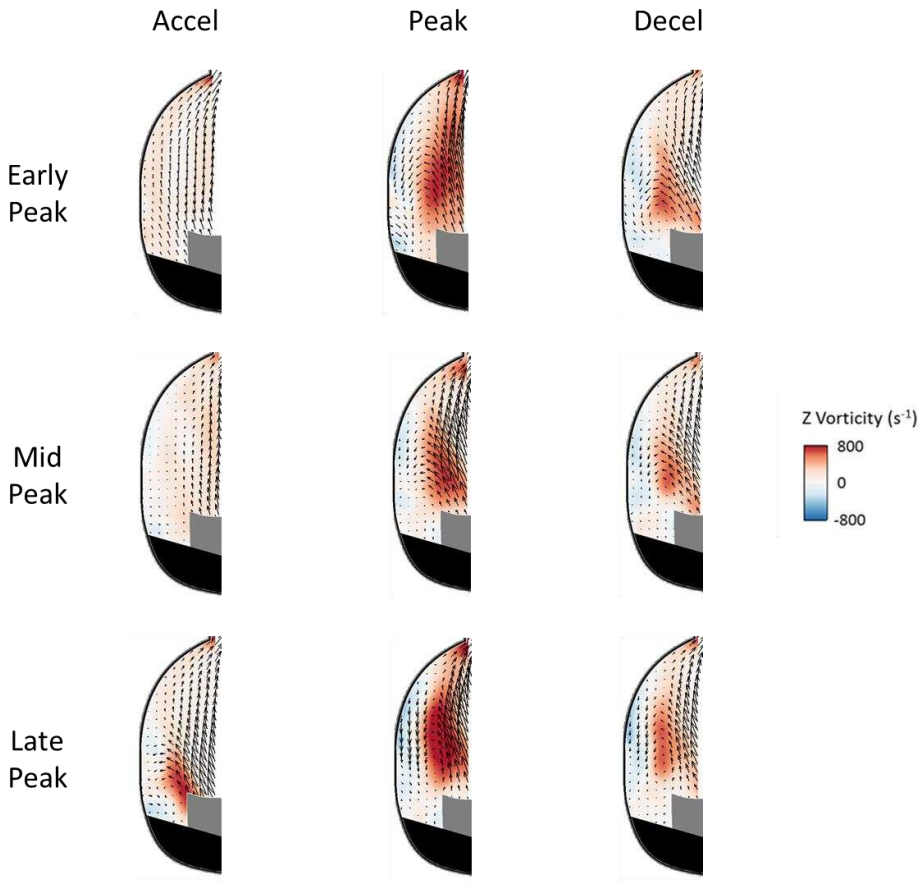

Figure 4.18: Aortic flow waveform study velocity vectors and vorticity contours
Quantitative velocity vectors and vorticity contours are presented at three (systolic) flow stages for three different peak flow times

systolic flow time, a dominant sinus vortex is present in all cases. This vortex is strongest in the late peak case, with magnitudes at peak flow time of 1065, 927, and 1200 s^{-1} for early, mid, and late peak cases, respectively. Once the flow has started to decelerate, the sinus vortex in each case has decreased in strength and vorticity magnitude is similar across the three cases.

Vorticity magnitude was also analyzed continuously across systole rather than at discrete flow stages. Figure 4.19 depicts varying vorticity strength throughout systole at the same central sinus location for each case. It is evident from this figure that the sinus vortex in the late peak case reaches the highest magnitude. Also, the vortex in the early peak case exists for a longer duration than the mid or late peak cases. Average vorticity magnitude at this sinus location throughout systole was 511, 339, and 462 s^{-1} for the early, mid, and late peak cases, respectively.

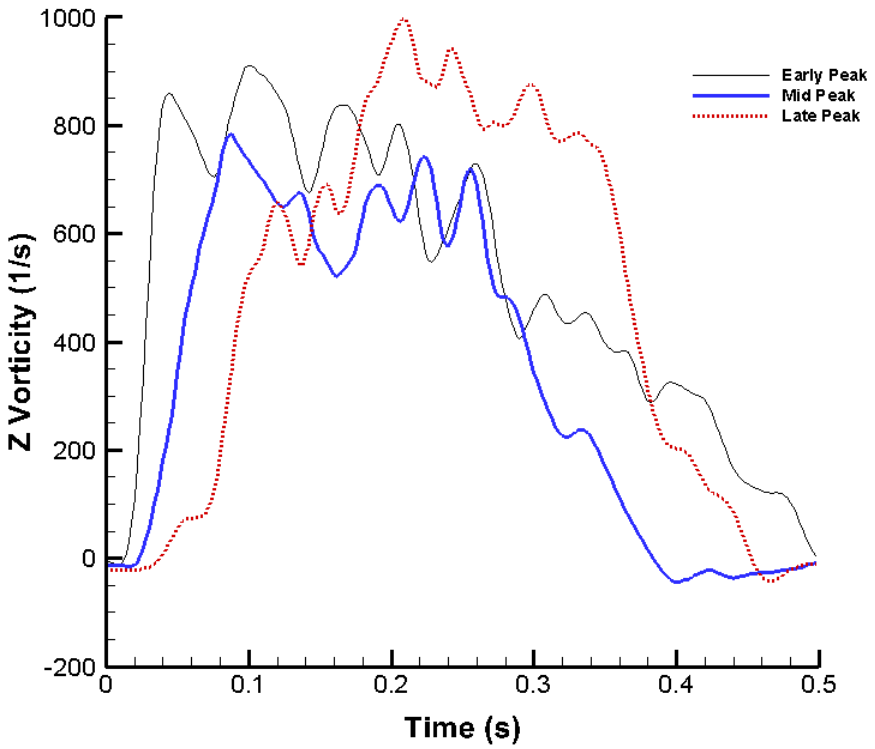

Figure 4.19: Time-varying vorticity magnitude for different aortic flow waveforms
Out-of-plane vorticity was monitored at one sinus location across systole for each peak flow case

Energy requirements for these different flow scenarios were also of interest since different types of flow accelerations have been shown to transfer momentum differently [112]. In order to do so, transvalvular pressure gradient was calculated and is plotted at three discrete systolic time points for each flow case in Figure 4.20. The pressure gradient for the early peak flow case spikes early, reaching a value around 16 mmHg at 0.06 s and is then much lower during the later time points. The mid peak gradient also reaches a maximum (of about 11 mmHg) during the early time point, but then remains near 7 mmHg during the later systolic stages. For the late peak flow case, transvalvular pressure gradient reaches a maximum of about 14 mmHg during mid systole and is still relatively high during late systole. Average systolic pressure gradient was 5.1, 5.7, and 7.8 mmHg for early, mid, and late flow peaks, respectively.

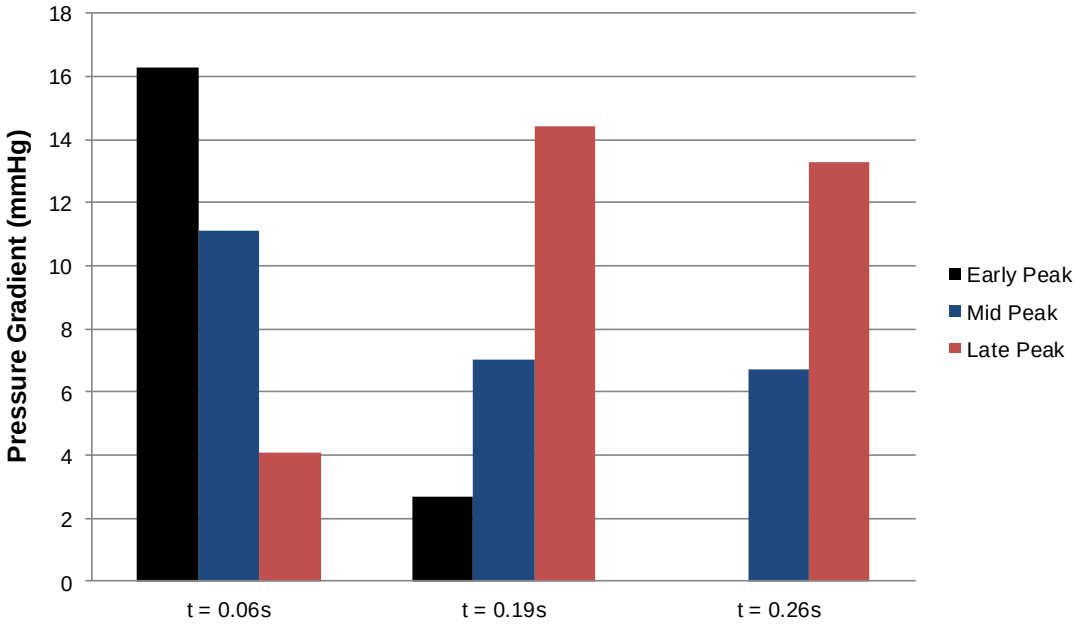

Figure 4.20: Transvalvular pressure gradients for different aortic flow waveforms
Aortic and ventricular pressures were recorded continuously and the difference between these two measurements is plotted over time for the three aortic flow waveform cases

4.7.3 Leaflet Kinematics

Results from leaflet kinematics tracking are presented in Figure 4.21. As shown, the valve stays fully open for the longest time duration in the early peak case and for the shortest duration in the

late peak case. It also opens widest in the early peak case, followed by the mid peak case, and least in the late peak case. There is also some leaflet flutter present in each case that manifests as oscillations in the graph.

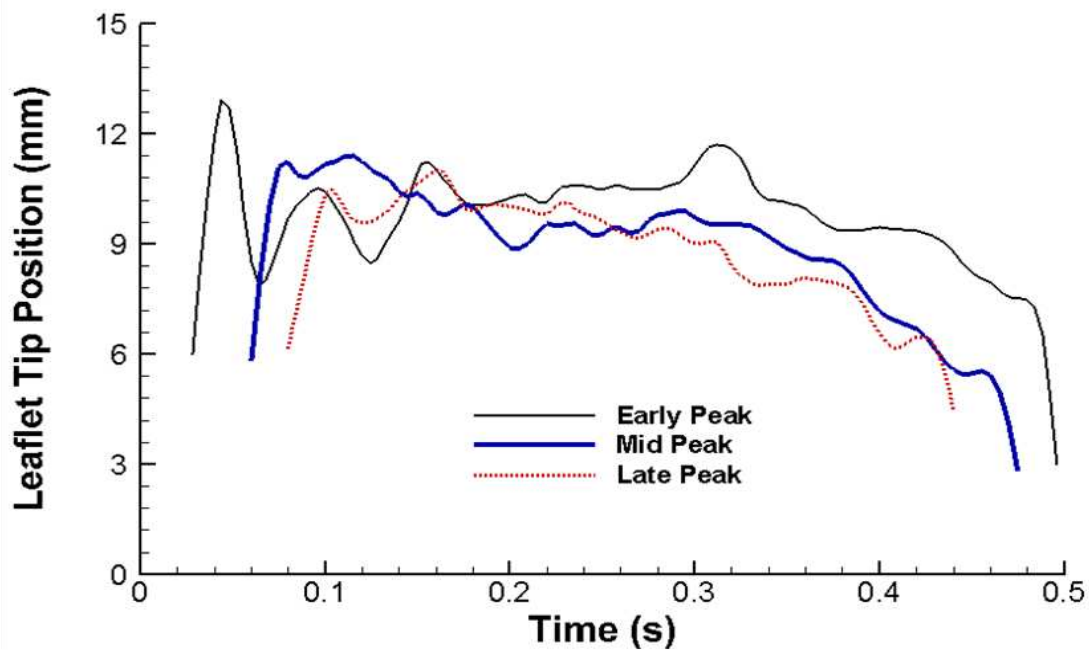

Figure 4.21: Aortic flow waveform leaflet kinematics
Radial leaflet tip position is plotted over time for each aortic flow waveform case

4.7.4 Discussion

There are a few interesting patterns that emerge from these hemodynamic analyses. For example, the highest sinus vorticity occurs in the late peak case and the lowest occurs in the mid peak case, however average vorticity throughout systole is highest for the early peak case. This can be explained by the manner in which the vortex builds and dissipates differently in the early and late peak flow cases. In the early peak case, the vortex builds to full strength rapidly and then stays at that level for a period of time before gradually dissipating. In the late peak case, on the other hand, the vortex is virtually non-existent during early systole before finally starting to grow in strength. It then reaches a peak at late systole and quickly dissipates

completely upon valve closure. This leads to a higher average vortex strength in the early peak case, and these trends are depicted graphically in Figure 4.19.

Pressure gradient results also give insight into the energetic requirements of the pump (i.e. ventricle). This gradient initially spikes and then quickly decreases in the early and mid peak flow cases, while it takes longer to reach a maximum value in the late peak case, but remains high for a longer period of time than the other two cases (Figure 4.20). This leads to the highest average pumping power requirement for the late peak case even when normalized by average aortic flow rate. Total normalized energy required to pump fluid across the valve for each case was 0.0092, 0.0112, and 0.0151 J/(L/min) for early, mid, and late flow peaks, respectively.

4.7.5 Limitations

One limitation involved in this experimental work is the oscillation in pressure signals due to wave reflections within the flow loop. This complicates analysis that involves pressure data, such as the energy requirements due to different aortic flow waveform shapes, however computation of energy requirements is still possible and comparable across cases.

4.8 Coronary Effects – Experimental

This is the first known in vitro study to simulate and analyze the effects of coronary flow on sinus hemodynamics. Such effects are of interest since two out of the three sinuses contain coronary arteries, so any significant differences should be taken into account when modeling the valve. Additionally, flow differences between these sinuses could have implications for valvular disease.

4.8.1 Qualitative Results

Qualitative particle streak plots were created in a very similar manner to previous studies. Videos of these particle streaks are included for one complete cardiac cycle for both non-coronary and coronary cases in Figure 4.22. Snapshots of these videos are included in Figure 4.23, with manually-drawn arrows superimposed to help give an indication of general flow patterns.

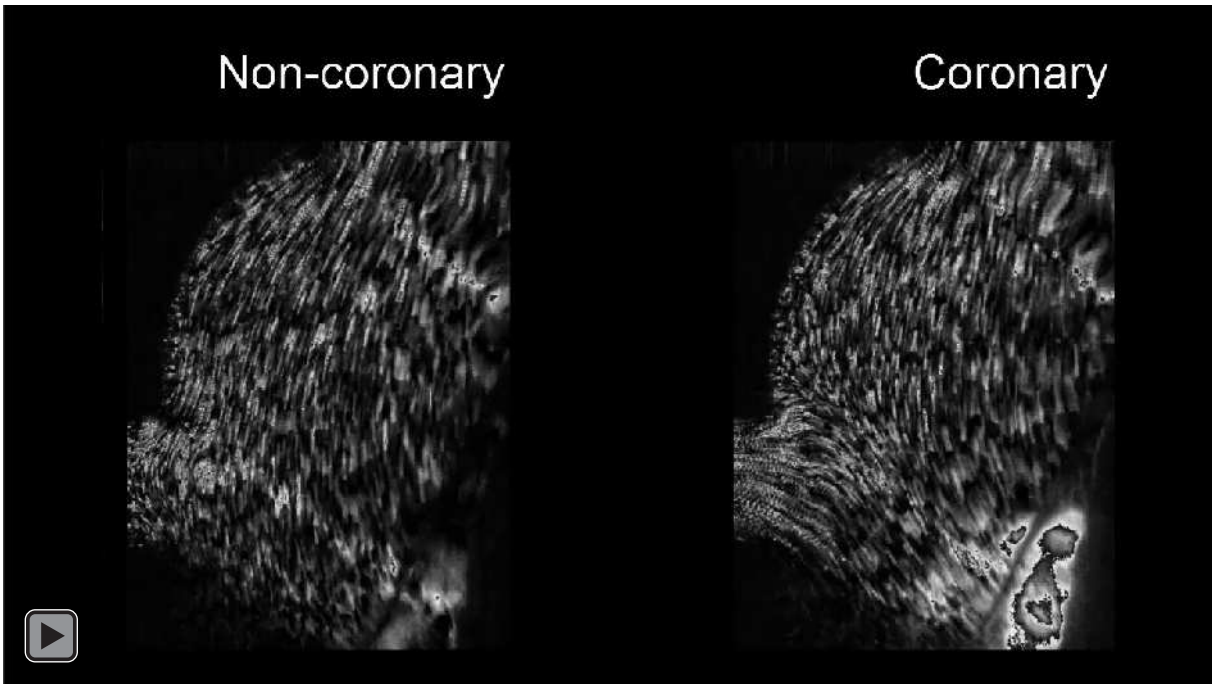

Figure 4.22: Coronary study streak plot video
Qualitative particle streak path videos are presented for non-coronary and coronary sinus cases. The non-coronary sinus case was created by clamping off the coronary artery just downstream of the ostium.

For the non-coronary case, Figure 4.23a shows the development of a sinus vortex during early systole. This vortex is positioned along the wall of the sinus and is relatively small compared to the overall size of the sinus. Additional streamwise flow is also present in the sinus, which is redirected toward the sinotubular junction by the curvature of the sinus wall. As systole progresses, the main vortex migrates slightly downstream (Figure 4.23b), and toward the end of systole flow magnitude decreases significantly in the sinus (Figure 4.23c). During diastole there

is some initial counterclockwise fluid motion (Figure 4.23d), which appears to decay by mid diastole (Figure 4.23e).

Examination of hemodynamics in the presence of coronary flow yields some differences from the non-coronary case. While sinus flow patterns are similar for both cases during early systole (Figure 4.23f), the sinus vortex – present in both cases – is positioned slightly more upstream in the coronary case during mid systole (Figure 4.23g). Additionally there is clear fluid motion near the annulus that is absent when coronary flow is suppressed. During late systole (Figure 4.23h), significant flow can be seen entering the coronary ostium and an area of clockwise rotation is evident just downstream of the ostium. Particle movement is still present near the

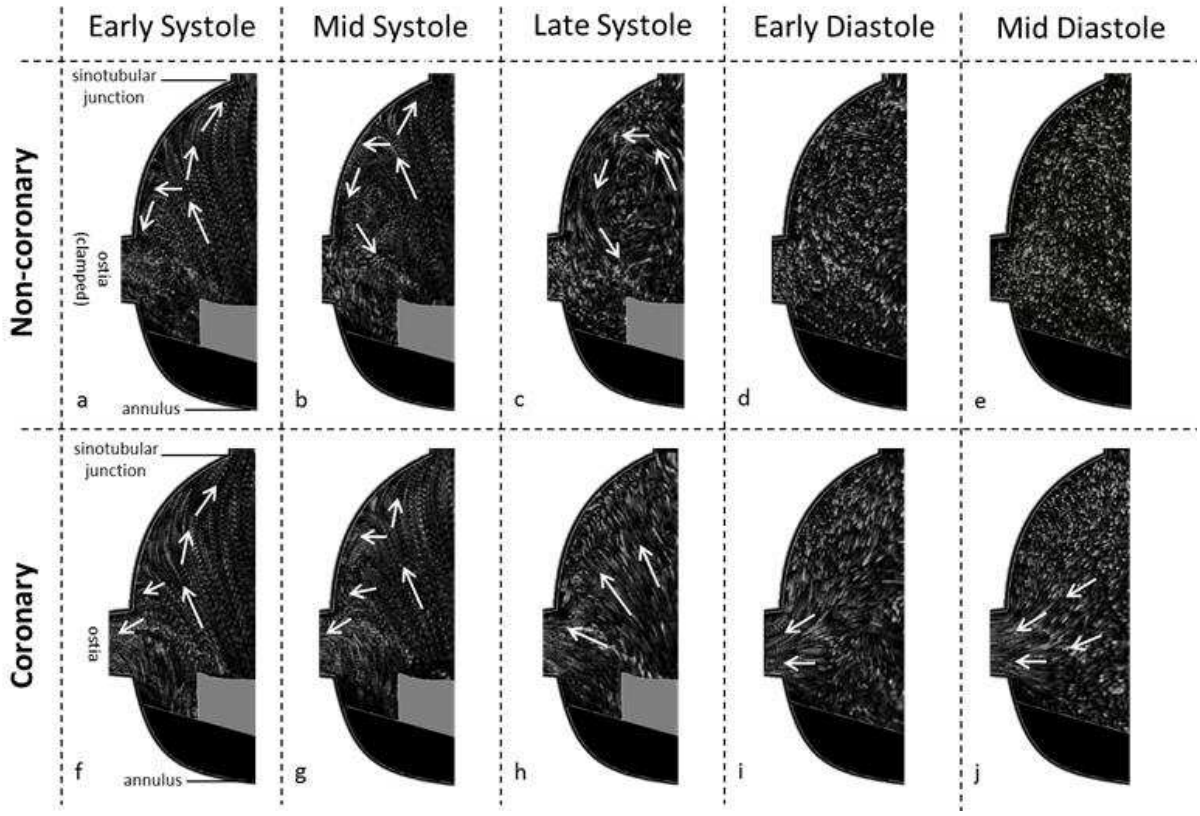

Figure 4.23: Coronary study particle streak plot snapshots
Annotated snapshots from particle streak videos for non-coronary and coronary sinuses. Two (rather than one) diastolic time points are shown since coronary flow is highest during diastole.

base of the leaflet (i.e. at the annulus). These patterns are in contrast to those of the non-coronary case. Particle motion during diastole is mainly noticeable only near the ostium for the coronary case (Figure 4.23i and j).

4.8.2 Quantitative Results

Figure 4.24 shows velocity vectors superimposed over vorticity contours in the sinus for multiple time points throughout the cardiac cycle both with and without coronary flow. These images provide a slightly less intuitive, yet more quantitative, picture of sinus hemodynamics than particle streak plots. However, many common flow patterns are apparent in each.

When viewing velocity fields, similarities to qualitative streak plots emerge. Recirculating flow is present in both sinus cases, however a complete vortex is only seen in the non-coronary case (Figure 4.24a and b). In the coronary sinus, much of the flow near the sinus wall is redirected into the coronary ostium rather than recirculating toward the freestream jet (Figure 4.24f and g). Additionally, there is relatively stagnant fluid near the leaflet base throughout systole in the non-coronary case, in contrast to the same region with coronary flow. This trend is displayed quantitatively in Figure 4.25, which shows time-varying velocity and vorticity magnitudes at different points within the sinus. The velocity magnitude at Position 1 in this figure is significantly higher for the coronary sinus throughout the cardiac cycle. It can also be seen at all time points during systole that there is significant streamwise flow in portions of the sinus closer to the aortic axis. This flow seems to reach deeper into the sinus when coronary flow is present. In diastole, there is less stagnation near the annulus due to the presence of the coronary artery (Figure 4.24d-e and i-j).

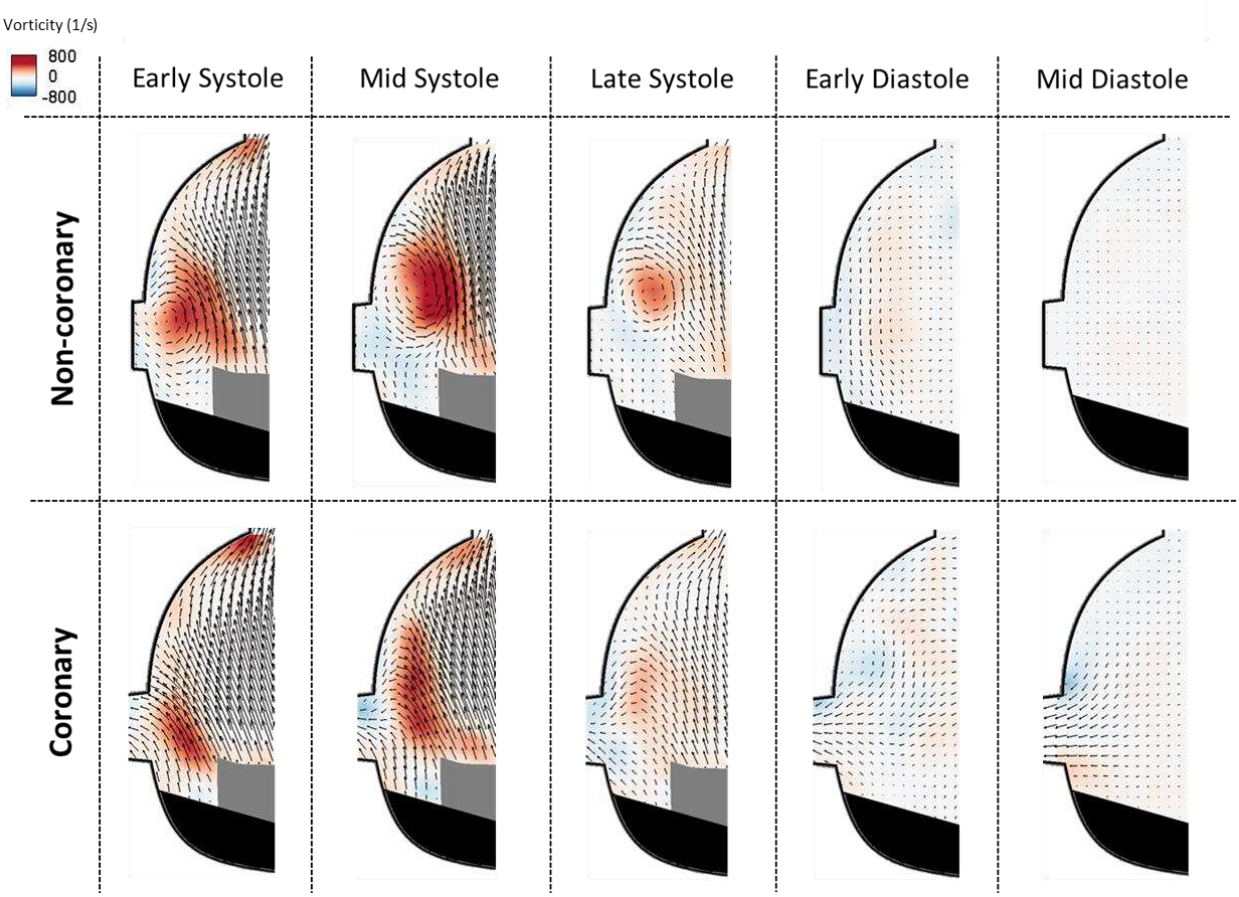

Figure 4.24: Coronary study velocity vectors and vorticity contours
Quantitative results are presented for non-coronary and coronary sinus cases at selected time points throughout the cardiac cycle

One of the more detailed trends that becomes apparent when viewing vorticity contours is the size and location of the high vorticity region during early and mid systole. This region is larger in the non-coronary sinus with higher peak vorticity values. Additionally, the core location of this vorticity is generally located closer to the annulus (i.e. upstream) in the coronary as opposed to the non-coronary sinus. These trends are reflected in Figure 4.25 at Positions 2 and 3. Vorticity magnitude at Position 2, which is closer to the ostium as well as the leaflet, remains higher in the coronary sinus as systole progresses. Alternatively, vorticity is greater at these later systolic time points for the non-coronary case at Position 3. These two trends suggest a systolic vortex that migrates farther downstream in the non-coronary sinus. From late systole to end diastole,

vorticity magnitude is much lower than during the earlier phases of systole. One of the only notable differences in vorticity between the two cases is the relatively weak sinus vortex that is still present in the non-coronary case but is hardly noticeable in the coronary case (Figure 4.24c and h).

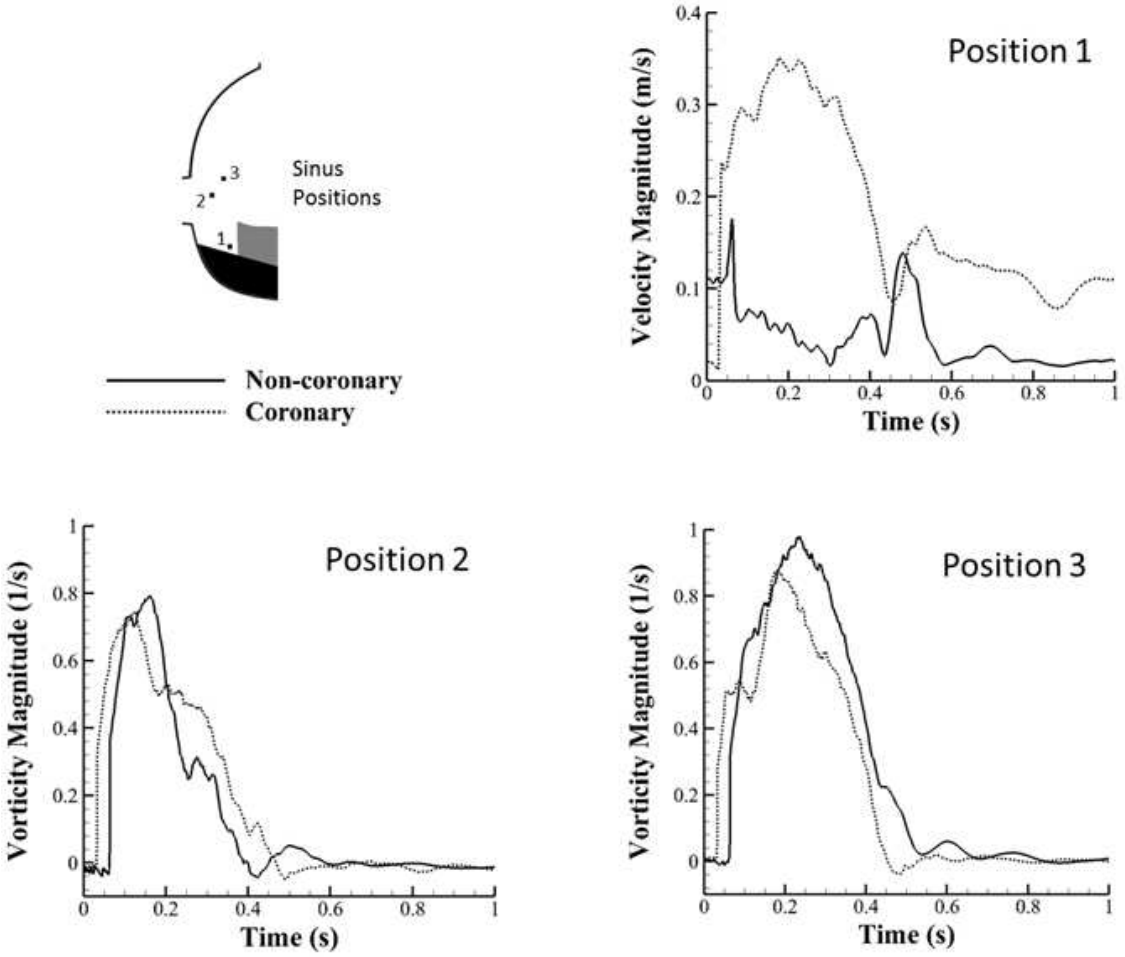

Figure 4.25: Time-varying velocity and vorticity magnitude for coronary study
Velocity and vorticity magnitude were monitored at three spatial locations within the sinus throughout the cardiac cycle. Results are compared for the non-coronary and coronary sinus cases.

4.8.3 Shear Stress Results

Shear stress is often a useful parameter in valve studies since it is a known cause of blood damage and also strongly linked to leaflet calcification [113, 114]. While leaflet wall shear stress was not obtained in this study, fluid shear stress throughout the sinus was computed to

give an order of magnitude of shear stresses in the vicinity of the leaflet. Shear stress contours are presented in Figure 4.26.

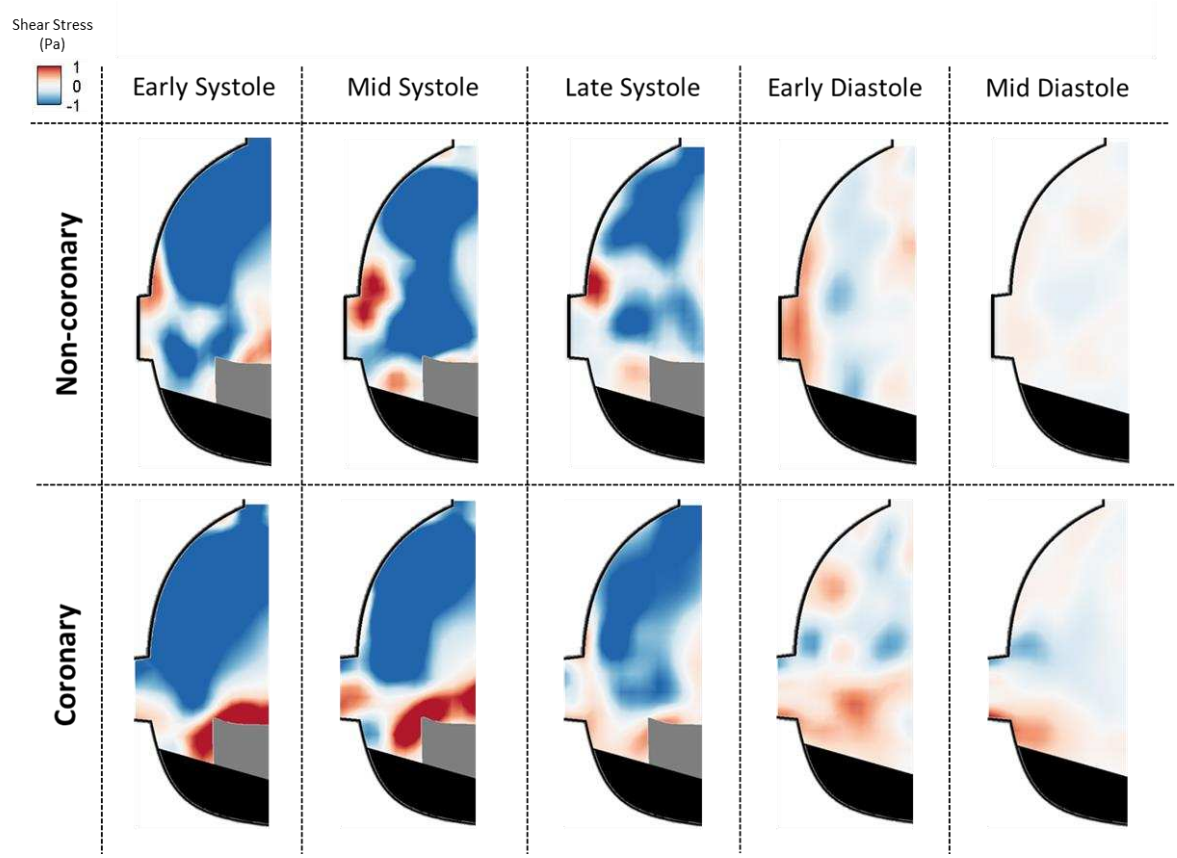

Figure 4.26: Coronary study fluid shear stress contours
Fluid shear stress was computed for all points within both the non-coronary and coronary sinuses and results are presented at selected time points throughout the cardiac cycle.

One of the first notable differences in shear stress due to coronary flow arises during early systole (Figure 4.26a and f). At this point, there is significant shear stress near the annulus between the leaflet and sinus wall in both cases, with magnitudes reaching slightly over 1 Pa. However, this peak shear region is near the sinus wall in the non-coronary case and along the leaflet in the coronary case. Direction of shear is also different for the two cases. Likewise, there is a region of shear on the sinus wall for the non-coronary case that is of opposite direction to the main sinus shear region. At mid systole, shear stress near the annulus is nearly unchanged for the coronary case but has switched direction and reduced in magnitude to around 0.4 Pa for the non-coronary case (Figure 4.26b and g). Near the end of systole, there is

greatly reduced shear in the base of the sinus for both cases (Figure 4.26c and h). At this same time point, there is a positive shear region near the inferior portion of the ostium which is not present at the corresponding location in the non-coronary case. While diastolic shear stress is generally much less, it is still present near the ostium (or where the ostium would be) in both cases during early diastole (Figure 4.26d and i). Once mid diastole is reached the only shear stresses in the sinus are near the ostium in the coronary case, with magnitudes around 0.3 Pa (Figure 4.26e and j).

4.8.4 Leaflet Kinematics

Leaflet tip position was manually tracked and its distance from the aortic axis was subsequently calculated for coronary and non-coronary cases. As seen in Figure 4.27, this distance was generally greater throughout systole for the coronary case. From the initial fully open time point (~10% systolic duration) to start of closure (~85% systolic duration), the coronary leaflet opened an average of 10% farther into the sinus than the non-coronary leaflet.

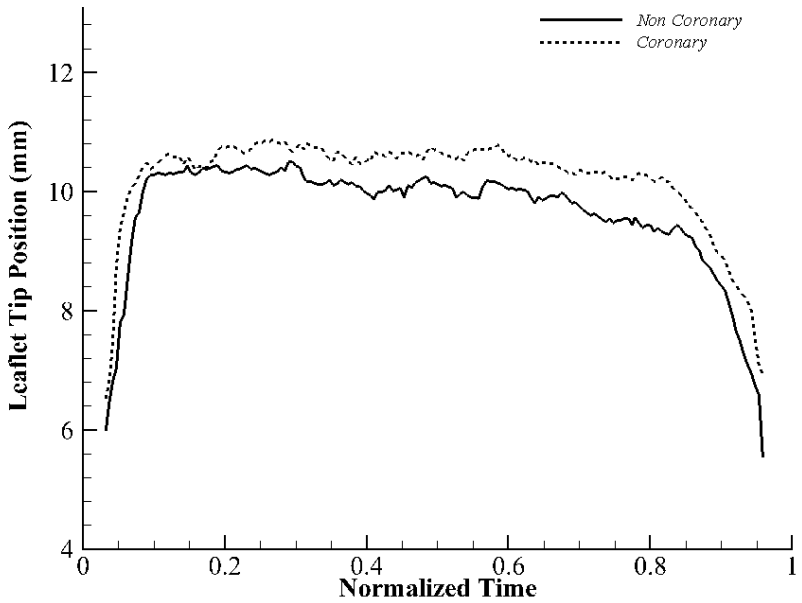

Figure 4.27: Coronary study leaflet kinematics
Leaflet tip position is plotted versus normalized systolic time for the non-coronary and coronary sinus cases

4.8.5 Discussion

Coronary Flow Waveform

The experimental coronary waveform from our model compares both qualitatively and quantitatively to physiological coronary flow [110, 111, 115]. These agreements with in-vivo published data were considered sufficient validation since inherent patient variability prohibits a perfectly ideal coronary waveform.

Hemodynamics

The presence of coronary flow causes numerous changes to hemodynamics. Some of these changes relate to the well-documented sinus vortex [11, 14, 116, 117]. For both native valve sinus cases a distinct zone of high vorticity magnitude, representative of a vortex, did indeed exist. However, in the coronary sinus velocity vectors demonstrate that much of the fluid in this high vorticity region is diverted into the ostium rather than fully recirculating. Therefore, the classical vortex structure is not entirely seen in the coronary sinus. Additionally, this “suction” effect from the coronary appears to pull the vortex more toward the ostium, thus altering its location.

An additional hemodynamic difference between these two cases is present near the aortic side of the leaflet. Increased flow in this region of the coronary sinus could be beneficial as it provides a “washout” effect to move otherwise stagnant blood out of the sinus. This is helpful since stagnation is often associated with thrombosis [118, 119]. Similarly, low velocity fluid causes low wall shear stress on the valve leaflets, which has been strongly linked to inflammation and therefore calcification [113, 119].

Shear Stress

In regards to sinus shear stress, the main area of interest is near the base of the leaflet since wall shear stress on the fibrosa has been strongly linked to calcification. Generally, higher shear stress values are present in this region for the coronary case, with peak magnitudes around 1.2 Pa versus 0.4 Pa for the non-coronary sinus. Additionally, direction of shear stress is constant when coronary flow is present as opposed to without, which demonstrates an oscillatory shear stress pattern. Both low and oscillatory shear stresses have been linked to calcification [120], so these findings could explain the trend of earlier and more frequent calcification on the non-coronary cusp [2].

These factors should be considered in other studies that involve examination of shear stresses along the aortic side of the valve leaflets. This work suggests that differing sinus hemodynamic environments should lead to differing shear stress patterns on the non-coronary and coronary cusps. Results yield a three-fold increase in systolic shear stress near the leaflet in the coronary sinus, which could likely have pathological impact for the non-coronary sinus. However, most studies have neglected coronary arteries when attempting to predict fibrosa shear stress patterns [55, 102, 120]. Therefore, the results from many of these previous studies are largely applicable to the non-coronary sinus only.

Leaflet Kinematics

The coronary leaflet is shown to open farther into the sinus than the non-coronary leaflet. This is likely due to a lower sinus pressure, which could be caused by the coronary ostium providing an alternate path for high pressure fluid in the sinus during systole. Da Vinci first hypothesized that the sinus vortex helped aid in leaflet closure, and recent studies have demonstrated how lowered pressure in the sinus could aid in leaflet opening [11, 121]. The vortex core is positioned between the leaflet free edge and the sinus wall in the coronary case, rather than

downstream of the free edge in the non-coronary case (see Figure 4.25). This creates a low pressure at the center of the vortex that pulls more radially outward on the leaflet in the coronary sinus, which could help explain the greater valve opening in this case.

4.8.6 Limitations

One other limitation was the inability to calculate wall shear stress on the leaflets. This was addressed by computing fluid shear stress throughout the sinus to still give a basic picture of leaflet wall shear stress patterns. Future computational modeling should also help address this issue. Last of all, there was a small amount of signal loss due to blockage of the laser sheet by the coronary tubing adapter, but this was limited to a small sliver in the base of the sinus.

4.9 Coronary Effects – Computational

4.9.1 2D Results

Vorticity contours are shown within the coronary and non-coronary sinus models in Figure 4.28. One of the first noticeable hemodynamic changes present during early systole is the “suction” effect provided by the presence of the coronary ostium. Vorticity from the shear layer downstream of the leaflet free edge is redirected toward the ostia. This pattern does not occur in the non-coronary sinus. Additionally, a negative vorticity region begins to develop in the sinus on the upstream side of the ostium, which is much weaker in the non-coronary sinus. At peak systole, there is a dominant vortex present in the downstream end of both sinuses. Some secondary vorticity also exists in both sinuses near the aortic side of the leaflet. This secondary vorticity is higher in magnitude in the coronary case. Peak systolic hemodynamics persist through late systole, with only a slight decrease in magnitudes for each case by this later time point.

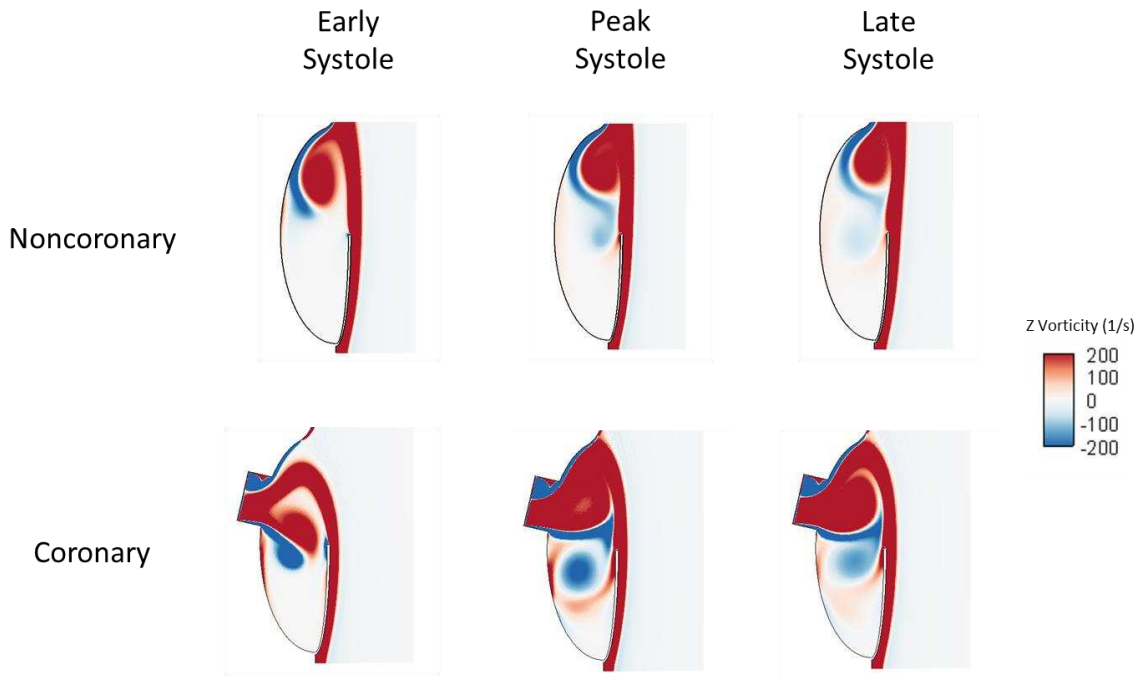

Figure 4.28: Coronary computational 2D study vorticity contours
Vorticity dynamics are shown within the non-coronary and coronary sinuses at three systolic time points for 2D computational models

4.9.2 3D Results

Vorticity contours are also presented for the 3D valve models with and without coronary arteries in Figure 4.29. During early systole, the sinus vortex that is present in the noncoronary sinus takes on a slightly different shape in the coronary sinus. In the latter case, this vortex stretches from the sinotubular junction to the sinus midplane, rather than encompassing just the downstream portion of the sinus. At mid systole, the secondary vortex that is present in the baseline case is not visible when coronary flow is introduced. Instead, there is a region of positive vorticity at this same sinus location. By late systole, the secondary vortex is smaller in size but still present for the baseline case and a positive vorticity region exists near the aortic side of the leaflet. This positive vorticity region is also present in the coronary sinus but is weaker in magnitude.

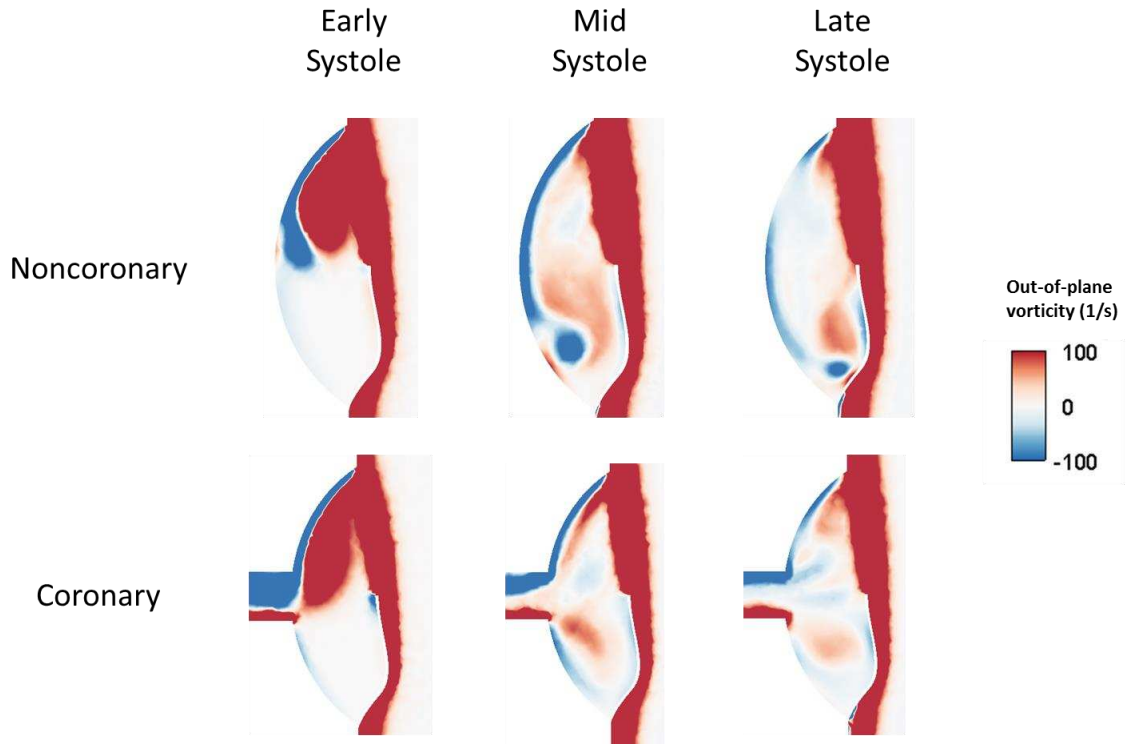

Figure 4.29: Coronary computational 3D study vorticity contours
Vorticity dynamics are presented for two different 3D models – with and without coronary arteries. A 2D slice was taken through the midplane of one sinus for each case.

Streamlines were also created for the 3D coronary model and are shown in Figure 4.30. These images are again shown at different viewing angles to help gain an understanding of the 3D nature of flow patterns. At early systole the hemodynamic environment is similar to the baseline case, where streamlines depict a smooth sinus vortex. However, in the presence of coronary flow, these streamlines reach deeper into the base of the sinus before recirculating into the freestream flow. There is still 3D motion from the sinus midplane toward the commisures at this time point when coronary flow is introduced. At mid systole, flow patterns are similar to those in the non-coronary sinus. Specifically, two vortices can be distinguished on either side of the sinus mid plane. There is also some flow into the coronary artery between these vortices. By late systole, sinus flow is very unsteady. Examination of the side view during this time point, however, shows a general pattern of counterclockwise fluid movement. Streamlines follow a

path from the sinotubular junction, past aortic side of the leaflet and along the sinus wall into the ostium.

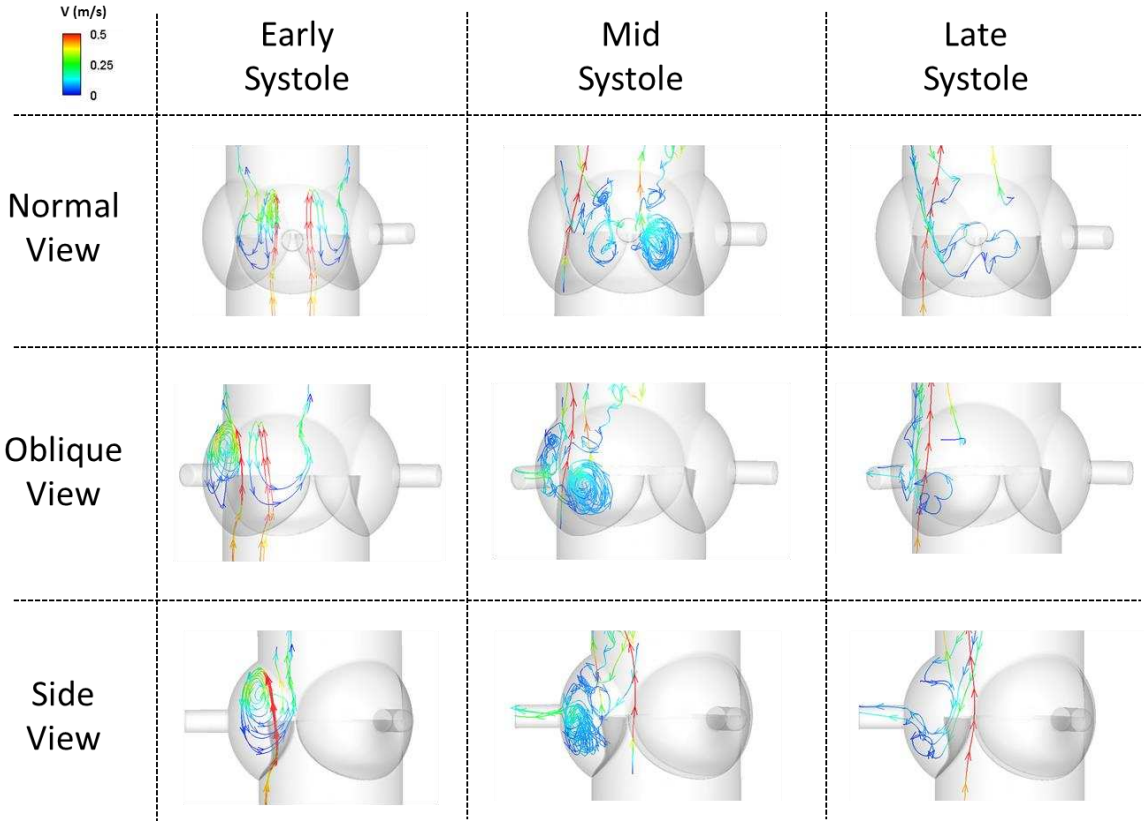

Figure 4.30: Coronary computational 3D study streamlines
Streamlines within the coronary sinus are presented at three systolic time points and different viewing angles and at three different viewing angles

4.9.3 Discussion

The sinus vortex stretches deeper into the sinus in the coronary case during early systole, which could indicate a beneficial effect from coronary flow. During mid and late systole, however, vorticity magnitudes are lower overall in the coronary sinus. However, there is very little counterclockwise vorticity in the coronary sinus, which indicates a reduced likelihood of oscillatory shear stress developing on the non-coronary leaflet. This could be beneficial since oscillatory shear stress patterns have been linked to development of leaflet calcification.

The positive vorticity region that is seen near the base of the sinus in the coronary case is consistent with vorticity dynamics from experimental work. While a secondary recirculation is noted in the non-coronary sinus both experimentally and computationally, coronary flow appears to eliminate this trend. Instead, fluid moves in a counterclockwise manner from the base of the sinus into the ostium in the coronary case. This trend is seen in both experiments and computational simulations.

4.10 Ostia Location Effects – Computational

After a coronary model was established, this geometry was modified to create two additional sinus anatomies with different ostium locations. These locations were chosen based on (non-anomalous) anatomical ranges given by previous studies [9, 108]. The lower limit of this range yielded an ostium location at the level of the leaflet tip (also at the midpoint of the sinus), with an average location of 3.5 mm above the leaflet and an upper limit of 7 mm above the leaflet. In each case, the coronary artery was oriented normal to the sinus wall.

4.10.1 Results

Sinus vorticity contours are shown in Figure 4.31 for these different ostium locations. At early systole, there is a significant region of positive vorticity within the low ostium sinus, however a vortex shape is not easily distinguished. Vorticity from the shear layer that is shed off of the leaflet tip curves downward and into the ostium where it joins with vorticity from the sinus vortex. This vorticity region is located closer to the sinotubular junction as the ostium location also moves toward this junction, and a more classical vortex shape appears for the highest ostium sinus case. At peak systole the positive vorticity region stretches from the sinotubular junction to the ostium in all cases, thus creating a larger vortex as the ostium location moves closer to the base of the sinus. A secondary vortex of opposite rotation direction is established for all

cases on the annulus side of the main vortex at this time point. A strong positive vorticity region is still apparent in each case by late systole, although some decrease in magnitude is apparent in each case. Likewise, a secondary vortex is still seen deeper in the sinus by late systole but has dissipated in each case relative to peak systole.

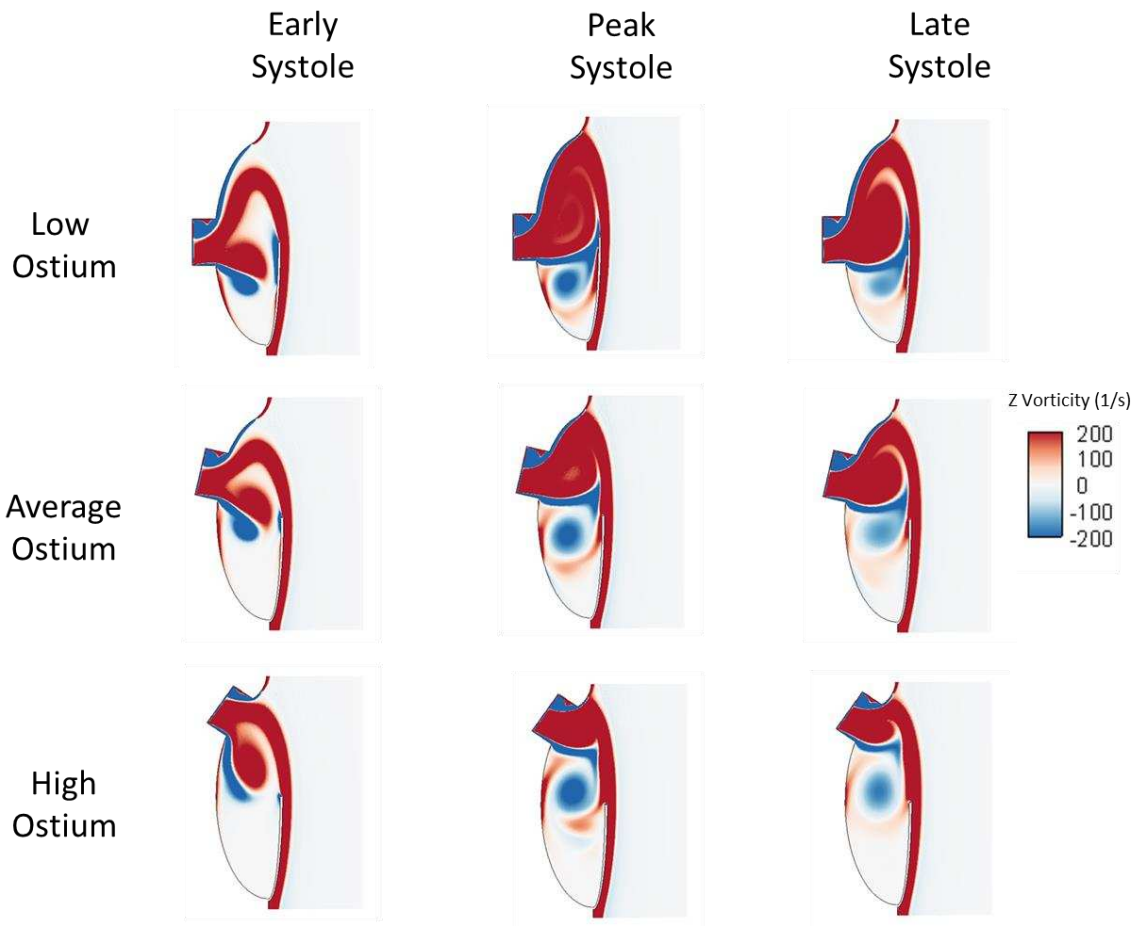

Figure 4.31: Ostium location computational 2D study vorticity contours
Three different 2D models were created to represent different coronary ostium locations and vorticity contours within each of these sinuses are presented at three systolic time points.

4.10.2 Discussion

As the ostium location becomes lower, the main sinus vortex becomes larger. This is likely because the reduced pressure in the coronary artery draws fluid towards it. Therefore, an ostium location farther from the center of the vortex (as determined by the non-coronary sinus

case) will tend to stretch this vortex and cause it to encompass more of the sinus, which is generally regarded as a better scenario for valve health. It is interesting to note that the average ostium location case displayed vortex dynamics most similar to the non-coronary case.

4.10.3 Limitations

One limitation of this study was the boundary condition at the coronary artery outlet. A time-varying velocity was prescribed at this location due to availability of clinical data. However, a pressure boundary condition may be more appropriate in this scenario since the gradient between the sinus and coronary artery outlet is what drives the flow. In this way, a different sinus location could yield a different pressure gradient and therefore different coronary flow velocity. This might explain why a lower, non-physiological, ostium location appears to have the most positive benefit on sinus hemodynamics.

4.11 Coronary Flow Rate Effects – Computational

The coronary flow waveform used in previous simulations (taken from experimental data) was used to model different flow rates by multiplying by a constant, thus retaining the waveform shape but adjusting the magnitude. A range of flow rates was chosen based on multiple previous studies [122, 123]. Three cases were modeled: low, average, and high coronary flow rate, which corresponded to average systolic flow rates of 46, 92, and 138 mL/min, respectively.

4.11.1 Results

Results for these three different cases are presented at the three previously mentioned systolic time points of interest in Figure 4.32. Vorticity contours at early systole show a similar hemodynamic landscape for each coronary flow scenario. The main difference is that sinus vorticity is located closer to the ostium in the higher flow rate cases. At peak systole, vorticity

patterns are very similar for each case, but there is a slight increase in strength of the main and secondary vortices as coronary flow rate is increased. By late systole, the sinus vortex is separate from the ostial flow in the low coronary flow case while it is still stretched into the ostium in the average and high flow cases.

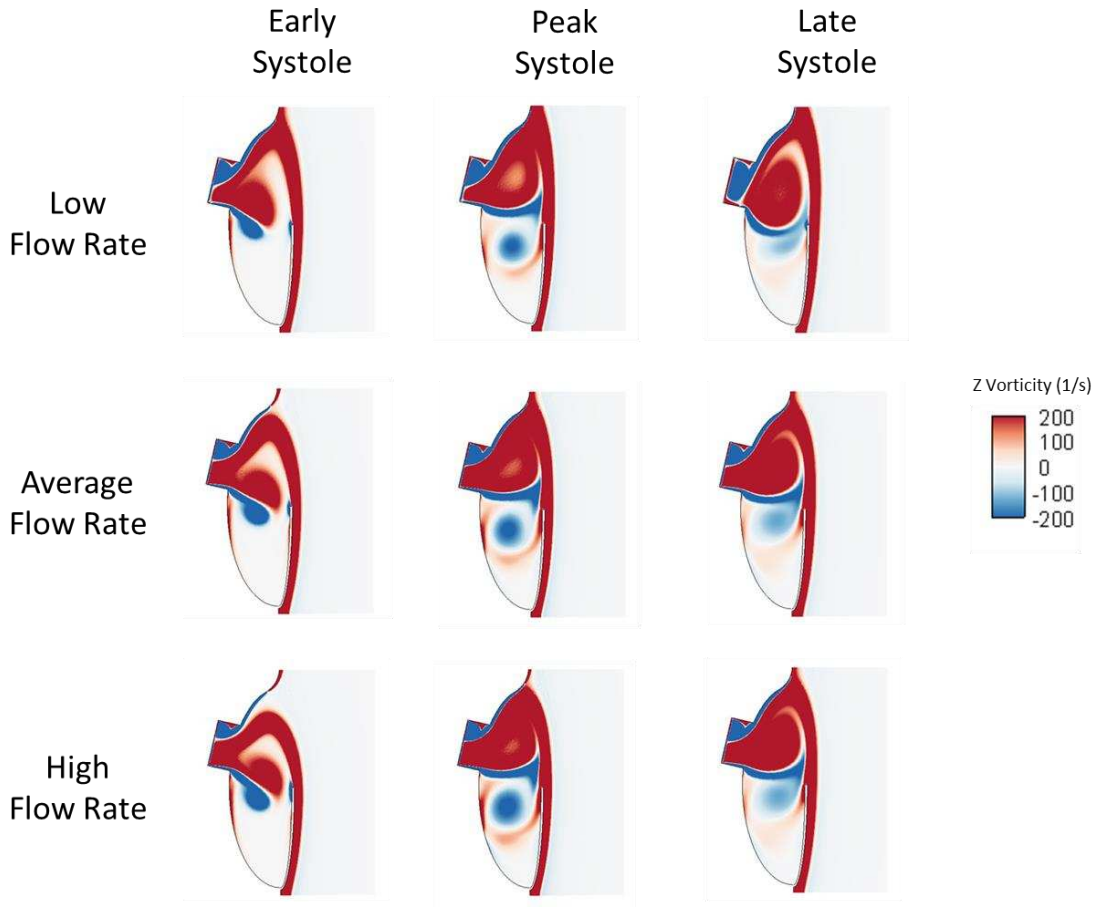

Figure 4.32: Coronary flow rate computational 2D study vorticity contours
Three different 2D models were created to represent different coronary flow rates and vorticity contours within each of these sinus models are presented at three systolic time points.

4.11.2 Discussion

Higher coronary flow rate appears to energize the sinus vortex, thus yielding higher vorticity magnitudes within the sinus. This difference in magnitude is the most notable flow difference as vorticity contours display very similar spatial patterns between cases. As previously stated,

stronger sinus vorticity is generally beneficial for valve health when other parameters are relatively unchanged. Therefore, higher coronary velocity is likely healthier for the aortic valve.

4.12 Chapter Summary

In conclusion, varying different anatomic and hemodynamic parameters can significantly affect sinus hemodynamics. These hemodynamic impacts were highly sensitive to changes in sinus geometry. Both computational and experimental findings showed weaker primary and secondary sinus vortices for a larger sinus, while simulation results also suggest very little to non-existent vorticity when the sinus is too narrow. Another parameter tested – aortic flow waveform shape – showed only minor impacts on sinus vorticity dynamics but did influence the energy requirements of the left ventricle.

The introduction of coronary flow did not bring significant change to the structure or shape of the main sinus vortex. However, there were notable differences between these two sinus cases near the base of the leaflets, where there is flow into the ostium in the coronary sinus. This coronary flow near the base of the sinus creates some positive vorticity that is not seen in the non-coronary sinus. However, some type of “washout” flow was present in both baseline non-coronary and coronary sinuses, which is generally considered beneficial for prevention of leaflet calcification and thrombosis. Diastolic sinus flow velocities were significantly increased due to the introduction of coronary flow, which could also be beneficial from a disease standpoint. Finally, ostia location appears to regulate the size of the main sinus vortex and coronary flow rate was seen to influence vortex strength. However, further experimentation is likely required to verify the impacts of these two parameters due to the limitations of the 2D simulations.

5. SPECIFIC AIM 3

Evaluate the hemodynamic impacts of different prosthetic aortic valve implantations

5.1 Chapter Introduction

The main goal of Specific Aim 3 was to examine sinus hemodynamics that result from recently developed aortic valve implantations. Two types of prosthetic valves were chosen: TAVI and sutureless. The specific TAVI valve used was a Medtronic CoreValve and the particular sutureless valve used was the ATS 3F Enable. Methodologies developed in both previous specific aims were employed to study these valves. Only experimental protocols were used for this aim, so no computational results are given and no distinction between these two methods is given in the section headings. This work has led to two conference publications [106, 124] and one submitted journal manuscript.

5.2 Methods

5.2.1 Valve Models and Sinus Chamber

A 26mm Medtronic CoreValve was studied. It was placed inside the model native valve used in Specific Aims 1 and 2 (i.e. Medtronic Hancock II), which was flush-mounted inside the valve chamber. In this way, a typical TAVI implantation, in which the native valve is left in place, was modeled. While this may suggest a valve-in-valve scenario, it better represents a standard transcatheter implantation in this particular scenario. This is because the acrylic sinus chamber was machined to fit smoothly around the prosthetic valve, thereby exposing only the leaflets to the fluid region. By minimizing the profiles of the stent posts and suture ring, the bioprosthetic valve acts much more like a native valve that a bioprosthesis.

The 26mm TAVI valve used was chosen to match annular size with the native valve. Its location relative to the native valve was determined based on clinical findings, which suggest an ideal TAVI leaflet location that extends just downstream of the native leaflets [125]. This valve combination and TAVI placement location also compare well with published recommendations for valve-in-valve implantation [126]. Sinus hemodynamics for this case were again captured with and without coronary flow.

The final valve tested was a 27 mm ATS 3F Enable stented, sutureless bioprosthesis made of equine pericardial tissue. This valve was tested in a chamber specifically designed to match its dimensions and was not studied with coronary flow. Due to the nature of this valve, no machining was needed between the sinuses for a proper fit between the valve and the chamber. Dimensions for this chamber included an aortic diameter of 29 mm, a sinus radius of 19 mm, and a sinus height of 22 mm. These two prosthetic valves and custom valve chamber are shown in Figure 5.1.

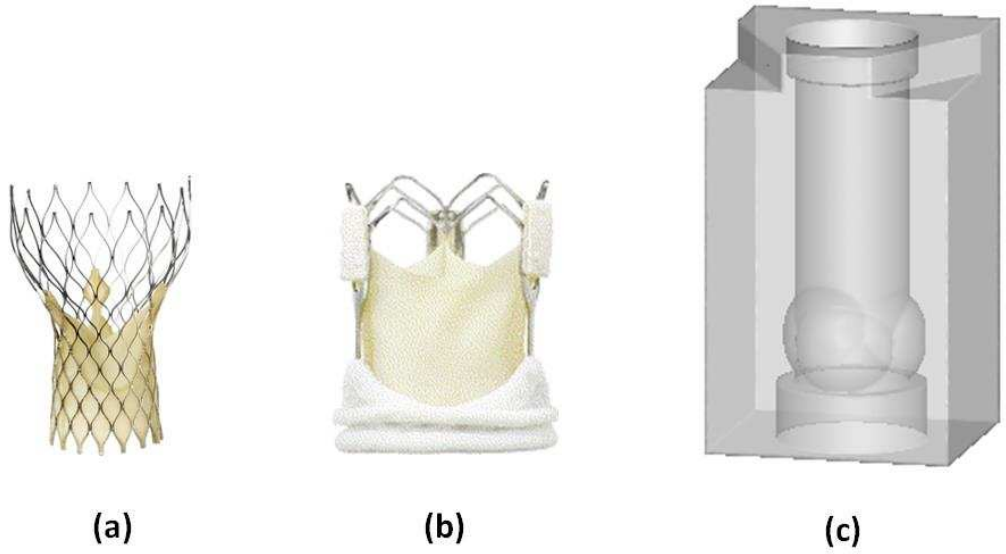

Figure 5.1: Prosthetic valve models and sinus chamber
Different valve models were used including a a) Medtronic CoreValve transcatheter aortic valve implantation (TAVI) and an b) ATS 3F Enable sutureless valve. c) A custom valve chamber was fabricated to house the sutureless valve due to its unique geometry.

This chamber has a rectangular, rather than trapezoidal, cross section as opposed to the previous chambers that were fabricated. The angled profile was meant to provide an optimal view of the sinus region with minimal blockage from the surgical valve stent posts. Since this chamber was made specifically for the sutureless valve, no such viewing adjustments were necessary since the valve does not contain stent posts. Therefore, PIV was conducted with the camera positioned at a 90 degree angle to the laser sheet, which bisected one sinus.

5.2.2 Flow Parameters

Coronary flow waveforms for both the native model valve and the TAVI valve are shown in Figure 5.2, along with the native aortic valve flow waveform (which was essentially the same for the native and TAVI valves). There were slight differences in coronary flow magnitude between

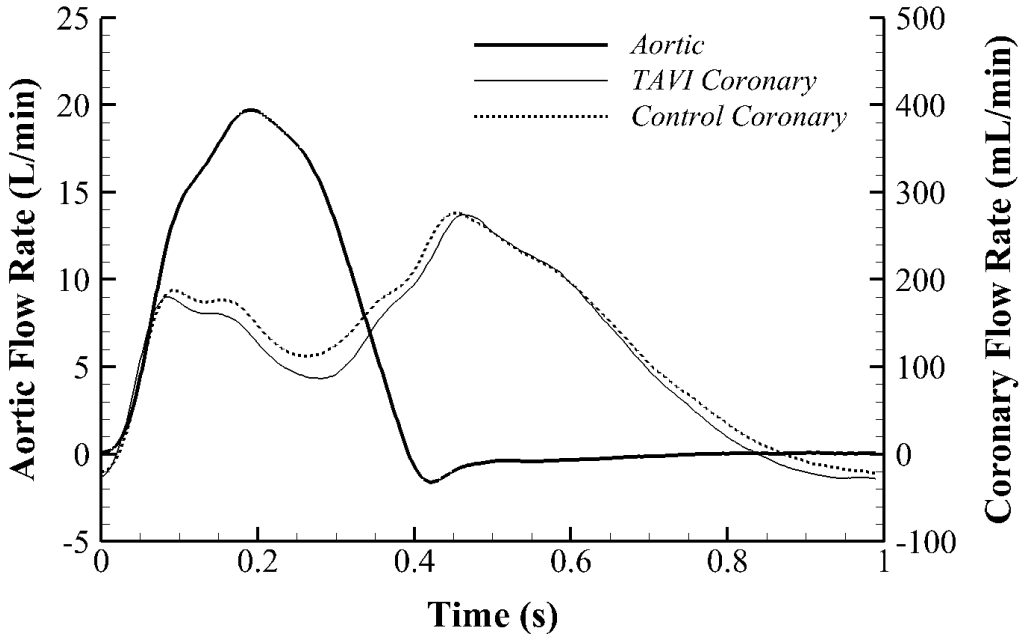

Figure 5.2: Coronary flow waveforms for native and TAVI valve cases
Coronary flow curves are shown for native and TAVI valve cases. The native valve aortic flow waveform is also plotted as a reference, which was very similar to the TAVI valve aortic flow waveform.

the native valve case and the TAVI case, specifically during systole. During this phase, flow was lower for the TAVI case, with an average difference in systolic flow rate of approximately 20 ml/min.

The aortic flow waveform for the sutureless valve is shown in Figure 5.3. Flow rate for this valve peaks around 26 L/min, and a moderate amount of regurgitation can be seen as the curve dips below zero during early diastole. Peak backwards flow during regurgitation is around 7 L/min for the sutureless valve case as opposed to about 2 L/min for the native valve case.

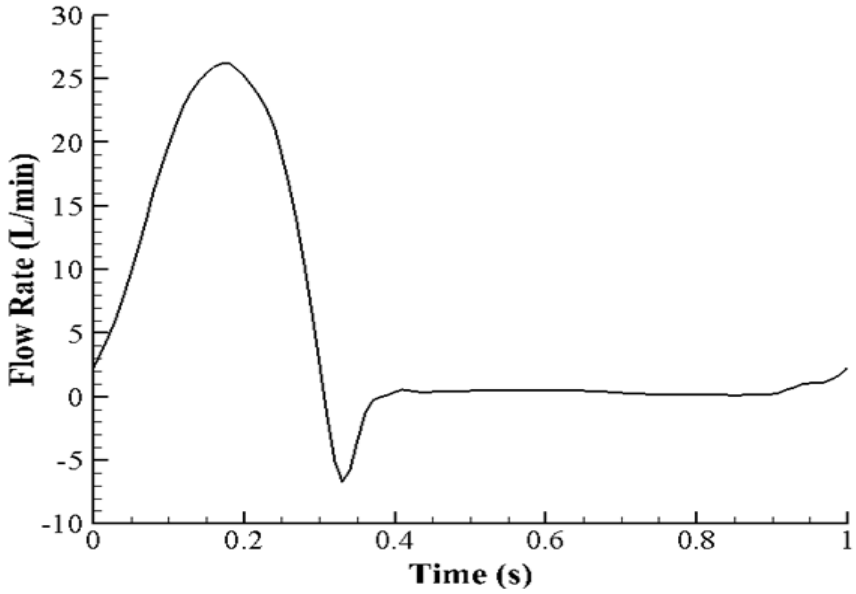

Figure 5.3: Sutureless aortic valve flow waveform
The flow-loop-generated experimental aortic flow curve for the ATS 3F Enable sutureless valve is presented for one cardiac cycle

5.3 Transcatheter Aortic Valve Implantation (TAVI)

For the TAVI sinus cases, particle streak plots were once again created from PIV images. Videos of these particle streaks are included for one complete cardiac cycle for native non-coronary, native coronary, TAVI non-coronary, and TAVI coronary cases in Figure 5.4. Still-frame snapshots from these videos are shown in Figure 5.5. Note that these snapshots include

manually-drawn arrows, not computed vectors, as a means to help explain the flow patterns present in the videos. Results for the native valve control case, which are presented in Specific Aim 2, are also presented and explained here for ease of comparison.

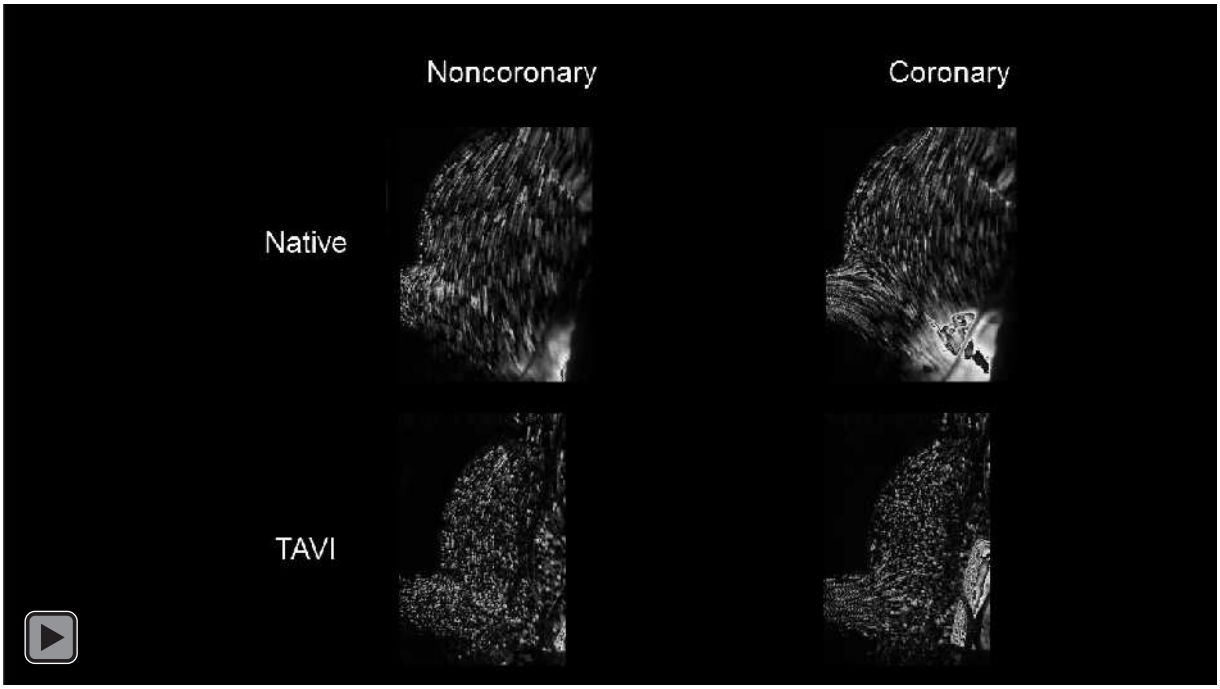

Figure 5.4: TAVI study streak plot video
Qualitative streak plots within the sinus were created for the case of a TAVI valve with and without coronary flow. Native valve non-coronary and coronary streaks plots are also included for comparison.

5.3.1 Qualitative Results

Figure 5.5a shows annotated snapshots from sinus streak plots for the native non-coronary sinus while Figure 5.5b shows streak plot images for the native coronary sinus. During early systole, sinus flow velocity is generally high and there is much streamwise flow in each of these cases. There appears to be a stagnation point near the downstream end of the sinus wall, where flow is either diverted towards the sinotubular junction or recirculated back into the sinus. This point is slightly farther upstream in the coronary sinus and migrates downstream in both cases as systole progresses. At mid systole, there is flow from the back of the sinus that is

drawn into the coronary artery which is not present in the non-coronary sinus. Near the end of systole, the sinus vortex has grown, however flow velocity is significantly reduced. During diastole, sinus flow velocities are much lower. There is a pattern of flow toward the base of the sinus at early diastole, but by mid diastole flow is relatively stagnant. In the coronary sinus, early and mid diastole display particle motion that is mainly toward the ostium, with this pattern being stronger and more widespread throughout the sinus toward mid diastole.

The introduction of a TAVI valve greatly alters sinus hemodynamics (Figure 5.5c) compared to those of the native valve. There is little to no streamwise flow within the sinus during early systole, however a small vortex is shed off the leaflet tip. This vortex grows in size and starts to fill more of the sinus as systole progresses. However, flow speed is much lower with the introduction of a TAVI valve for these portions of systole. Diastolic hemodynamics are similar with or without a TAVI valve. There is still some flow from the sinotubular junction towards the sinus base during early diastole and still very little, yet unpredictable, fluid motion during mid diastole.

Coronary flow in the presence of a TAVI valve causes some changes in sinus hemodynamics from the non-coronary TAVI case (Figure 5.5d). During the early stages of systole, the sinus vortex covers much more of the sinus. However, flow does not recirculate completely but rather exits the sinus at the coronary ostium. Additionally, there is some entrainment of fluid from the base of the sinus from coronary flow. Toward the end of systole, there is no noticeable sinus vortex as most particle motion is toward the ostium. Similarly, both early and mid-diastolic hemodynamics show a dominant pattern of flow from all parts of the sinus toward the coronary ostium, with somewhat higher velocities during mid diastole.

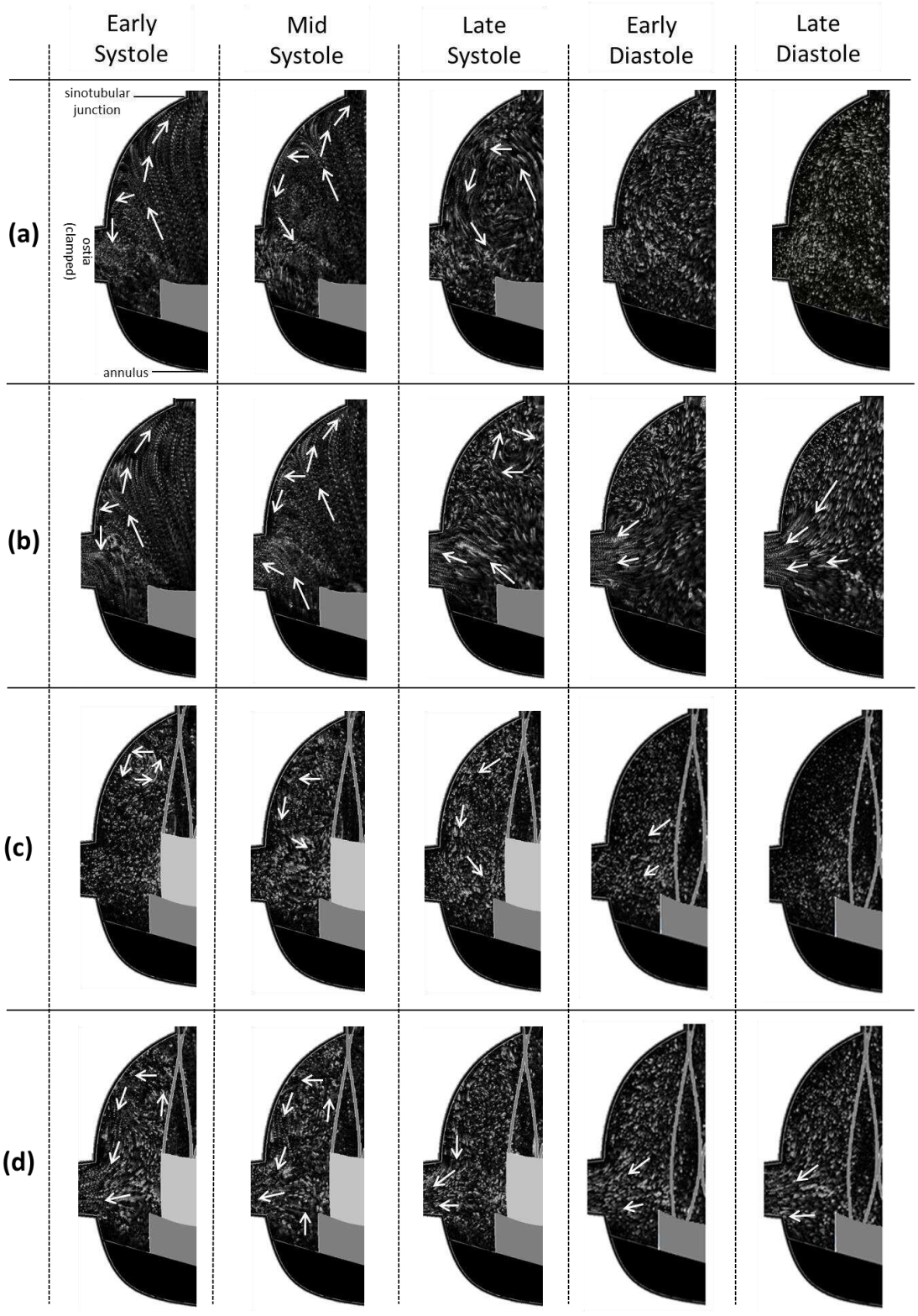

Figure 5.5: TAVI study streak plot snapshots
Snapshots from qualitative streak plot videos for a) native non-coronary, b) native coronary, c) TAVI non-coronary, and d) TAVI coronary sinuses are presented with manually-added annotations to help explain flow features in the videos.

5.3.2 Quantitative Results

While qualitative streak plots are a useful tool for quickly and easily examining overall flow patterns, quantitative vector and contour maps provide more precise and detailed information on sinus flow parameters. Therefore, velocity vectors and vorticity contours are presented at select time-points of interest in Figure 5.6.

In the native valve control cases (Figure 5.6a and b), the presence of the sinus vortex is clear as soon as the early stages of systole. The center of this vortex is just downstream of the leaflet tip, in between the edge of the leaflet and the sinus wall. There is also significant freestream flow that enters the sinus, with velocities around 1.3 m/s and peak vorticity magnitude around 800 s^{-1}. Most of this is diverted into the aorta by the curvature of the downstream sinus wall while a small portion is redirected back toward the base of the sinus. At mid systole, the sinus vortex is still clearly distinguished but has migrated slightly downstream. This leads to the formation of a pocket of quiescent fluid near the annulus, which is entrained into the ostia in the coronary case. Vorticity magnitude is greatest at this time point, with a peak around 1000 s^{-1} and vortex velocities on the order of 0.7 m/s. Late systole yields a reduction in overall sinus velocity and therefore vorticity magnitude. However a weakened sinus vortex is still present, which is the dominant sinus flow pattern as most streamwise flow no longer exists within the sinus. There is a small amount of counterclockwise fluid motion during early diastole, but this is mostly gone as little flow exists during mid diastole. In the coronary sinus, the main velocity and vorticity during diastole exist near the ostium.

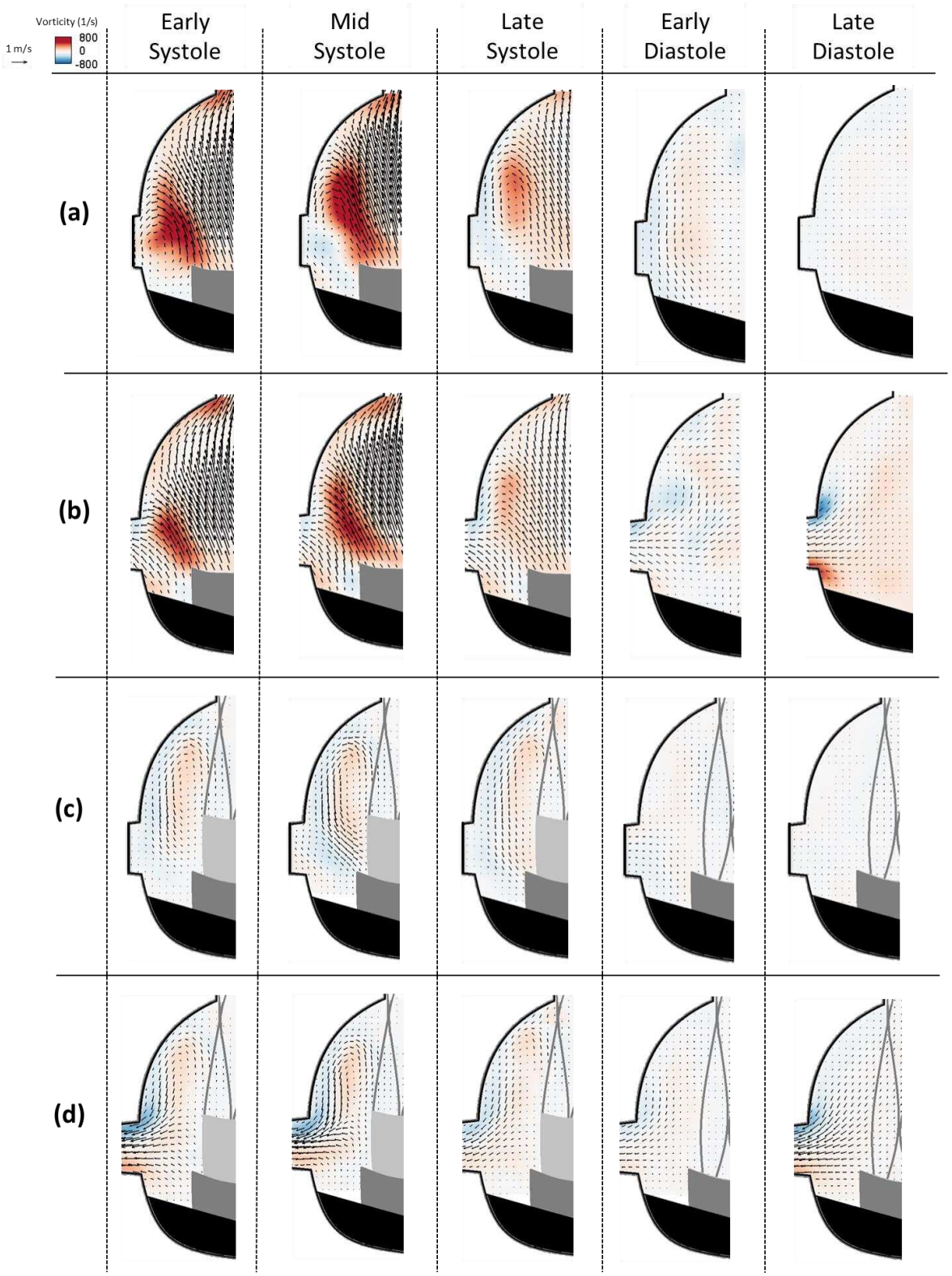

Figure 5.6: TAVI study velocity vectors and vorticity contours
Qualitative results are presented for a) native non-coronary, b) native coronary, c) TAVI non-coronary, and d) TAVI coronary sinuses at five time points throughout the cardiac cycle

The introduction of a TAVI valve causes numerous changes in sinus hemodynamics (Figure 5.6c). The most dramatic difference in the TAVI valve case, in comparison to the native valve case, is a reduction in overall velocity and voriticity, which becomes noticeable during early systole. Also, the less noticeable sinus vortex is positioned more downstream in the TAVI sinus than in the native sinus. At mid systole, the sinus vortex size is relatively unchanged as it stretches from the sinotubular junction to the tip of the native leaflet. Vorticity magnitude also remains similar to that during early systole, with a peak around 550 s^{-1}. Velocity magnitude is reduced relative to the native sinus, with highest systolic values around 0.4 m/s. Near the end of systole, there is only a small amount of counterclockwise motion, and fluid in the sinus is relatively stagnant throughout diastole.

Velocity and vorticity were also calculated for the coronary sinus in the presence of a TAVI valve (Figure 5.6d). In this case, the sinus vortex plays much less of a role. For instance, at early systole the highest velocity and vorticity magnitude occur due to flow entering the coronary ostium, with velocity magnitude in this region around 0.3 m/s. Around mid systole, hemodynamics are not significantly changed, however there is stronger recirculation around the downstream sinus wall and some entrainment of fluid into the ostium is apparent. Once freestream velocity has slowed, towards the end of systole, there is only a weak recirculating flow pattern present and a relatively small amount of coronary perfusion. Coronary flow is still low during early diastole but increases by mid diastole, reaching velocities near 0.4 m/s. There is otherwise very little motion in the sinus throughout diastole.

5.3.3 Shear Stress Results

Shear stress was calculated at the given time points of interest for each valve case. Results are presented as contour maps in Figure 5.7. These contours give an indication of the order of

magnitude of shear stresses in the sinus. The sub-region near the leaflet is of particular interest since leaflet wall shear stress is strongly linked to calcification [127].

Native valve sinus shear stress patterns are displayed in Figure 5.7a and b. During early systole, most of the sinus is dominated by large magnitude negative shear stress, over 1 Pa magnitude, in the downstream end of the sinus. However, there is also a significant region of strong positive shear near the leaflet free edge, which extends to the aortic side of the leaflet in the coronary case. Peak shear stress magnitudes near the aortic side of the leaflet are approximately 0.24 and 0.84 Pa in the non-coronary and coronary sinuses, respectively. During diastole, significant shear stress only exists near the edges of the ostium in the coronary sinus.

When a TAVI valve is implanted, sinus shear stress levels are generally reduced compared to the native valve cases (Figure 5.7c). During systole, two distinct shear regions are noticeable: one negative region along the aortic side of the TAVI leaflet and another positive region along the sinus wall. Stress magnitude in these regions increases during mid systole and then decreases dramatically during late systole. There is very little shear stress in the sinus throughout diastole for the TAVI non-coronary case.

Shear stresses for the TAVI coronary sinus case are presented in Figure 5.7d. In this case, there is higher magnitude shear stress near the leaflet tip and the ostium than in the non-coronary sinus. Peak shear magnitude near the aortic side of the leaflet reaches 0.7 Pa in the non-coronary sinus and 1.1 Pa in the coronary sinus. Additionally, stress magnitude in this region is much greater throughout diastole when coronary flow is present.

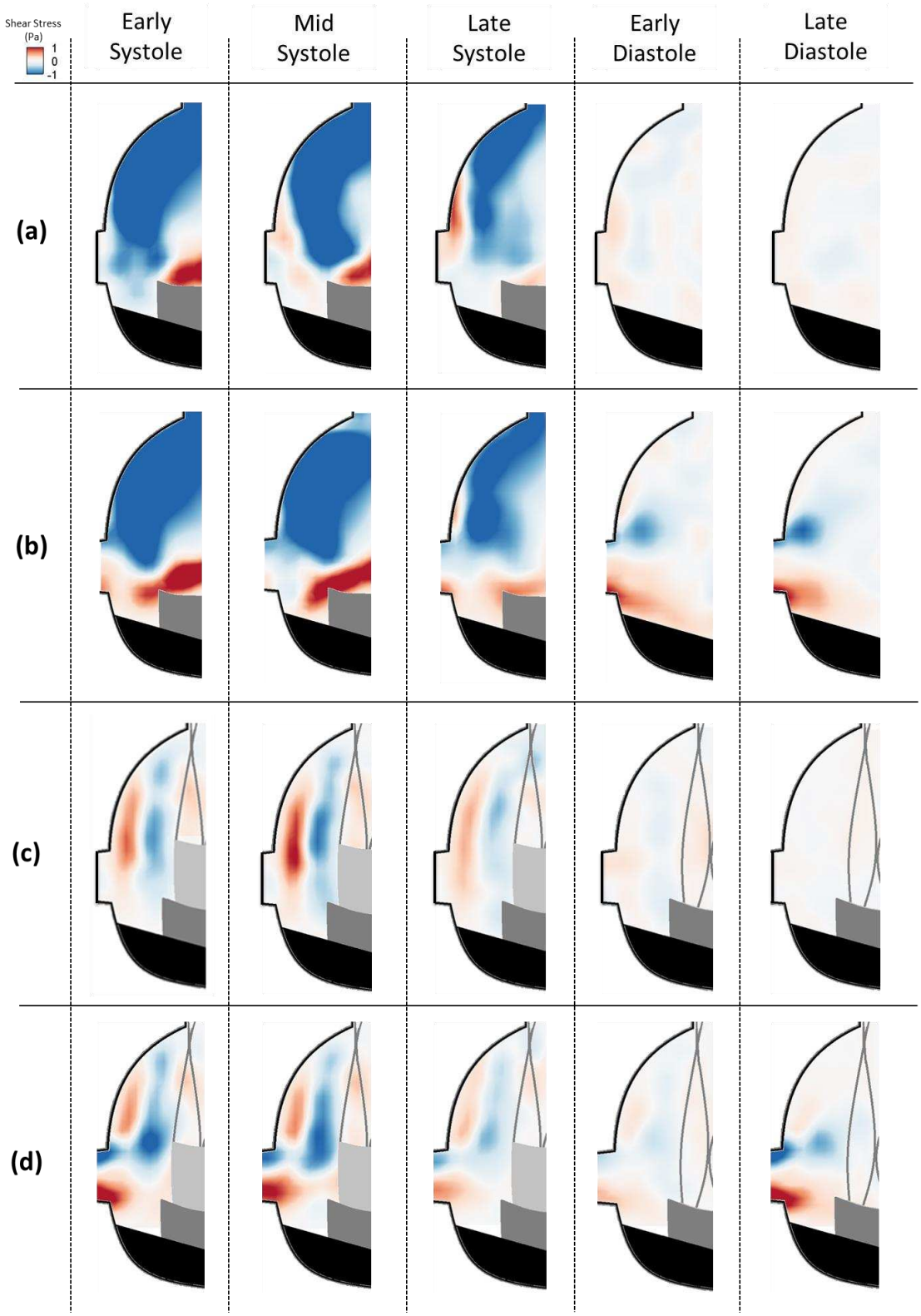

Figure 5.7: TAVI study fluid shear stress contours
Fluid stress contours are presented within the a) native non-coronary, b) native coronary, c) TAVI non-coronary, and d) TAVI coronary sinuses

5.3.4 Leaflet Kinematics

Leaflet tip position was manually tracked and its distance from the aortic axis was then calculated for each case of coronary and non-coronary sinus, with and without a TAVI valve. As seen in Figure 5.8, radial distance was significantly greater for the native valve cases since there was no stent present to restrict leaflet opening. Furthermore, the native coronary leaflet opened farther than the native non-coronary leaflet. From the initial fully open time point (~10% systolic duration) to start of closure (~85% systolic duration) the coronary leaflet opened an average of 5% farther into the sinus than the non-coronary leaflet in the native valve case. When comparing the two TAVI cases, both display the same flat profile due to restriction from the stent. This resulted in approximately an 8% difference in TAVI leaflet radial position from the native non-coronary leaflet and a 12% difference from the native coronary leaflet.

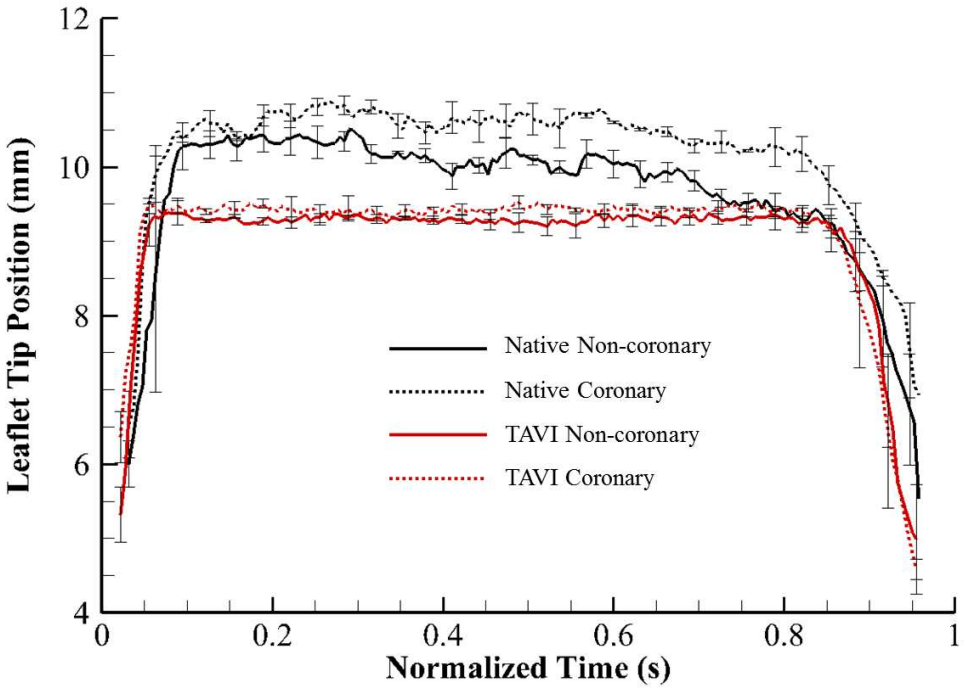

Figure 5.8: TAVI study leaflet kinematics
Radial distance from aortic axis to leaflet tip is plotted over systole for native and TAVI valve sinuses with and without coronary flow.

5.3.5 Discussion

Coronary Flow Waveforms

Coronary flow rate in vivo peaks during diastole with a smaller local peak occurring during systole [109, 111]. Our custom in vitro setup was tuned to mirror these coronary flow trends while maintaining physiological flow rate and pressures across the valve. There were slight differences in coronary flow magnitude between the native valve case and the TAVI case, specifically during systole. During this phase, flow was lower for the TAVI case. This could be due to lowered pressure within the sinus, which may have been caused by a higher pressure drop across the narrower TAVI valve.

TAVI Hemodynamic Effects

Examination of detailed sinus flow patterns in the presence of a TAVI valve yields numerous differences from the native valve case. In the native valve, for example, the systolic sinus vortex develops in the upstream portion of the sinus and then migrates downstream as systole progresses. In contrast, the TAVI sinus vortex encompasses nearly the entire downstream half of the sinus throughout systole. However, the TAVI vortex is much weaker overall than the native vortex.

The differing vorticity dynamics between these two valve cases are regulated largely by leaflet kinematics. When no TAVI valve is present, the leaflet tip opens into the sinus during early systole. In the presence of a TAVI valve, on the other hand, the leaflet extends farther downstream and is restricted from opening completely by the stent frame. The extended length of the TAVI leaflet is likely the reason for the downstream location at which the vortex develops, while the constant vortex topology is due to the static leaflet location.

The vortex topology is also due to viscous effects as well as geometry. These effects and their impact on vortex formation and development are explained for general sinus flow by Yap et al

[102]. To summarize their description, there are two possible methods of vortex formation within a sinus: 1) by some of the freestream flow entering the sinus or 2) by shear force interaction between sinus fluid and the freestream flow. In the present study, it appears that 1) is responsible for the native sinus vortex and 2) is responsible for the TAVI sinus vortex. This means that no freestream flow enters the sinus in the TAVI case, which could be due to the extension of the leaflet, the restriction of leaflet opening by the stent, by the stent itself, or by a combination of these factors. Regardless of the cause, the absence of freestream flow in the TAVI sinus leads to a much weaker vortex, with shear force being the sole contributing factor behind vortex formation. Additionally, some quiescent fluid near the native valve leaflet is entrained by the vortex, thus increasing overall fluid motion from early to mid systole.

Altered vorticity dynamics due to the introduction of a TAVI valve could have implications for disease. This is mainly due to the low magnitude and downstream location of the TAVI sinus vortex. Low magnitude means low blood velocity and therefore low shear stress along the leaflet – a factor that is strongly linked to calcification [113, 119]. Likewise, a downstream vortex that only slightly reaches the base of the sinus leaves a pocket of nearly stagnant fluid for much of the cardiac cycle. This particular finding is in agreement with results from a study by Ducci et al [53]. Such stagnation zones are often associated with thrombosis, which could explain an increased risk of stroke for TAVI patients [46, 47].

TAVI Hemodynamic Effects in a Coronary Sinus

Most alterations in hemodynamics brought about by TAVI implantation occur in both non-coronary and coronary sinuses. However, some hemodynamic changes are unique to the coronary sinus. For example, vortex flow in the TAVI coronary sinus is greatly reduced while coronary perfusion remains nearly unchanged. Therefore, flow into the ostium represents a

much larger portion of fluid movement in the sinus. Furthermore, this added flow could help alleviate thrombosis risk in the coronary sinus of TAVI patients.

Shear Stress

Leaflet wall shear stress is often of interest in aortic valve studies due to its correlation to calcification. While no wall shear stress was calculated in this study, fluid shear stress within the sinus was indeed calculated and is still of value since it demonstrates the magnitude of shear near the leaflet at different times during the cardiac cycle.

Coronary presence alone alters some sinus shear stress patterns in the native valve case. One of the areas of interest where differences exist is near the leaflet. This area is of interest because valvular calcification on the fibrosa side of the leaflet is strongly tied to shear stress. When examining this region in both cases, it is apparent from Figure 5.9a that there is higher magnitude shear for the coronary sinus. Additionally, shear stress direction is constant for the coronary case while it changes direction for the non-coronary case. Both of these trends have implications for disease since reduced and oscillatory shear stresses are correlated to development of calcification [120]. Therefore, the non-coronary sinus appears hemodynamically more susceptible to disease than the coronary sinus, which is supported by clinical findings that show earlier and more frequent signs of calcification on the non-coronary leaflet [2].

Effects of a TAVI valve on shear stress in the sinus are quite evident throughout systole when viewing the contour maps presented in Figure 5.7. The most noticeable trend is much lower magnitude shear overall for the TAVI valve cases. This is due in large part to the fact that free stream flow enters the sinus in the native but not in the TAVI sinuses. Such a large reduction in shear could lead to further calcification of the native leaflets.

Coronary presence significantly increases sinus shear stresses in the TAVI sinus throughout the cardiac cycle, most notably along the aortic side of the leaflet as shown in Figure 5.9b. This could be caused by a low pressure region near the ostium that helps pull the vortex toward the upstream end of the sinus. Low ostial pressure also produces some shear stress in the base of the sinus from entrainment of stagnant flow into the ostium from this region.

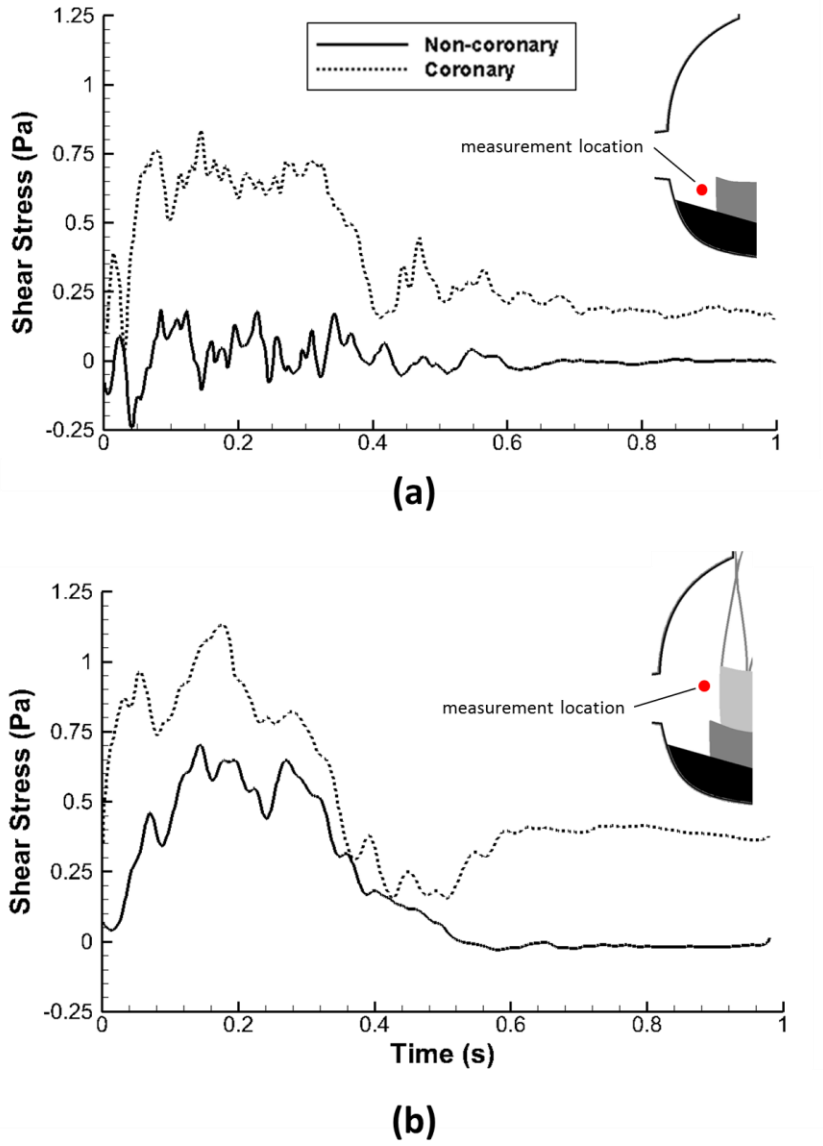

Figure 5.9: Time-varying fluid shear stress for TAVI study
Fluid shear stresses were calculated near the leaflet fibrosa for cases with and without coronary flow. These stresses are plotted vs time over one cardiac cycle for the a) native valve and b) TAVI valve

Leaflet Kinematics

The coronary leaflet is shown in Figure 5.8 to open farther into the sinus than the non-coronary leaflet. This is most likely due a lower sinus pressure, which is caused by the coronary ostium providing an alternate path for high pressure fluid in the sinus during systole. Da Vinci first hypothesized that the sinus vortex helped aid in leaflet closure, and recent studies have demonstrated how lowered pressure in the sinus could aid in leaflet opening [11, 121]. An additional lowering of pressure in the coronary sinus could further facilitate leaflet opening.

Application to Valve-in-Valve Situation

The bioprosthesis used in this study is modeled as a native valve due to the manner in which it meshes with the acrylic valve chamber. In this way, the leaflets alone are exposed to the fluid while the stent frame is hidden by recesses in the chamber walls that have matching dimensions. However, a CoreValve inside of a Hancock bioprosthesis also clinically represents a valve-in-valve situation. While the surgical aortic valve replacement (SAVR) stent frame may have a lower profile, the in vivo interaction between the SAVR and TAVI valves is preserved. Therefore, it is expected that changes in hemodynamics and leaflet kinematics resulting from TAVI implantation in this study will occur in both valve-in-valve and TAVI-in-native-valve scenarios.

5.3.6 Limitations

A few major limitations were present in this study. First of all, the use of a rigid sinus chamber is not physiologically accurate. However, this simplification has been employed in previous studies due to the fact that wall motion is very small compared to leaflet displacement. Moreover, the aortic root of most TAVI patients is calcified and therefore more rigid than the healthy root. Additionally, while there is three dimensional flow in the sinus, we were only able

to capture a two dimensional slice. Last of all, there was a small amount of signal loss due to blockage of the laser sheet by the coronary tubing adapter, but this was limited to a small sliver in the base of the sinus.

5.4 Sutureless Aortic Valve Implantation

An ATS 3F Enable sutureless valve was tested inside a custom valve chamber. A video of particle streak paths is shown in Figure 5.10.

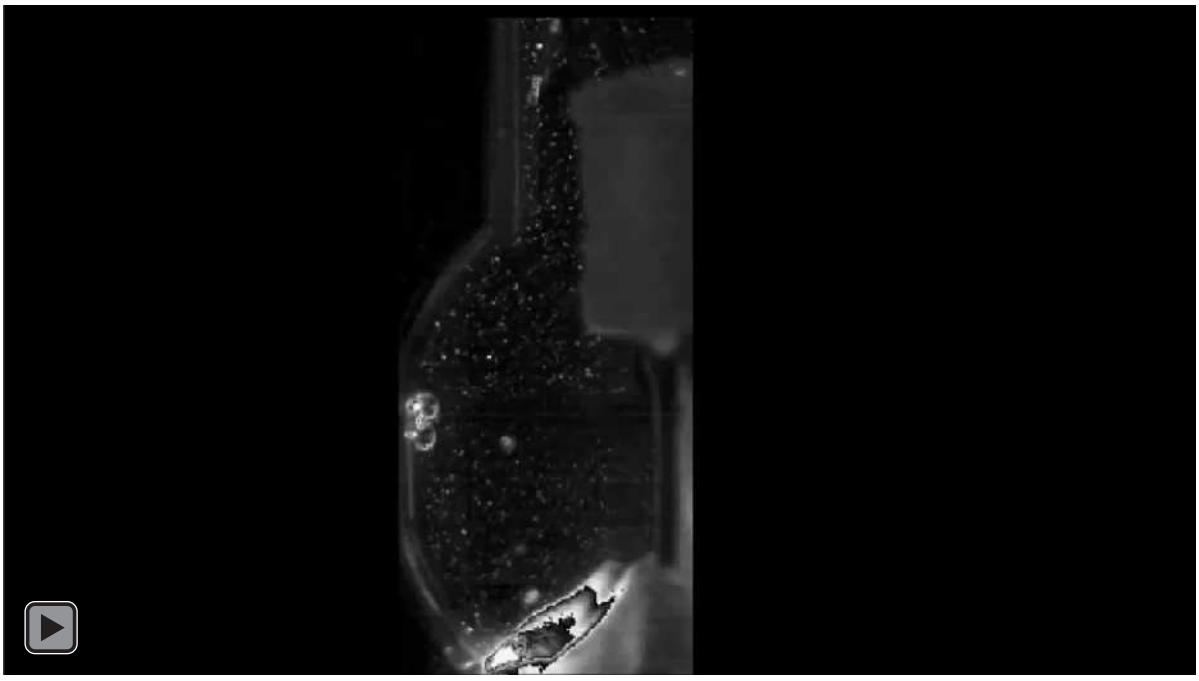

Figure 5.10: Sutureless valve study streak plot video
A qualitative streak path video is shown for an ATS 3F Enable sutureless valve inside a custom chamber.

5.4.1 Qualitative Results

Annotated snapshots are included in Figure 5.11. Overall, there is very little fluid motion within the sinus for this valve case compared to others tested. At early systole, there is a small vortex that appears to form off of the leaflet free edge. This vortex is positioned in close proximity to the sinotubular junction and quickly disappears as systole progresses. By mid systole, there is

still some fluid movement near the edge of the leaflet and sinotubular junction, and most of this motion is in the streamwise direction. Some recirculating flow is apparent in this same region during late systole as flow begins to decelerate and the leaflet begins to close. The most notable sinus velocities are present during valve closure. As this takes place, particles follow the contour of the sinus wall and therefore move in a counterclockwise manner from the sinotubular junction toward the annulus. Once the valve is fully closed, there is very little particle motion within the sinus throughout diastole.

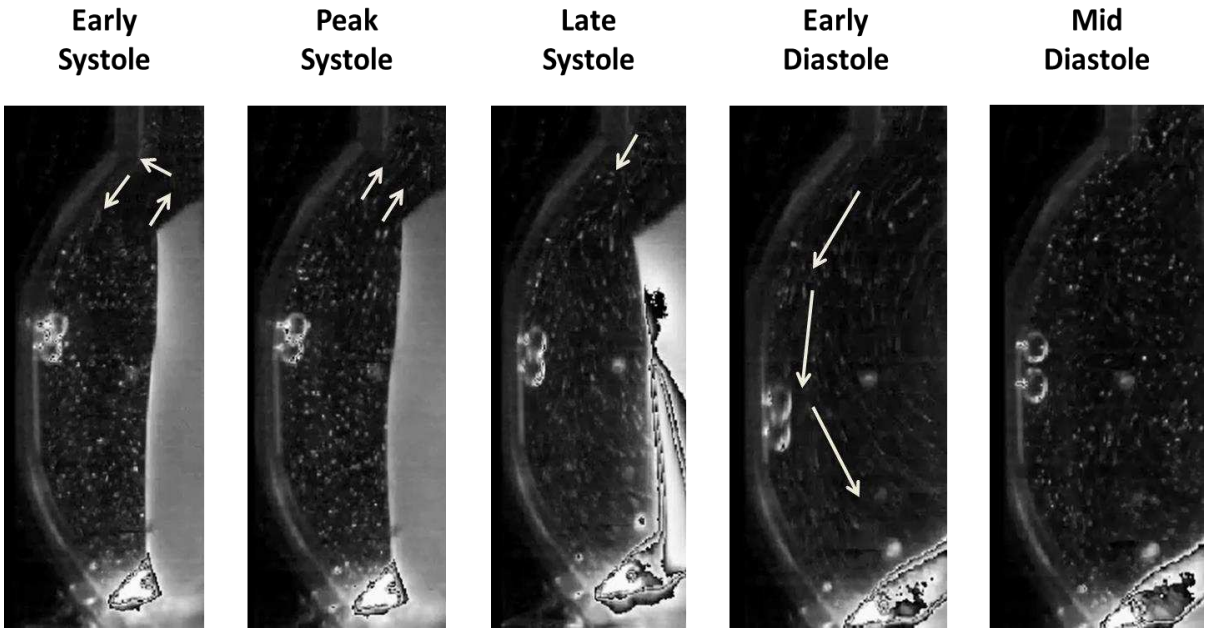

Figure 5.11: Sutureless valve study streak plot snapshots
Annotated snapshots from qualitative streak video of the ATS 3F Enable valve are presented at discrete time points across one cardiac cycle

5.4.2 Quantitative Results

Quantitative results are shown in Figure 5.12. These images reflect the flow trends that are present in the qualitative streak video. At early systole, there is a small vortex present between the leaflet free edge and the sinotubular junction, with a magnitude around 200 s^{-1}. A shear layer is also visible near the aortic wall at this time point. During the later systolic stages, there

is very little sinus motion, aside from a small amount of entrained fluid near the sinotubular junction into the free stream flow. The highest magnitudes of velocity and vorticity within the sinus occur as the valve is closing. During this phase, there is some regurgitation that leads to backward flow within the sinus. This flow moves in a somewhat counterclockwise pattern, thus leading to a region of positive vorticity near the leaflet. However, this flow quickly dissipates and fluid is relatively stagnant in the sinus by mid diastole.

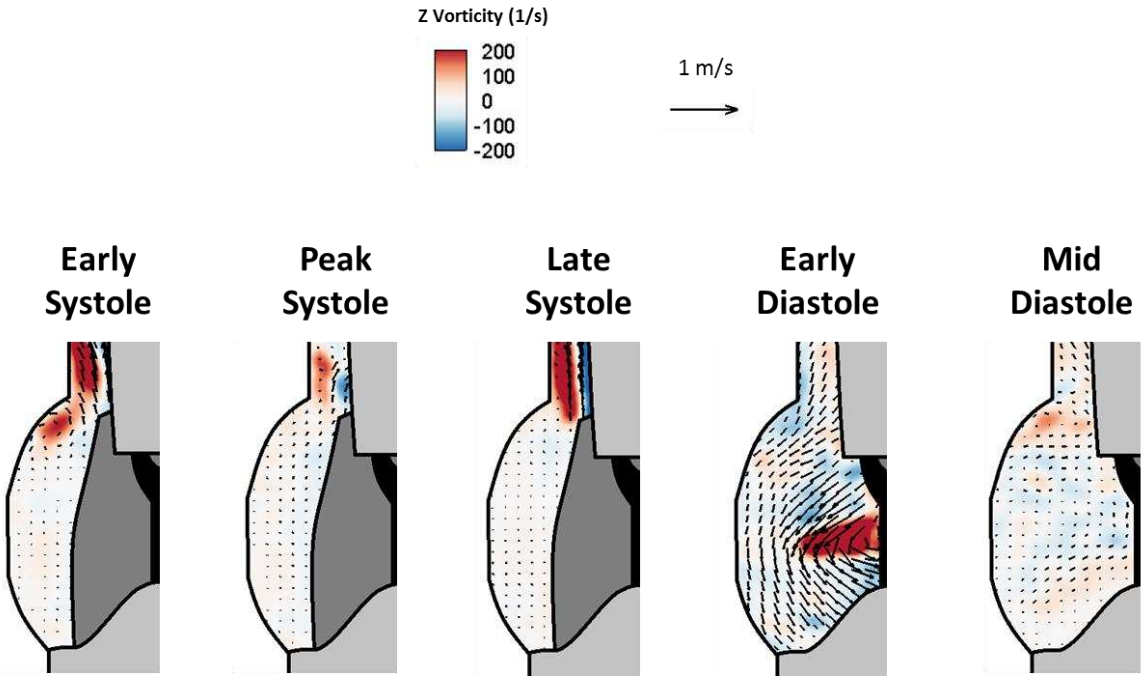

Figure 5.12: Sutureless valve study velocity vectors and vorticity contours
Quantitative results for the ATS 3F Enable sutureless valve are presented at five time points throughout the cardiac cycle

5.4.3 Discussion

The early vortex that is formed appears to be shed off of the leaflet tip, mainly during valve opening. This vortex is entrained into the free stream flow relatively quickly without influencing any fluid in the rest of the sinus. This entrainment appears to continue into peak systole as some fluid in the downstream end of the sinus is pulled into the free stream jet. Fluid movement

toward the valve occurs during early diastole as the valve is closing, likely due to regurgitant flow and a suction effect created by the moving leaflets.

Overall low sinus velocities and vorticities are likely due to the length of the valve in the streamwise direction. Sinus dimensions of the valve chamber used are on the upper end of the physiological range and were chosen in order to fit the sutureless valve. Therefore, this scenario likely represents the largest sinus size in which this particular valve would be implanted. In this study, sinus flow is stagnant, which appears to be caused by the sutureless leaflets extending too far downstream and blocking flow into the sinuses. Since a relatively large sinus model was used, this likely represents the best case scenario for sinus perfusion, so other cases would have even less flow in the sinuses.

5.4.4 Limitations

One limitation of this study is the rigid valve chamber that was used. Since this sutureless valve is designed to be secured in place by radial stent forces, a more realistic compliant aortic root model would likely yield valve dynamics more representative of those in vivo. This could be one explanation for the discrepancy in regurgitation between this study and previous in vivo studies. There was moderate regurgitation in this in vitro model while this parameter was mild to non-existent in clinical trials [128].

5.5 Chapter Summary

Two types of prosthetic valves were tested in addition to the model native valve. These were a Medtronic CoreValve transcatheter aortic valve implantation (TAVI) and an ATS 3F Enable sutureless bioprosthesis. Experimental results from both of these studies show greatly reduced velocity and vorticity within the sinuses relative to the native valve case. This is most likely due

to the geometry of these prosthetic valves. In particular, the leaflets extend farther downstream than the native leaflets and therefore limit the area for flow to enter the sinuses. Additionally, stent geometry for each valve limits radial leaflet opening, which could contribute to reduced sinus flow velocities.

For the TAVI valve, although the sinus vortex was weaker, it did encompass more of the sinus than the native vortex. Also, due to these reduced sinus velocities, the introduction of coronary flow into the TAVI sinus had a larger relative impact on vorticity dynamics than for the native valve case. This was especially true for fluid in the base of the sinus. At this location, flow was greatly enhanced and there was a corresponding increase in fluid shear stress magnitude when coronary flow was present.

Fluid motion in the sinus for the sutureless valve case was reduced even more than in the TAVI valve case. There was little to no vortex motion in the sutureless sinus, with the only evidence of this structure apparent between the leaflet free edge and sinotubular junction at early systole. Valve closure also brought about some sinus fluid movement, but only for limited time duration. Overall, it appears that these types of prosthetic valves could have negative impacts on valve health due to reduced fluid motion in the sinuses.

6. SUMMARY AND FUTURE WORK

6.1 Overall Summary

The aortic valve functions in a complex mechanical environment and even slight changes to these mechanics can have serious implications for valve health. In particular, hemodynamics on the aortic side of the leaflets regulate valve health because this is most often the site of disease development. Flow in this region is highly unsteady and is dictated by anatomic valve conditions and bulk hemodynamics, so a parametric study has been conducted to evaluate the impacts on sinus flow from a range of anatomic and hemodynamic parameters.

Both experimental and computational methods have been developed to study sinus hemodynamics. Multiple flow loop variations were created for in vitro valve testing and particle image velocimetry protocols were followed to visualize hemodynamics within these setups. These PIV results yielded high spatiotemporal resolution and demonstrated novel sinus flow patterns. Additionally, 2D and 3D computational fluid dynamics models were created and used to run simulations in ANSYS Fluent. Results from CFD simulations were comparable to experiments and gave further insight into aortic valve sinus hemodynamic. Both experimental and computational results were analyzed using Tecplot software.

It was found that sinus hemodynamics can change drastically depending on the specific valve conditions. In this study, the largest changes in hemodynamics occur due to prosthetic valve implantation, however normal variance in anatomy as well as differences between coronary and non-coronary sinus still have significant impacts. The prosthetic valves tested – a TAVI valve and a sutureless valve – both impeded sinus flow and therefore demonstrate adverse mechanics from a clinical standpoint. Tests across a range of anatomic and physiologic

parameters – such as sinus size, coronary ostium location and flow rate, heart rate, and aortic flow waveform shape – suggest that there are ideal anatomic and physiologic conditions that generally correspond to an average in vivo valve. Known pathological conditions, such as elevated heart rate or reduced coronary flow, caused negative alterations to sinus hemodynamics which give insight into the mechanisms of disease. Also, the effects of coronary flow on the sinus vorticity landscape have been elucidated and provide support for the notion that calcification develops earlier on the non-coronary cusp.

This study employed a tandem experimental-computational approach. Computational simulations did not always exactly match experimental results, but many common flow patterns exist. Also, differences introduced by certain anatomic and physiological parameters are similar experimentally compared to computationally. Therefore, while the computational methods developed here may not yield perfectly accurate results when used as a standalone tool, simulations do provide some realistic insight into sinus hemodynamics that are more easily obtained than through experimentation. This is because simulations can be adapted to test different parameters much more easily than experiments can and they can also yield 3D information that is not obtainable from PIV.

6.2 Future Work

There are a number of limitations associated with this work, which can be addressed through refinement of current studies and/or development of additional methodologies. For example, the rigid valve chambers used to mimic the aortic root in this work can instead be fabricated with compliant materials, such as silicone, that better model the material properties of aortic tissue. Another experimental limitation is the 2D nature of the PIV methodology. To enhance these experiments, 3D PIV can be employed. While this method is still being refined and therefore lacks spatial and temporal resolution, 3D PIV would still be useful to give insight into

hemodynamics throughout the entire valve model rather than just at a planar slice. The major limitation computationally is a lack of leaflet motion. Development of a fluid-structure interaction (FSI) model in the future would greatly improve simulation capabilities and give additional information regarding structural leaflet stresses. Finally, the modeling framework developed here can be used to assist in the design and testing of novel aortic valves to overcome the limitations of currently available prosthetic valves.

Despite computational limitations, CFD simulations still gave insight that was not possible with experiments only. Since it is generally easier to modify these computational models than corresponding experimental models, simulations could be used in the future to drive experimental work. Numerous CFD models could be created and those yielding unique or interesting flow patterns could then be further explored experimentally.

7. FIELD CONTRIBUTIONS

7.1 Peer-Reviewed Journal Publications

B. Moore and L. P. Dasi, “Coronary Flow Impacts Aortic Leaflet Mechanics and Aortic Sinus Hemodynamics”, Annals of Biomedical Engineering, 2015.

B. Moore and L.P. Dasi, “Spatiotemporal complexity of the aortic sinus vortex”, Experiments in Fluids, 2014. 55(7).

B. Moore and L.P. Dasi, “Multi-fractal nature of human left ventricular trabeculae: Possible biomechanical role?”, Chaos Solitons & Fractals, 2013. 57: p. 19-23.

B. Moore and L.P. Dasi, “Quantifying left ventricular trabeculae function - application of image-based fractal analysis”, Physiol Rep, 2013. 1(4): p. e00068.

B. Moore, P. Maureira, and L. P. Dasi, “Effects of Transcatheter Aortic Valve Implantation on Sinus Hemodynamics with and without Coronary Flow”, 2015. (submitted)

7.2 Conference Publications

B. Moore, P. Maureira, and L. P. Dasi, “Effects of Coronary Flow on Sinus Hemodynamics in the Presence of a Transcatheter Aortic Valve Implantation”, Summer Biomechanics, Bioengineering and Biotransport Conference, Snowbird, Utah, 2015.

B. Moore and L. P. Dasi, “Aortic Flow Waveform Shape Regulates Valvular Hemodynamics and Energy Losses”, Summer Biomechanics, Bioengineering and Biotransport Conference, Snowbird, Utah, 2015.

B. Zebhi, B. Moore, G. J. Luckasen, L. P. Dasi, “Aortic Valve Calcification: Geometric and Biomechanical Analysis”, Summer Biomechanics, Bioengineering and Biotransport Conference, Snowbird, Utah, 2015.

A. Y. Koupaei, B. Moore, D. Bark, L. P. Dasi, “Analyzing the Effects of Stent Geometry for Polymeric Aortic Valves”, Summer Biomechanics, Bioengineering and Biotransport Conference, Snowbird, Utah, 2015.

B. Moore, R. Simon-Walker, P. Maureira, L. P. Dasi, “Effect of Coronary Flow and Implications of Trans-Catheter Aortic Valve Implantation on Sinus Flow”, World Conference of Biomechanics, Boston, Massachusetts, 2014.

B. Moore and L. P. Dasi, “Aortic Valve Sinus Vorticity Dynamics and the Potential Role of Coronary Flow”, American Society of Mechanical Engineering – Summer Bioengineering Conference, Sunriver, Oregon, 2013.

B. Moore and L. P. Dasi. Is the human left ventricle partially a fractal pump? American Physical Society – Division of Fluid Dynamics, Baltimore, Maryland, 2011.

8. REFERENCES

1. Go, A.S., et al., *Heart Disease and Stroke Statistics-2014 Update A Report From the American Heart Association.* Circulation, 2014. **129**(3): p. E28-E292.

2. Freeman, R.V. and C.M. Otto, *Spectrum of calcific aortic valve disease - Pathogenesis, disease progression, and treatment strategies.* Circulation, 2005. **111**(24): p. 3316-3326.

3. Iaizzo, P.A., *Handbook of cardiac anatomy, physiology, and devices*. Current clinical oncology (Totowa, N.J.), ed. P.A. Iaizzo2005, Totowa, N.J.: Humana Press.

4. Kasel, A.M., et al., *Standardized imaging for aortic annular sizing: implications for transcatheter valve selection.* JACC: Cardiovascular Imaging, 2013. **6**(2): p. 249-262.

5. Gould, S.T., et al., *Hemodynamic and Cellular Response Feedback in Calcific Aortic Valve Disease.* Circulation Research, 2013. **113**(2): p. 186-197.

6. Ho, S.Y., *Structure and anatomy of the aortic root.* European journal of echocardiography, 2009. **10**(1): p. i3-i10.

7. Scott, M. and I. Vesely, *Aortic valve cusp microstructure: the role of elastin.* The annals of thoracic surgery, 1995. **60**: p. S391-S394.

8. Liao, J., E.M. Joyce, and M.S. Sacks, *Effects of decellularization on the mechanical and structural properties of the porcine aortic valve leaflet.* Biomaterials, 2008. **29**(8): p. 1065-1074.

9. Thubrikar, M.J., *The Aortic Valve*. 1st ed1990: CRC-Press.

10. *Wiggers diagram*. 2014; Available from: http://en.wikipedia.org/wiki/Wiggers_diagram.

11. Gharib, M., et al., *Leonardo's vision of flow visualization.* Experiments in Fluids, 2002. **33**(1): p. 219-223.

12. Reid, K., *The anatomy of the sinus of Valsalva.* Thorax, 1970. **25**(1): p. 79-85.

13. Lee, C.S.F. and L. Talbot, *A fluid-mechanical study of the closure of heart valves.* J. Fluid Mech., 1978. **91**(1): p. 41-63.

14. Peacock, J.A., *AN INVITRO STUDY OF THE ONSET OF TURBULENCE IN THE SINUS OF VALSALVA.* Circulation Research, 1990. **67**(2): p. 448-460.

15. Moore, B. and L.P. Dasi, *Spatiotemporal complexity of the aortic sinus vortex.* Experiments in Fluids, 2014. **55**(7).

16. Soulis, J., et al., *Wall shear stress oscillation and its gradient in the normal left coronary artery tree bifurcations.* Hippokratia, 2014. **18**(1): p. 12.

17. Otto, C.M., et al., *Characterization of the early lesion of'degenerative'valvular aortic stenosis. Histological and immunohistochemical studies.* Circulation, 1994. **90**(2): p. 844-853.

18. Hjortnaes, J., S.E.P. New, and E. Aikawa, *Visualizing novel concepts of cardiovascular calcification.* Trends in Cardiovascular Medicine, 2013. **23**(3): p. 71-79.

19. Yip, C.Y.Y. and C.A. Simmons, *The aortic valve microenvironment and its role in calcific aortic valve disease.* Cardiovascular Pathology, 2011. **20**(3): p. 177-182.

20. Lloyd, J., *Heart Disease and Stroke Statistics-2009 Update: A Report From the American Heart Association Statistics Committee and Stroke Statistics Subcommittee (vol 119, pg e21, 2009).* Circulation, 2011. **124**(16): p. E424-E424.

21. Novaro, G.M. *Aortic Valve Disease*. Center for Continuing Education; Available from: http://www.clevelandclinicmeded.com/medicalpubs/diseasemanagement/cardiology/aortic-valve-disease/Default.htm.

22. GL, H. and L. GV, *Aortic valve disease and hypertrophic cardiomyopathies*, 1996, Appleton & Lange: Connecticut.

23. Yener, N., et al., *Bicuspid aortic valve.* Annals of thoracic and cardiovascular surgery, 2002. **8**(5): p. 264-267.

24. Saikrishnan, N., L. Mirabella, and A.P. Yoganathan, *Bicuspid aortic valves are associated with increased wall and turbulence shear stress levels compared to trileaflet aortic valves.* Biomechanics and Modeling in Mechanobiology, 2014: p. 1-12.

25. Lee, H.-J., et al., *Anomalous Origin of the Right Coronary Artery from the Left Coronary Sinus with an Interarterial Course: Subtypes and Clinical Importance.* Radiology, 2012. **262**(1): p. 101-108.

26. Govsa, F., et al., *Anatomic variability of the coronary arterial orifices.* Anadolu Kardiyoloji Dergisi-the Anatolian Journal of Cardiology, 2010. **10**(1): p. 3-8.

27. Torigoe, T., et al., *Anomalous Origin of the Left Coronary Artery from the Proper Sinus with Acute Angulation and an Intramural Segment.* Congenital heart disease, 2014. **9**(1): p. E1-E5.

28. Latham, R.D., et al., *Regional wave travel and reflections along the human aorta: a study with six simultaneous micromanometric pressures.* Circulation, 1985. **72**(6): p. 1257-1269.

29. Mitchell, G.F., et al., *Changes in arterial stiffness and wave reflection with advancing age in healthy men and women the Framingham Heart Study.* Hypertension, 2004. **43**(6): p. 1239-1245.

30. Nichols, W., M. O'Rourke, and C. Vlachopoulos, *McDonald's blood flow in arteries: theoretical, experimental and clinical principles*2011: CRC Press.

31. Senthilnathan, V., et al., *Heart valves: which is the best choice?* Cardiovascular surgery, 1999. **7**(4): p. 393-397.

32. Vongpatanasin, W., L.D. Hillis, and R.A. Lange, *Prosthetic heart valves.* New England Journal of Medicine, 1996. **335**(6): p. 407-416.

33. Pibarot, P. and J. Dumesnil, *Valvular Heart Disease: Changing Concepts in Disease Management.* Circulation, 2009. **119**: p. 1034-1048.

34. Yankah, C.A., Y.-G. Weng, and R. Hetzer, *Aortic root surgery: the biological solution*2010: Springer Science & Business Media.

35. Weinberg, E.J., et al., *Hemodynamic Environments from Opposing Sides of Human Aortic Valve Leaflets Evoke Distinct Endothelial Phenotypes In Vitro.* Cardiovascular Engineering, 2010. **10**(1): p. 5-11.

36. Sucosky, P., et al., *Altered Shear Stress Stimulates Upregulation of Endothelial VCAM-1 and ICAM-1 in a BMP-4-and TGF-beta 1-Dependent Pathway.* Arteriosclerosis Thrombosis and Vascular Biology, 2009. **29**(2): p. 254-260.

37. Sun, L., N.M. Rajamannan, and P. Sucosky, *Design and Validation of a Novel Bioreactor to Subject Aortic Valve Leaflets to Side-Specific Shear Stress.* Ann Biomed Eng, 2011. **39**(8): p. 2174-2185.

38. Sun, L., S. Chandra, and P. Sucosky, *Ex Vivo Evidence for the Contribution of Hemodynamic Shear Stress Abnormalities to the Early Pathogenesis of Calcific Bicuspid Aortic Valve Disease.* Plos One, 2012. **7**(10).

39. Miller, J.D., R.M. Weiss, and D.D. Heistad, *Calcific Aortic Valve Stenosis: Methods, Models, and Mechanisms.* Circulation Research, 2011. **108**(11): p. 1392-1412.

40. Butcher, J.T. and R.M. Nerem, *Valvular endothelial cells and the mechanoregulation of valvular pathology.* Philosophical Transactions of the Royal Society B-Biological Sciences, 2007. **362**(1484): p. 1445-1457.

41. Balachandran, K., et al., *Elevated Cyclic Stretch Induces Aortic Valve Calcification in a Bone Morphogenic Protein-Dependent Manner.* American Journal of Pathology, 2010. **177**(1): p. 49-57.

42. Fisher, C.I., J. Chen, and W.D. Merryman, *Calcific nodule morphogenesis by heart valve interstitial cells is strain dependent.* Biomechanics and Modeling in Mechanobiology, 2013. **12**(1): p. 5-17.

43. Butcher, J., C. Simmons, and J. Warnock, *Mechanobiology of the aortic heart valve.* The Journal of heart valve disease, 2008. **17**(1): p. 62-73.

44. Beppu, S., et al., *Rapidity of progression of aortic stenosis in patients with congenital bicuspid aortic valves.* The American journal of cardiology, 1993. **71**(4): p. 322-327.

45. Roberts, W.C. and J.M. Ko, *Frequency by decades of unicuspid, bicuspid, and tricuspid aortic valves in adults having isolated aortic valve replacement for aortic stenosis, with or without associated aortic regurgitation.* Circulation, 2005. **111**(7): p. 920-925.

46. Smith, C.R., *Transcatheter versus surgical aortic-valve replacement in high-risk patients.* The New England journal of medicine, 2011. **364**(23): p. 2187.

47. Waksman, R. and S.a. Minha, *Stroke After Aortic Valve Replacement: The Known and Unknown.* Circulation, 2014. **129**(22): p. 2245-2247.

48. Groves, E., et al., *The Effects of Positioning of Transcatheter Aortic Valves on Fluid Dynamics of the Aortic Root.* ASAIO journal, 2014. **60**(5): p. 545-552.

49. Dvir, D., et al., *Transcatheter Aortic Valve Replacement for Degenerative Bioprosthetic Surgical Valves: Results From the Global Valve-in-Valve Registry.* Circulation, 2012. **126**(19): p. 2335-2344.

50. Saikrishnan, N., et al., *In Vitro Characterization of Bicuspid Aortic Valve Hemodynamics Using Particle Image Velocimetry.* Ann Biomed Eng, 2012. **40**(8): p. 1760-1775.

51. Bottio, T., et al., *Aortic Valve Hydrodynamics: Considerations on the Absence of Sinuses of Valvalsva.* The Journal of heart valve disease, 2012. **21**(6): p. 718-723.

52. Lim, W., et al., *Pulsatile flow studies of a porcine bioprosthetic aortic valve in vitro: PIV measurements and shear-induced blood damage.* J Biomech, 2001. **34**(11): p. 1417-1427.

53. Ducci, A., et al., *Hemodynamics in the Valsalva Sinuses after Transcatheter Aortic Valve Implantation (TAVI).* Journal of Heart Valve Disease, 2013. **22**(5): p. 688-696.

54. Gunning, P.S., et al., *An in vitro evaluation of the impact of eccentric deployment on transcatheter aortic valve hemodynamics.* Ann Biomed Eng, 2014. **42**(6): p. 1195-1206.

55. Yap, C.H., et al., *Experimental Technique of Measuring Dynamic Fluid Shear Stress on the Aortic Surface of the Aortic Valve Leaflet.* Journal of Biomechanical Engineering-Transactions of the Asme, 2011. **133**(6).

56. Yap, C.H., N. Saikrishnan, and A.P. Yoganathan, *Experimental measurement of dynamic fluid shear stress on the ventricular surface of the aortic valve leaflet.* Biomechanics and Modeling in Mechanobiology, 2012. **11**(1-2): p. 231-244.

57. Ge, L. and F. Sotiropoulos, *Direction and magnitude of blood flow shear stresses on the leaflets of aortic valves: is there a link with valve calcification?* Journal of Biomechanical Engineering, 2010. **132**(1): p. 014505.

58. Marn, J., et al., *Non-Newtonian Blood Flow around Healthy and Regurgitated Aortic Valve with Coronary Blood Flow Involved.* Strojniski Vestnik-Journal of Mechanical Engineering, 2012. **58**(7-8): p. 482-491.

59. Dwyer, H.A., et al., *Computational fluid dynamics simulation of transcatheter aortic valve degeneration.* Interactive cardiovascular and thoracic surgery, 2009. **9**(2): p. 301-308.

60. Marom, G., et al., *A fluid-structure interaction model of the aortic valve with coaptation and compliant aortic root.* Medical & Biological Engineering & Computing, 2012. **50**(2): p. 173-182.

61. De Hart, J., et al., *A three-dimensional computational analysis of fluid-structure interaction in the aortic valve.* J Biomech, 2003. **36**(1): p. 103-112.

62. Borazjani, I., *Fluid-structure interaction, immersed boundary-finite element method simulations of bio-prosthetic heart valves.* Computer Methods in Applied Mechanics and Engineering, 2013. **257**: p. 103-116.

63. Billiar, K.L. and M.S. Sacks, *Biaxial mechanical properties of the natural and glutaraldehyde treated aortic valve cusp—part I: experimental results.* Journal of Biomechanical Engineering, 2000. **122**(1): p. 23-30.

64. Strecker, C., et al., *Flow-sensitive 4D MRI of the thoracic aorta: Comparison of image quality, quantitative flow, and wall parameters at 1.5 T and 3 T.* Journal of Magnetic Resonance Imaging, 2012. **36**(5): p. 1097-1103.

65. Markl, M., et al., *4D flow MRI.* Journal of Magnetic Resonance Imaging, 2012. **36**(5): p. 1015-1036.

66. Leo, H.L., et al., *Fluid dynamic assessment of three polymeric heart valves using particle image velocimetry.* Ann Biomed Eng, 2006. **34**(6): p. 936-952.

67. Querzoli, G., S. Fortini, and A. Cenedese, *Effect of the prosthetic mitral valve on vortex dynamics and turbulence of the left ventricular flow.* Physics of Fluids, 2010. **22**(4).

68. Falahatpisheh, A. and A. Kheradvar, *High-speed particle image velocimetry to assess cardiac fluid dynamics in vitro: From performance to validation.* European Journal of Mechanics B-Fluids, 2012. **35**: p. 2-8.

69. Toger, J., et al., *Vortex Ring Formation in the Left Ventricle of the Heart: Analysis by 4D Flow MRI and Lagrangian Coherent Structures.* Ann Biomed Eng, 2012. **40**(12): p. 2652-2662.

70. Bellofiore, A., E.M. Donohue, and N.J. Quinlan, *Scale-up of an unsteady flow field for enhanced spatial and temporal resolution of PIV measurements: application to leaflet wake flow in a mechanical heart valve.* Experiments in Fluids, 2011. **51**(1): p. 161-176.

71. Kaminsky, R., et al., *Flow visualization through two types of aortic prosthetic heart valves using stereoscopic high-speed particle image velocimetry.* Artificial Organs, 2007. **31**(12): p. 869-879.

72. Seaman, C., A.G. Akingba, and P. Sucosky, *Steady Flow Hemodynamic and Energy Loss Measurements in Normal and Simulated Calcified Tricuspid and Bicuspid Aortic Valves.* J Biomech Eng, 2014.

73. Keshavarz-Motamed, Z., et al., *Effect of coarctation of the aorta and bicuspid aortic valve on flow dynamics and turbulence in the aorta using particle image velocimetry.* Experiments in Fluids, 2014. **55**(3).

74. Grande, K.J., et al., *Stress variations in the human aortic root and valve: the role of anatomic asymmetry.* Ann Biomed Eng, 1998. **26**(4): p. 534-545.

75. Mao, S.S., et al., *Normal thoracic aorta diameter on cardiac computed tomography in healthy asymptomatic adults: impact of age and gender.* Academic radiology, 2008. **15**(7): p. 827-834.

76. Tops, L.F., et al., *Noninvasive evaluation of the aortic root with multislice computed tomography implications for transcatheter aortic valve replacement.* JACC Cardiovasc Imaging, 2008. **1**(3): p. 321-30.

77. de Paulis, R., et al., *Coronary flow characteristics after a Bentall procedure with or without sinuses of Valsalva1.* European journal of cardio-thoracic surgery, 2004. **26**(1): p. 66-72.

78. Nobari, S., et al., *Therapeutic Vascular Compliance Change May Cause Significant Variation in Coronary Perfusion: A Numerical Study.* Computational and Mathematical Methods in Medicine, 2012.

79. Nishimura, R., et al., *2014 AHA/ACC Guideline for the Management of Patients With Valvular Heart Disease: Executive Summary.* Journal of the American College of Cardiology, 2014. **63**(22): p. 2438-2488.

80. Walther, T., et al., *Minimally invasive transapical beating heart aortic valve implantation â" proof of concept.* European journal of cardio-thoracic surgery, 2007. **31**(1): p. 9-15.

81. Kheradvar, A., et al., *Emerging Trends in Heart Valve Engineering: Part II. Novel and Standard Technologies for Aortic Valve Replacement.* Ann Biomed Eng, 2014: p. 1-14.

82. Clavel, M.-A., et al., *Validation and Characterization of Transcatheter Aortic Valve Effective Orifice Area Measured by Doppler Echocardiography.* JACC: Cardiovascular Imaging, 2011. **4**(10): p. 1053-1062.

83. Clavel, M.-A., et al., *Comparison of the hemodynamic performance of percutaneous and surgical bioprostheses for the treatment of severe aortic stenosis.* Journal of the American College of Cardiology, 2009. **53**(20): p. 1883-1891.

84. Groves, E.M., et al., *The Effects of Positioning of Transcatheter Aortic Valves on Fluid Dynamics of the Aortic Root.* ASAIO, 2014. **60**(5): p. 545-552.

85. Vesely, I. *For Patients*. 2015; Available from: http://www.valvexchange.com/for-patients/.

86. Fanning, J.P., et al., *The silent and apparent neurological injury in transcatheter aortic valve implantation study (SANITY): concept, design and rationale.* Bmc Cardiovascular Disorders, 2014. **14**.

87. Chiam, P.T.L., *Percutaneous transcatheter aortic valve implantation: Evolution of the technology.* The American heart journal, 2009. **157**(2): p. 229.

88. Ranucci, M., et al., *Aortic Cross-Clamp Time, New Prostheses, and Outcome in Aortic Valve Replacement.* Journal of Heart Valve Disease, 2012. **21**(6): p. 732-739.

89. Salis, S., et al., *Cardiopulmonary bypass duration is an independent predictor of morbidity and mortality after cardiac surgery.* Journal of cardiothoracic and vascular anesthesia, 2008. **22**(6): p. 814-822.

90. Lamelas, J., et al., *Outcomes of Minimally Invasive Valve Surgery Versus Median Sternotomy in Patients Age 75 Years or Greater.* The annals of thoracic surgery, 2011. **91**(1): p. 79-84.

91. Cooley, D., *Antagonist's View of Minimally Invasive Heart Valve Surgery.* Journal of cardiac surgery, 2000. **15**(1): p. 3-5.

92. Cooley, D., The annals of thoracic surgery, 1998. **66**(3): p. 1101-1105.

93. Santarpino, G., et al., *Sutureless replacement versus transcatheter valve implantation in aortic valve stenosis: A propensity-matched analysis of 2 strategies in high-risk patients.* Journal of Thoracic and Cardiovascular Surgery, 2014. **147**(2): p. 561-567.

94. Miceli, A., et al., *Minimally invasive aortic valve replacement with Perceval S sutureless valve: Early outcomes and one-year survival from two European centers.* Journal of Thoracic and Cardiovascular Surgery, 2014. **148**(6): p. 2838-2843.

95. Flameng, W., et al., *Effect of sutureless implantation of the Perceval S aortic valve bioprosthesis on intraoperative and early postoperative outcomes.* Journal of Thoracic and Cardiovascular Surgery, 2011. **142**(6): p. 1453-1457.

96. Cox, J.L., et al., *Tubular heart valves: A new tissue prosthesis design - Preclinical evaluation of the 3F aortic bioprosthesis.* Journal of Thoracic and Cardiovascular Surgery, 2005. **130**(2): p. 520-527.

97. Stühle, S., et al., *Fluid Dynamic Investigation of the ATS 3F Enable Sutureless Heart Valve.* Innovations: Technology and Techniques in Cardiothoracic and Vascular Surgery, 2011. **6**(1): p. 37-44.

98. Martens, S., *Sutureless aortic valve replacement with the 3f Enable aortic bioprosthesis.* The annals of thoracic surgery, 2009. **87**(6): p. 1914.

99. Carrel, T., L. Englberger, and M. Stalder, *Recent developments for surgical aortic valve replacement: The concept of sutureless valve technology.* Open Journal of Cardiology, 2013. **4**(1).

100. Shrestha, M., et al., *Sutureless Perceval S aortic valve replacement: a multicenter, prospective pilot trial.* J Heart Valve Dis, 2009. **18**(6): p. 698-702.

101. Moore, B.L. and L.P. Dasi. *Aortic Valve Sinus Vorticity Dynamics and the Potential Role of Coronary Flow*. in *ASME 2013 Summer Bioengineering Conference*. 2013. American Society of Mechanical Engineers.

102. Yap, C.H., et al., *Experimental measurement of dynamic fluid shear stress on the aortic surface of the aortic valve leaflet.* Biomechanics and Modeling in Mechanobiology, 2012. **11**(1-2): p. 171-182.

103. Chrisohoides, A. and F. Sotiropoulos, *Experimental visualization of Lagrangian coherent structures in aperiodic flows.* Physics of Fluids, 2003. **15**(3): p. L25-L28.

104. Kvitting, J.P.E., et al., *Flow patterns in the aortic root and the aorta studied with time-resolved, 3-dimensional, phase-contrast magnetic resonance imaging: Implications for aortic valve-sparing surgery.* Journal of Thoracic and Cardiovascular Surgery, 2004. **127**(6): p. 1602-1607.

105. Kilner, P.J., et al., *HELICAL AND RETROGRADE SECONDARY FLOW PATTERNS IN THE AORTIC-ARCH STUDIED BY 3-DIRECTIONAL MAGNETIC-RESONANCE VELOCITY MAPPING.* Circulation, 1993. **88**(5): p. 2235-2247.

106. Moore, B., et al. *Effect of Coronary Flow and Implications of Trans-Catheter Aortic Valve Implantation on Sinus Flow*. in *World Congress of Biomechanics*. 2014. Boston, Massachusetts.

107. Moore, B. and L.P. Dasi, *CORONARY FLOW IMPACTS AORTIC LEAFLET MECHANICS AND AORTIC SINUS HEMODYNAMICS.* Annals of Biomedical Engineering, 2015.

108. Knight, J., et al., *Ex vivo and in vivo coronary ostial locations in humans.* Surgical and Radiologic Anatomy, 2009. **31**(8): p. 597-604.

109. Spiller, P., et al., *Measurement of systolic and diastolic flow rates in the coronary artery system by x-ray densitometry.* Circulation, 1983. **68**(2): p. 337-347.

110. Johnson, K., P. Sharma, and J. Oshinski, *Coronary artery flow measurement using navigator echo gated phase contrast magnetic resonance velocity mapping at 3.0 T.* J Biomech, 2008. **41**(3): p. 595-602.

111. Payne, J., et al., *Assessment of coronary arterial flow and flow reserve in humans with magnetic resonance imaging.* Circulation, 1996. **93**(8): p. 1502-8.

112. Gharib, M., E. Rambod, and K. Shariff, *A universal time scale for vortex ring formation.* Journal of Fluid Mechanics, 1998. **360**: p. 121-140.

113. Davies, P.F., A.G. Passerini, and C.A. Simmons, *Aortic valve - Turning over a new leaf(let) in endothelial phenotypic heterogeneity.* Arteriosclerosis Thrombosis and Vascular Biology, 2004. **24**(8): p. 1331-1333.

114. Balachandran, K., P. Sucosky, and A.P. Yoganathan, *Hemodynamics and Mechanobiology of Aortic Valve Inflammation and Calcification.* International Journal of Inflammation, 2011: p. 263870.

115. Spiller, P., et al., *MEASUREMENT OF SYSTOLIC AND DIASTOLIC FLOW-RATES IN THE CORONARY-ARTERY SYSTEM BY X-RAY DENSITOMETRY.* Circulation, 1983. **68**(2): p. 337-347.

116. Bellhouse, B.J. and L. Talbot, *FLUID MECHANICS OF AORTIC VALVE.* Journal of Fluid Mechanics, 1969. **35**: p. 721-&.

117. Peskin, C.S. and A.W. Wolfe, *AORTIC SINUS VORTEX.* Federation Proceedings, 1978. **37**(14): p. 2784-2792.

118. Turitto, V.T. and C.L. Hall, *Mechanical factors affecting hemostasis and thrombosis.* Thrombosis Research, 1998. **92**(6): p. S25-S31.

119. Wootton, D. and D. Ku, *Fluid Mechanics of Vascular Systems, Diseases, and Thrombosis.* Annual review of biomedical engineering, 1999. **1**(1): p. 299-329.

120. Chandra, S., N.M. Rajamannan, and P. Sucosky, *Computational assessment of bicuspid aortic valve wall-shear stress: implications for calcific aortic valve disease.* Biomechanics and Modeling in Mechanobiology, 2012. **11**(7): p. 1085-1096.

121. Golzari, M. and J.B. Riebman, *The four seasons of ruptured sinus of Valsalva aneurysms: Case presentations and review.* Heart Surgery Forum, 2004. **7**(6): p. E577-E583.

122. Jin, S., J. Oshinski, and D. Giddens. *Numerical Simulation of Flow Patterns in the Entrance Regions of the Left and Right Coronary Arteries*. in *2nd Joint Conference of the IEEE Engineering in Medicine and Biology Society and the Biomedical Engineering Society*. 2002. Houston, TX.

123. Yilmaz, S., et al., *Optimal in vitro realization of pulsatile coronary artery flow waveforms using closed-loop feedback algorithms with multiple flow control devices.* Turkish Journal of Electrical Engineering & Computer Sciences, 2012. **20**(6): p. 1006-1030.

124. Moore, B., P. Maureira, and L.P. Dasi. *Effects of Coronary Flow on Sinus Hemodynamics in the Presence of a Transcatheter Aortic Valve Implantation*. in *Summer Biomechanics, Bioengineering, and Biotransport Conference*. 2015. Snowbird, Utah.

125. Lichtenstein, S.V., et al., *Transapical transcatheter aortic valve implantation in humans - Initial clinical experience.* Circulation, 2006. **114**(6): p. 591-596.

126. Bapat, V.N., et al., *Fluoroscopic Guide to an Ideal Implant Position for Sapien XT and CoreValve During a Valve-in-Valve Procedure.* Jacc-Cardiovascular Interventions, 2013. **6**(11): p. 1186-1194.

127. Balachandran, K., P. Sucosky, and A.P. Yoganathan, *Hemodynamics and mechanobiology of aortic valve inflammation and calcification.* International journal of inflammation, 2011. **2011**.

128. Pillai, R., et al., *3f prosthesis aortic cusp replacement: implantation technique and early results.* Asian Cardiovascular and Thoracic Annals, 2010. **18**(1): p. 13-16.

9. APPENDIX I

This appendix gives detailed dimensions of each of the three custom-fabricated valve chambers. Each chamber was designed in SOLIDWORKS, and this software was used to create these dimension drawings.

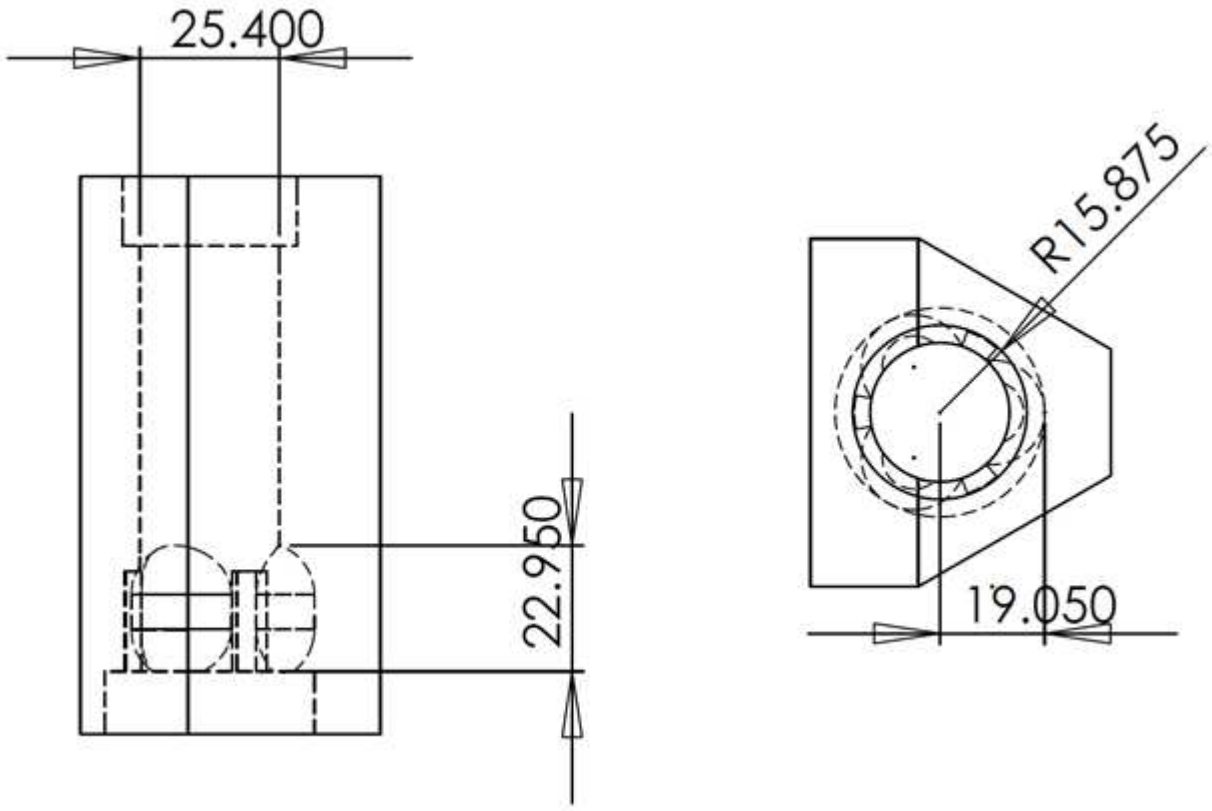

Valve chamber dimensions are shown for the initial mock aortic root, which was used as the larger sinus model.

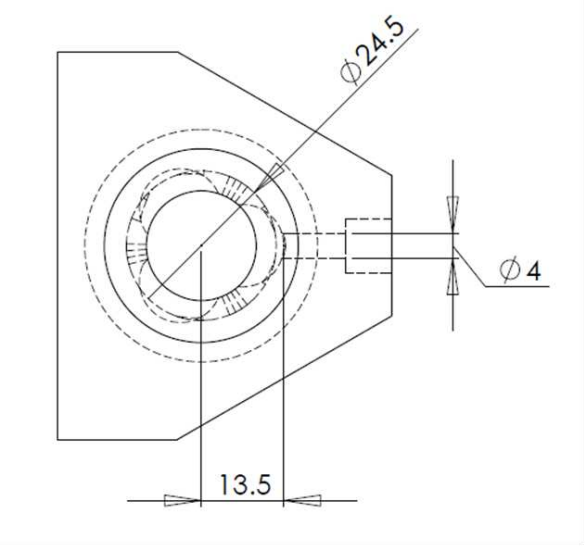

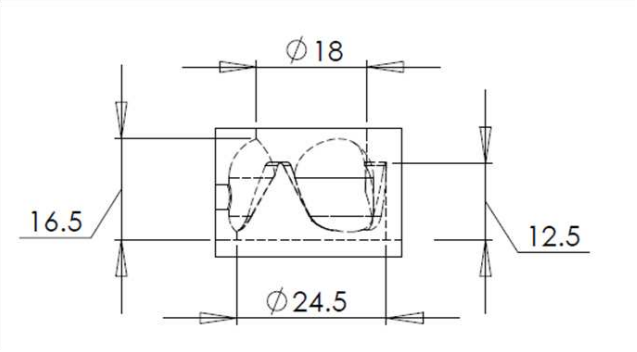

Dimensions are given for the valve chamber that was developed for flush-mounting of the porcine bioprosthesis used as the model native valve. This chamber was used as the smaller sinus model.

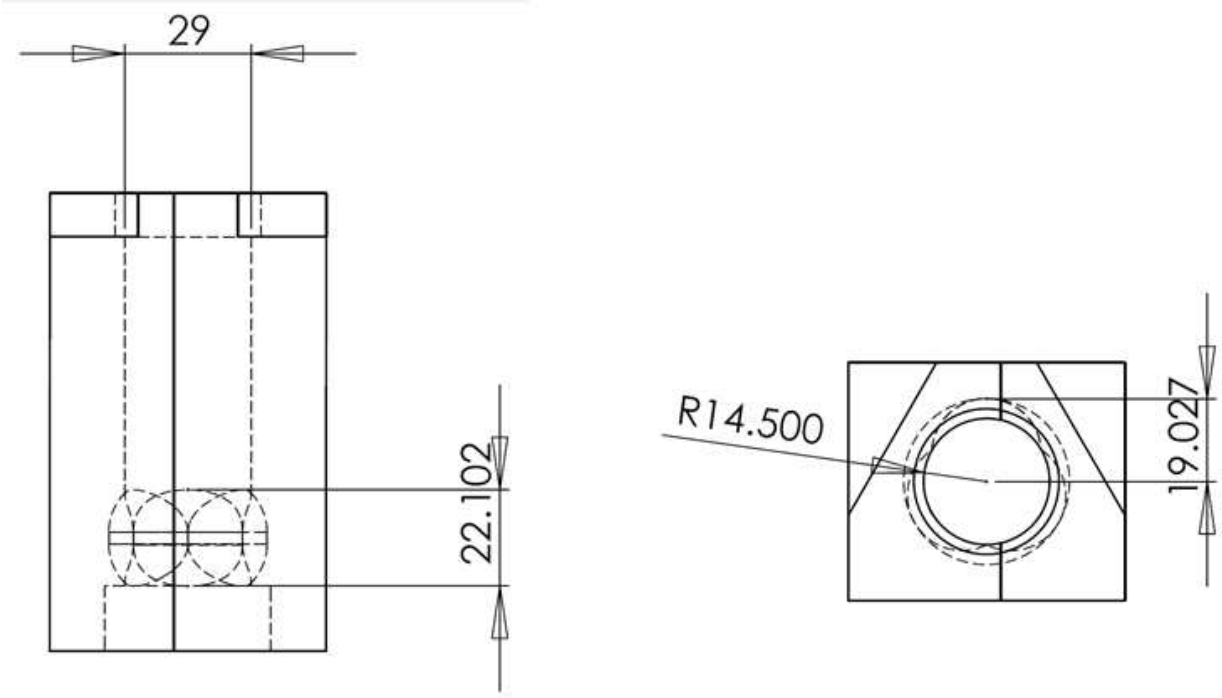

The final sinus chamber fabricated was designed specifically for the ATS 3F Enable sutureless valve, and detailed dimensions are given.

10. APPENDIX II

This appendix gives information on how the 3D computational aortic valve geometry was created in SOLIDWORKS.

Step 1: A cylinder is created to represent the aorta and an ellipsoid is added to this cylinder to represent one sinus.

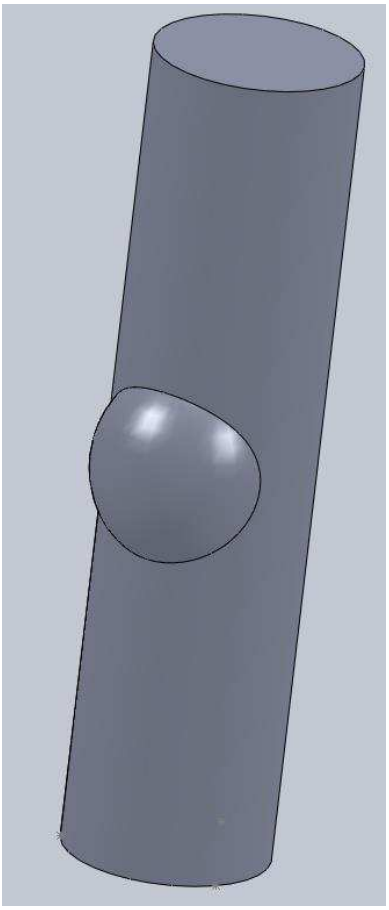

Step 2: A slightly larger ellipsoid is added at the same location as the existing ellipsoid (aka sinus) and 2 intersection curves are created – 1) intersection of the aorta and sinus, 2) intersection of the aorta and larger ellipsoid. This is done to create leaflets, so the difference in diameter between the 2 sinus ellipsoids should be chosen to match leaflet thickness.

Step 3: Intersection curves are manipulated (trimmed and then connected) to create two closed profiles on either side of the sinus, below the sinus midplane.

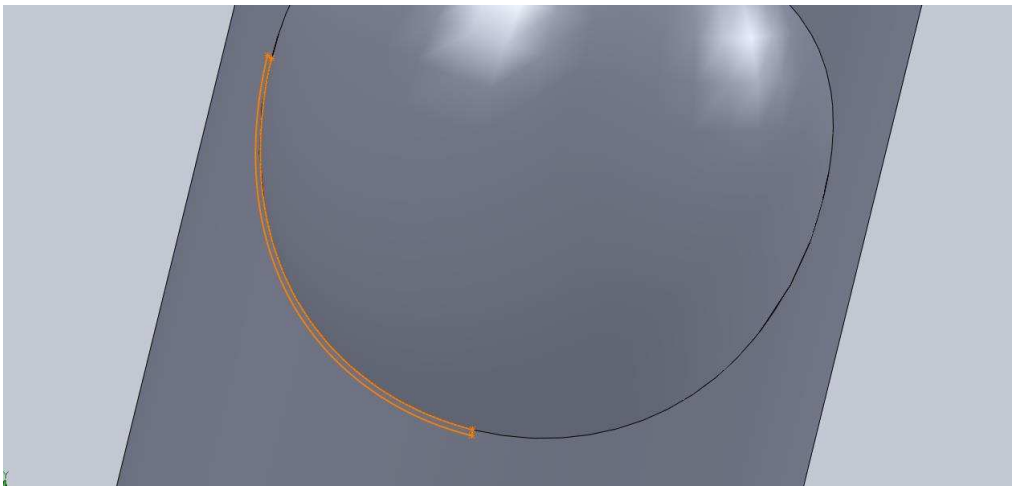

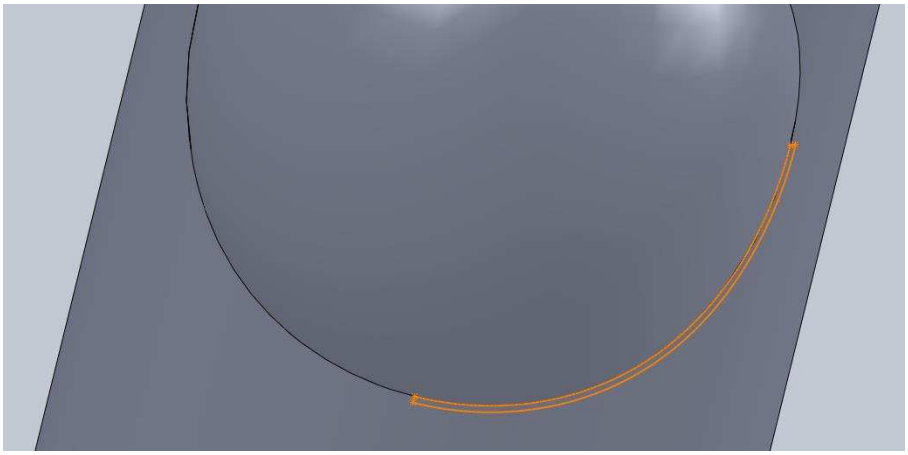

Step 4: Splines are created to represent the leaflet profile at multiple heights. A spline connecting the commissures determines the profile of the leaflet free edge, and a spline closer

to the base of the leaflets ensures that the profile at this location is realistic (if unconstrained at this level, modeling difficulties may arise when creating the leaflet in the next step).

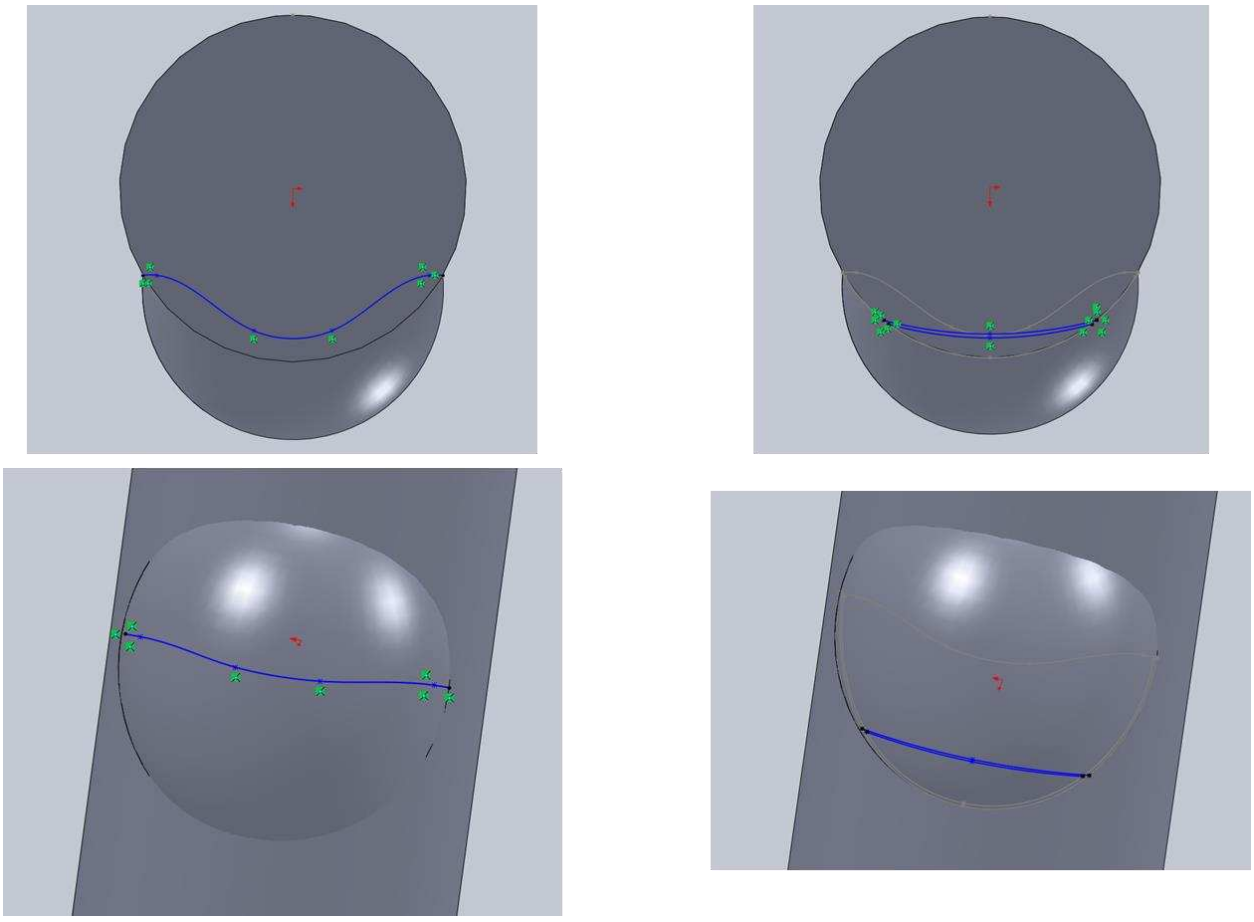

Step 5: A lofted cut is generated to create the leaflets. The two closed profiles created in Step 3 are constrained along the splines created in Step 4.

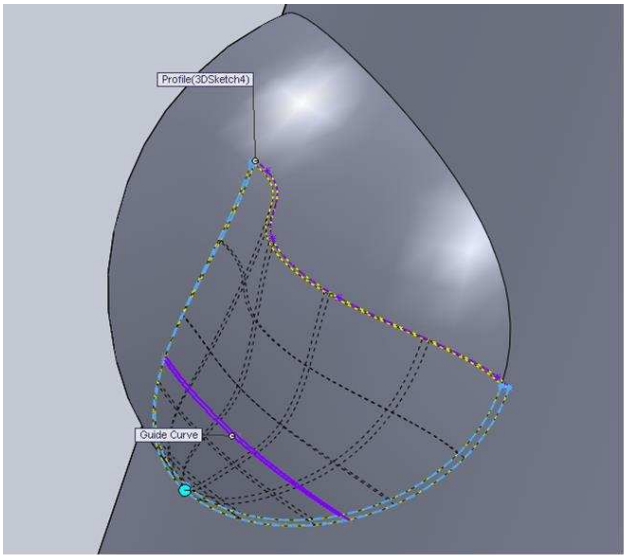

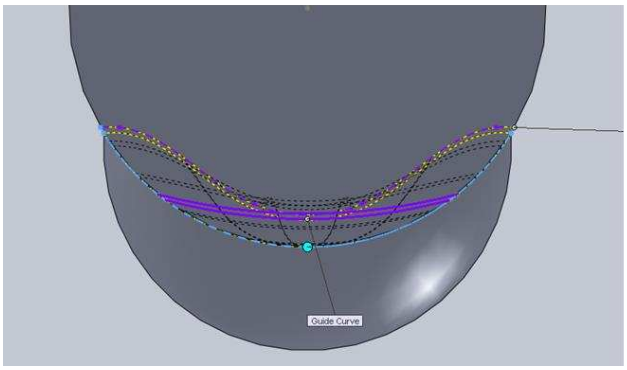

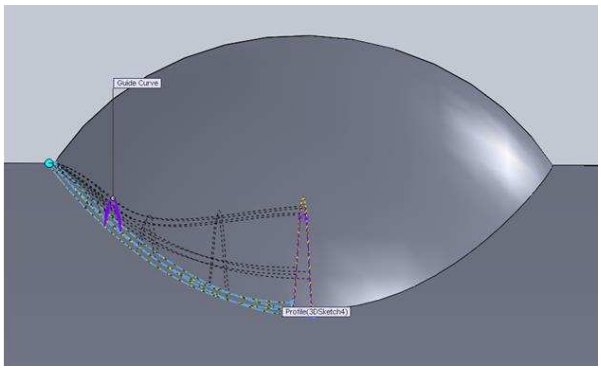

Step 6: This part is cut into a “wedge”, representing one third of the valve radially. Three wedges are then assembled into the complete geometry.